Exploratory Study of ECL Backgrounds Arising from Charged Hadrons at Belle II

Garrett Leverick

Department of Physics

McGill University, Montreal

October 2023

A thesis submitted to McGill University in partial fulfillment of the requirements of the degree of Master of Science

Abstract

The Belle II experiment is making ultra precise measurements of B meson decay chains to search for deviations from the Standard Model, the leading theory of particle physics. Many physics analyses at Belle II analyze residual electromagnetic calorimeter (ECL) energy to significantly improve their signal decay purity. Spurious ECL clusters decrease the separation power of residual ECL energy, thereby reducing precision of physics measurements. Therefore, it is important to remove the spurious ECL clusters from the residual ECL energy measurement while keeping any residual energy from true sources. To improve the discrimination between true and spurious ECL clusters, characterization studies of the sources for spurious clusters were performed.

It was found that the majority of spurious clusters (not arising from beam background or bremsstrahlung radiation) were due to processes called hadronic split off and low transverse momentum clustering. These processes were characterized by the momentum and type of the particles that cause them. Relations between the spurious cluster and the track associated to the charged particle causing the spurious cluster were found to be promising discriminators that have not yet been used in the discrimination of spurious ECL clusters.

Abrégé

L'expérience Belle II effectue des mesures super-précises des chaînes de désintégration du méson B afin de rechercher des déviations par rapport au Modèle Standard, la principale théorie de la physique des particules. De nombreuses analyses physiques effectuées à Belle II analysent l'énergie résiduelle du calorimètre électromagnétique (ECL) afin d'améliorer de manière significative la pureté du signal de désintégration. Les grappes erronées de cellules de l'ECL diminuent la capacité de séparation de l'énergie résiduelle du calorimètre électromagnétique, réduisant ainsi la précision des mesures de physique. Il est donc important d'éliminer ces grappes erronées de cellules, tout en conservant l'énergie résiduelle provenant de vraies sources du signal. Pour améliorer la discrimination entre les grappes vraies et erronées, des études de caractérisation de sources possibles ont été réalisées.

Il s'est avéré que la majorité des grappes erronées (qui ne proviennent pas des photons de bruit du faisceau ou du rayonnement de freinage) étaient dues à des processus appelés séparation hadronique et grappes à basse quantité de mouvement transversale. Ces processus sont caractérisés par la quantité de mouvement et le type de particules qui les provoquent. Les relations entre une grappe erronée et la trace associée à la particule chargée à l'origine cette grappe se sont révélées être des discriminateurs prometteurs qui n'ont pas encore été utilisés dans la discrimination des grappes erronées de l'ECL.

Acknowledgements

The work presented in this thesis is built on the back of the Belle II collaboration, so I owe many thanks to the (over one thousand) members who have put so much work in to make this research possible.

The next person without whom I could not have completed this thesis is my supervisor, Dr. Steven Robertson. Thank you for guiding me in my research and studies, providing feedback to my talks and writing, and presenting me with multiple amazing opportunities to engage with our physics community. Along with the rest of the McGill Belle II group, which includes Dr. Andreas Warburton, Andrea Fodor, Dr. Hannah Wakeling, Trevor Shillington, Kai-Ning Chu, and Dr. Raynette van Tonder, I greatly appreciate your time, effort, and patience you all have given me. You have all been wonderful to work with.

I would like to thank Dr. Francois Corriveau for revising my French translation of the abstract.

I would also like to think the greater McGill physics graduate student community, the friends I have made along the way, the friends who stuck with me, and of course my family who has been so supportive despite being 2000 km away.

Preface

Unless otherwise stated, the work in this thesis was performed by the author as a Masters student at McGill University. All sections were written by the author and represent original content with any references to work of others accompanied by a citation. All plots and tables were produced by the author unless otherwise stated and cited.

Table of Contents

List of Figures

List of Tables

Chapter 1

Introduction

The foundational question of particle physics is: What are the fundamental building blocks of the universe and how do they interact with each other? A compilation of theories called the Standard Model (SM) is the most complete answer to this question. The SM can be confoundingly accurate in its agreement with experiment. However, the physics community knows it is incomplete due to observations related to neutrino masses [1, 2, 3], measurements of some B meson decays [4], the absence of gravity in the model, and various other problems. To resolve these issues, particle physicists must perform measurements that either confirm the SM or are explained by new theories that are beyond the Standard Model (BSM). Were a BSM theory confirmed, it would be considered new physics (NP).

There are two main approaches to find NP. One is on the energy frontier, where particle interactions at higher and higher energies (like those at the Large Hadron Collider) may allow direct creation and measurement of highly massive particles and their interactions. The other is the luminosity frontier, where NP, or signs of NP, may be found in small deviations from the SM in high precision measurements. The Belle II [5] experiment is on the cutting edge of the high-luminosity approach.

The Belle II experiment is located at the SuperKEKB collider [6] in Tsukuba, Japan. SuperKEKB collides electrons and positrons at energies to encourage the production of

B mesons. When a B meson is produced, it will decay within the beam pipe since its lifetime is on the order of 1×10^{-12}s [7]. This means it will not reach sensitive detector material, but instead decay to intermediate state and/or final state particles. Intermediate state particles are other heavy mesons, like D mesons, that have very short lifetimes and further decay to final state particles that can be seen in the Belle II detector. Based on the detector information, the decay chains of the B mesons can be reconstructed. Belle II aims to uncover NP through the precise study of B meson decay chains.

Unfortunately, the Belle II detector may sometimes make incorrect measurements of final state particles. As a result, spurious background particles are sometimes reconstructed. There are a number of reasons why this is bad, so it is important to discriminate between these spurious particles and real ones. Of particular importance for π^0 reconstruction and the use of residual calorimeter energy in analyses, both of which will be described later, is the discrimination of spurious photon candidates. These spurious photon candidates, seen in the electromagnetic calorimeter of Belle II, are caused by beam backgrounds, bremsstrahlung radiation from particles traversing the tracking detector, artifacts from the calorimeter reconstruction and/or the interactions of particles within the calorimeter, and perhaps other sources. The aim of this thesis is to characterize the spurious photon candidates related to charged particles traversing the calorimeter, thereby finding new information that can be used to discriminate them from real photons.

Chapter 2 will contain background information on the Standard Model and particle interactions with matter so that the purpose and operation of the Belle II experiment may be understood. Chapter 3 will give details on the Belle II experiment and detector while Chapter 4 describes how relevant parts of the detector information are used and analyzed. Chapter 5 begins the analysis section, introducing properties of spurious photon candidates and Chapter 6 contains information on their discrimination. Chapter 7 discusses the analysis and ways to improve discrimination of spurious photons. Finally, Chapter 8 serves as a conclusion to the thesis.

Chapter 2

Background

2.1 The Standard Model

The standard model (SM) is the leading theory of particle physics due to its power in predicting particles such as the top quark [8, 9] and the Higgs boson [10, 11] and agreements in precision measurements of fundamental quantities such as the W boson mass [12, 13]. It details seventeen elementary particles and three of the four ways they can interact with each other. An elementary particle is defined as a particle that has no underlying structure, and can therefore be mathematically modelled as excitations in quantum fields [14]. These fields may interact with themselves and one another in ways described by electroweak theory [15, 16, 17, 18] and quantum chromodynamics (QCD) [19]. These theories are built on symmetries described by mathematical structures called special unitary groups ($SU(n)$), first introduced to model physical processes by Yang and Mills [20].

The particles of the SM, depicted in figure 2.1, may be organized into fermions and bosons based on a property called spin. Fermions have half integer spin, while bosons have integer spin. Bosons that are spin-1 mediate the various interactions between particles in the SM. These interactions, also called forces, are electromagnetism, the weak force, and the strong force. Gravity, the fourth fundamental force, is not modelled within the SM in part due to how weak it is at the scale of particle physics. The force carrying

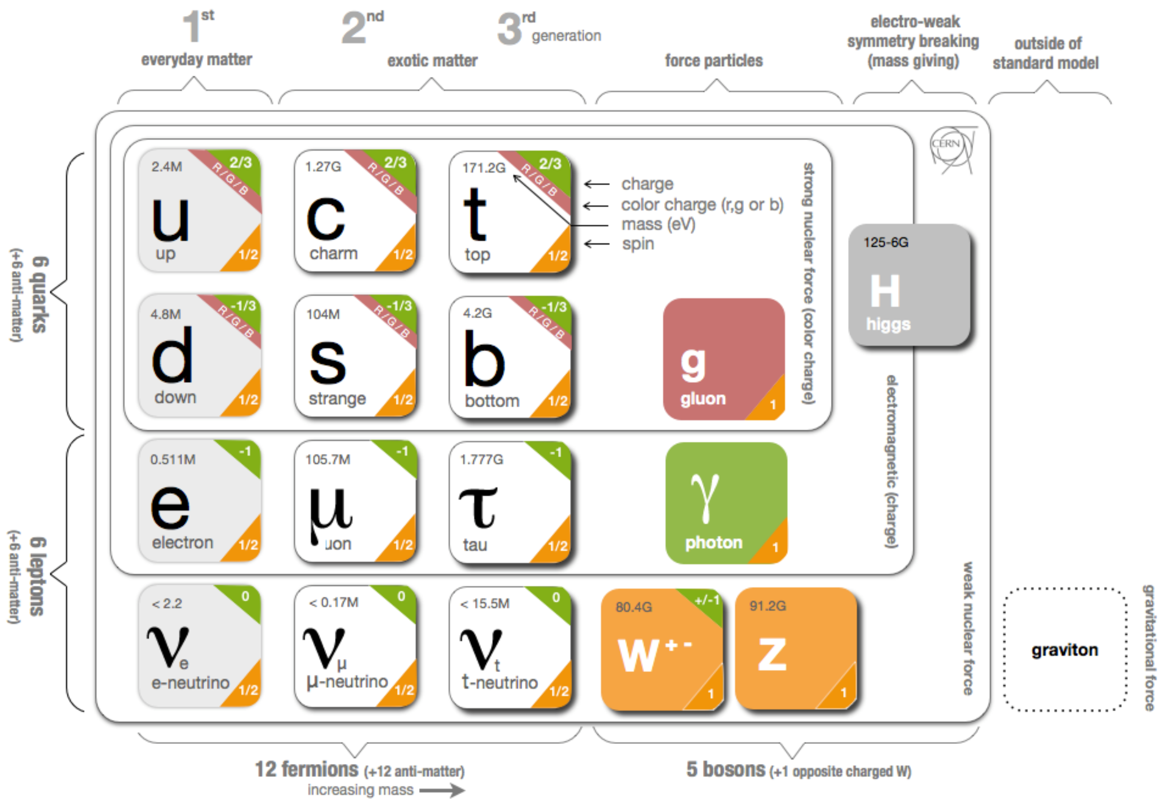

Figure 2.1: The standard model of elementary particles represented pictorially, with properties of each particle listed. The graviton is hypothetical. From [23].

bosons arise from gauge fields acting on fermions which are allowed because the Lagrangian is invariant under local symmetries according to operations associated to Lie groups. The only boson within the SM that is not spin-1 is the Higgs boson which is spin-0 and is responsible for giving the elementary particles their mass by spontaneous symmetry breaking [21, 22].

What distinguishes elementary particles from one another are their properties (such as mass, charge, and spin) that determine how they interact with each other. The fermions make up what is called matter, and each of them have an antimatter counterpart. Antimatter particles have the same mass and spin as their corresponding matter particles, but have opposite quantum numbers (such as electric charge, lepton number, weak isospin, etc). Therefore, when a particle and its corresponding antiparticle interact, they can annihilate and produce another particle-antiparticle pair.

2.1.1 The Fundamental Forces

Each SM force arises from some imposed gauge invariance on the SM Lagrangian. The SM is a non-abelian gauge theory with the symmetry group $SU(3) \times SU(2) \times U(1)$. This group can be broken down to strong and electroweak parts. The $SU(3)$ group makes up the eight massless fields known as gluons which mediate the strong force. The eight fields correspond to the various different gluons that can be exchanged between particles while conserving color charge, the strong force analogue to electric charge. The $SU(2) \times U(1)$ group forms the four fields required for the electroweak force. However, at low enough energies (which aren't actually that low in todays standards), electroweak symmetry breaking occurs due to the Higgs field [22]. This leaves the broken $SU(2)$ group for the weak force and residual $U(1)$ group for the electromagnetic force. The broken $SU(2)$ group results in massive fields corresponding to the W and Z bosons of the weak interaction and the massless photon field comes from $U(1)$ group.

The weak and strong forces get their names from a property known as their coupling. A coupling is key in determining how likely a force carrier is to be exchanged between two particles. The strong force has the largest coupling of the three forces, while the weak force has the lowest. However, when considering a likelihood of an interaction, the range must also be considered. Electromagnetism has an infinite range because photons are massless. While gluons are massless, they may self interact which limits their range to short distances, yet also makes the strong interaction weaker at extremely short distances, a process called asymptotic freedom [24, 25]. On the other hand, the weak force carriers are massive, which limits their range due to their limited lifetimes. Furthermore, the weak force is parity violating, meaning it does not occur for particles that are right-handed[1] or anti-particles that are left-handed [26]. Lastly, the charge of the particles that could participate in an interaction is also important in determining the likelihood of an interaction. While electric charge is often a familiar term, color charge (strong force) and weak charge (weak force) may be assigned to particles as well.

2.1.2 Elementary and Composite Particles

The fermions, or matter particles, are further divided into two sets, quarks, which may interact via the strong force, and leptons, which cannot interact via the strong force. All 12 of these particles can interact via the weak force, and all may interact electromagnetically except neutrinos since they do not have electric charge. There are three generations of both leptons and quarks, with each generation essentially being distinguished by its mass. Each generation of quarks and leptons consists of an $SU(2)$ doublet due to the broken symmetry of the weak force.

The lepton generations are the electron, the muon, and the tau, where each charged lepton has a neutral partner called a neutrino. The muon and tau are $\sim$ 200 and $\sim$ 3500 times more massive than the electron [7], while neutrinos are massless in the SM. Electrons are common to everyday life, being the particles that orbit nuclei to form atoms which they're able to do because of their stability. On the other hand, the muon and tau have lifetimes of 2.2 microseconds and 290 femtoseconds [7] respectively and cannot form stable composite particles. However, due to relativistic effects seen in high-energy experiments, muons are still capable of travelling several meters to reach detectors in particle physics experiments. Such is not the case for the tau, only the daughters from its decay chain may be seen in detectors with the exception of emulsion film detectors [27] which have extremely high spatial resolution. Neutrinos have long lifetimes, but they often pass through detectors without being detected since they can only interact via the weak force.

[1] Handedness is the projection of a particle's spin on it's momentum, also known as helicity. When the spin is aligned with momentum, a particle is right-handed. When the spin is anti-aligned, it is left-handed.

The quark generations (in order) are up and down, charm and strange, and top and bottom. The first of each of those pairing has an electric charge of +2/3 while the second has charge -1/3. Quarks may bind to one another via the strong force to create composite particles called hadrons. In fact, due to a QCD principle called confinement, quarks can only exist in composite particles. The two most common combinations are pairs of quarks and antiquarks called mesons, and combinations of three quarks or three antiquarks called baryons. The hadrons most common in everyday life are baryons made from up and down quarks called protons and neutrons, which can further bind together via the strong force to form atomic nuclei due to their stability[2]. Common to particle physics experiments, and of particular significance for this thesis, are mesons called pions and kaons, which are formed from the various pairings of up, down, and strange quarks and antiquarks found in table 2.1. The charged versions of these particles have lifetimes long enough that they usually can reach a detector, but the neutral versions are more complicated. Neutral pions decay so quickly, almost always into two photons, that they are never directly detected. The decay of a neutral kaon is quite different to the other particles in table 2.1. The kaon's weak eigenstate is not equal to its mass eigenstate, which means a neutral kaon is in a superposition of the two weak eigenstates before it decays. Once it decays, the weak eigenstate is known. The lifetimes of the two weak eigenstates are quite different, and therefore only one of them can be directly detected. However, this is not to say physicists can never infer the existence of the short lived kaons or even neutral pions. Signatures of their decays can be searched for (by detecting their decay products) within detectors, which is sometimes more effective at finding the particles than direct detection of the long lived kaon.

The last composite particles worth noting are the Upsilon (Υ) and B mesons. The former is made from a bottom quark and bottom antiquark, while the latter are bottom quarks(antiquarks) paired with up or down antiquarks(quarks). An Upsilon can be produced by colliding electrons and positrons at an energy equal to the mass of the Upsilon.

[2]Free neutrons have a lifetime of $\sim$15 minutes, but bound in a nucleus can become stable at cosmological scales, i.e. an undetermined amount of time.

Particle	Mass	Quark Components	Charge	Lifetime
π^+	139.6 MeV/c^2	$u\overline{d}$	+1	26 ns
π^-	139.6 MeV/c^2	$\overline{u}d$	-1	26 ns
π^0	135.0 MeV/c^2	$\frac{1}{\sqrt{2}}\left(u\overline{u}+d\overline{d}\right)$	0	(84 ± 1.3) as
K^+	493.7 MeV/c^2	$u\overline{s}$	+1	12 ns
K^-	493.7 MeV/c^2	$\overline{u}s$	-1	12 ns
K^0	497.6 MeV/c^2	$d\overline{s}$	0	0.090 ns, 51 ns
$\overline{K^0}$	497.6 MeV/c^2	$\overline{d}s$	0	0.090 ns, 51 ns

Table 2.1: Pions and kaons listed with some of their properties. Note that two lifetimes are listed for neutral kaons since their weak eigenstates (which dictate lifetimes) aren't the same as their mass eigenstates [7].

At the 4S resonance (when the Upsilon has a specific internal angular momentum) it decays to *B* mesons >96% of the time [7]. This is the process Belle II uses to create *B* mesons.

2.2 Particle Interactions with Matter

In particle physics, the measurement of a particle actually refers to the measurement of a particle's interaction with some medium. Particles interact in various ways depending on their fundamental properties and their energy. Detectors are often designed to detect a certain subset of particles at a specified energy range. This section will describe the interactions particles face as they traverse matter.

2.2.1 Charged Particle Interactions

The main quantity used to characterize charged particle interactions in matter is called mass stopping power. It is a measure of the average energy loss as a particle passes through a material, normalized for density. In other words, it is the energy loss per unit mass per unit area. At energies relevant to the Belle II experiment, the main effects responsible for particle's energy loss in material are ionization and bremsstrahlung.

Ionization

Ionization is the stripping of electrons from atoms in a material. A charged particle has a chance of interaction with the electrons it passes by. Each interaction the incident particle loses energy by lifting the electron from the Coulomb potential of the atom, and transferring some kinetic energy. Energy loss from ionization may occur so long as the incident particle has enough energy to free electrons from the atom. The expression for mass stopping power by ionization is given by the Bethe equation [28],

$$\left\langle -\frac{dE}{dx} \right\rangle = Kz^2 \frac{Z}{A} \frac{1}{\beta^2} \left[\frac{1}{2} \ln \frac{2m_e c^2 \beta^2 \gamma^2 W_{max}}{I^2} - \beta^2 \right] \tag{2.1}$$

Where $\langle -\frac{dE}{dx} \rangle$ is the mass stopping power (often notated simply as $\frac{dE}{dx}$), z is the charge of the incident particle, Z is the atomic number of the material, A is the atomic mass of the material, β is the ratio of the particles velocity to the speed of light, γ is the Lorentz factor, m_e is the electron mass, I is the mean excitation energy, W_{max} is the maximum energy transfer to an electron in the material, and K is a coefficient. The last of these two quantities can be further expressed as the following,

$$W_{max} = \frac{2m_e c^2 \beta^2 \gamma^2}{1 + \frac{2\gamma m_e}{M} + \left(\frac{m_e}{M}\right)} \tag{2.2}$$

$$K = 4\pi N_A r_e^2 m_e c^2 \tag{2.3}$$

Where c is the speed of light, M is the mass of the incident particle (and it is assumed $M \gg m_e$ and the particle is point-like), N_A is Avogadro's number, and r_e is the classical electron radius.

What is immediately noticeable about this set of equations is the strong dependence on the factor $\beta\gamma$. Save for the mass of the incident particle and the properties of the absorber material, which don't cause large deviations with the exception of a couple special cases,

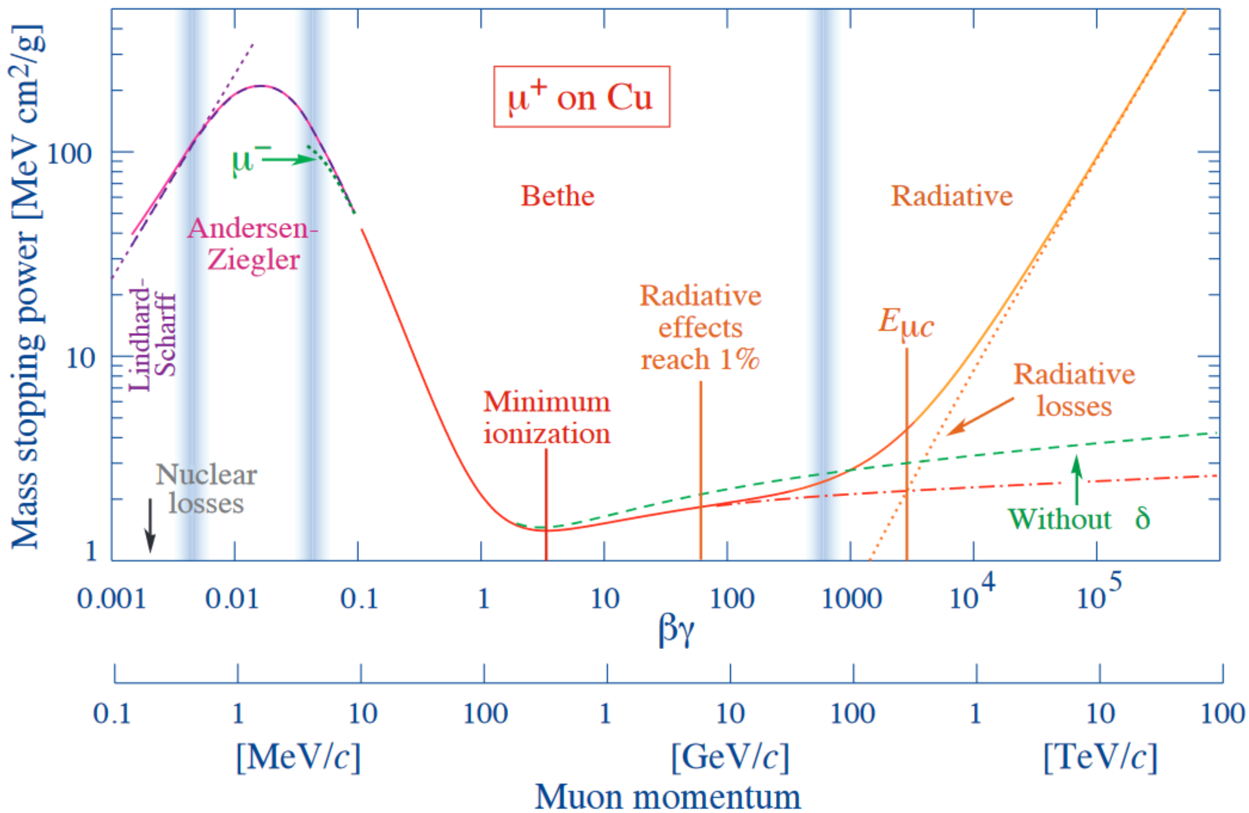

Figure 2.2: Mass stopping power for positive muons in copper. The dotted lines are components of the stopping power whereas the solid lines are total stopping power. Vertical bands are boundaries between the different models labeled on the plot. The critical energy (defined in the Bremsstrahlung section below) is labelled as $E_{\mu c}$. Various effects and corrections are labelled, but the ones which are of importance for this thesis are the Bethe and radiative curves in red and orange respectively [28].

all else is constant except $\beta\gamma$ which is equivalent to $\frac{p}{Mc}$ of the incident particle. This dependence is explicitly shown in the $0.1 < \beta\gamma < 1000$ region of figure 2.2. Particles that lie in the range $1 < \beta\gamma < 10$ are known as minimum ionizing particles (MIPs). Muons and pions are commonly MIPs in momentum ranges seen in the Belle II experiment.

Bremsstrahlung

Bremsstrahlung, a process in which photons are emitted during the deceleration of a particle in matter (usually around a nucleus), is important for highly relativistic particles. As can be seen in figure 2.2, it dominates the mass stopping power for $\beta\gamma \tilde{>} 1000$. While ionization still occurs for highly relativistic particles, the energy losses due to bremsstrahlung begin to dominate above an energy called the critical energy, labelled in figure 2.2 as $E_{\mu C}$[3]. In many particle physics experiments, including Belle II, only electrons characteristically reach a $\beta\gamma$ in which bremsstrahlung becomes important because of their small mass. Since this occurs so often for electrons, a parameter called "radiation length" has been developed to macroscopically describe the energy an electron loses due to bremsstrahlung radiation. It is employed in the following way,

$$E = E_0 e^{-x/X_0} \tag{2.4}$$

Where E and E_0 are the final and initial energies of the electron respectively, x is the thickness of material the electron has traversed, and X_0 is the radiation length for the material. This means an electron loses $1 - 1/e$, or about 63%, of its energy over one radiation length.

2.2.2 Photon Interactions

Photons lose energy quite differently than charged particles. This is due to their interaction being "catastrophic", meaning the photon is usually destroyed, or heavily altered, after an interaction. These interactions are the photoelectric effect, Compton scattering, and pair production. As can bee seen in figure 2.3, pair production is the dominant process for photons over 10 MeV in sodium iodide (NaI). Since photons in Belle II are often over this energy and absorbed in caesium iodide (CsI), it shall be assumed all photons undergo pair production going forward.

Pair production is the aptly named process in which a photon enters the electric field of a nucleus or electron and converts to an electron and positron pair. Macroscopically,

[3]Normally the critical energy is denoted as just E_C. The μ is specified since the data relate to muons.

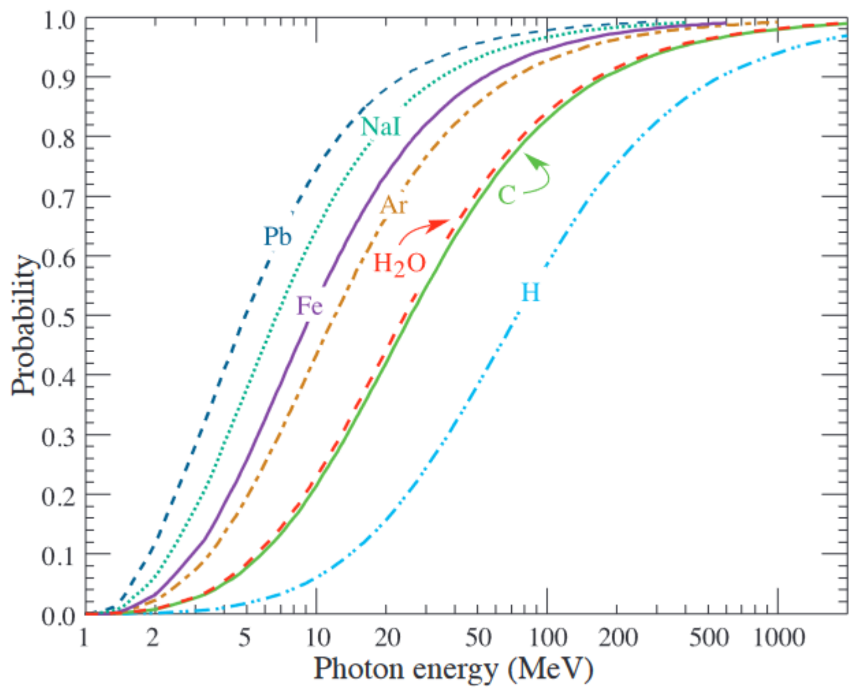

Figure 2.3: Probability that a photon interaction will result in pair production for various materials [28].

this process manifests itself in the property known as photon attenuation length, which is used in the following way,

$$P = e^{-x/\lambda} \tag{2.5}$$

Where P is the probability that a photon hasn't interacted in the material after traversing a distance x, and λ is the photon attenuation length. While this equation takes a form that is similar to that of radiation length, energy is not deposited unless the photon interacts and the energy dependence is hidden in the photon attenuation length. This energy dependence can be seen in figure 2.4.

2.2.3 Electromagnetic Showers

At energies relevant to the Belle II calorimeter (¿50 MeV for photons and ¿100 MeV for electrons), electron and positron interactions will create photons via bremsstrahlung,

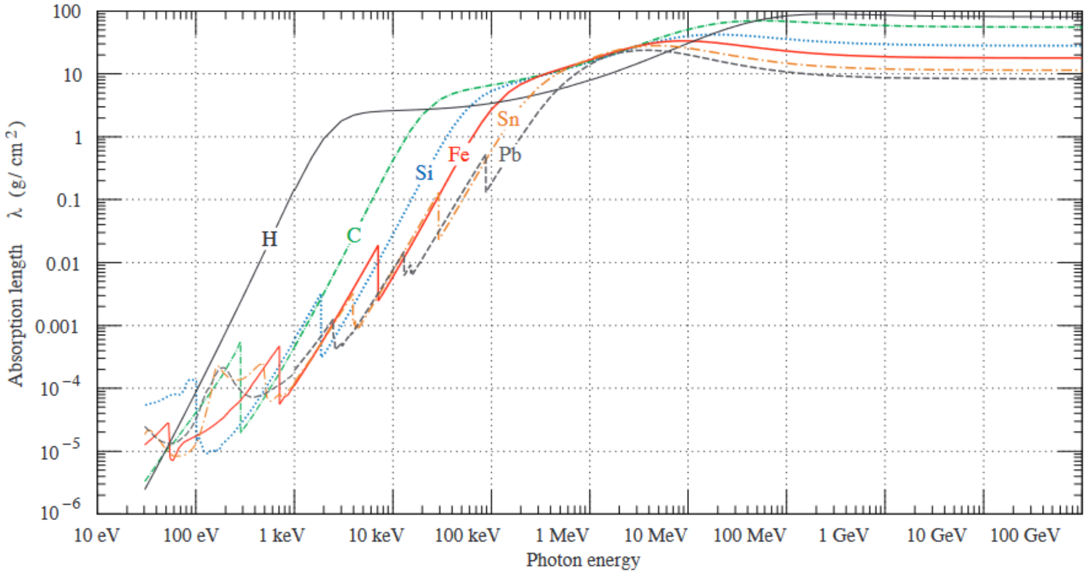

Figure 2.4: Photon mass attenuation length for various materials. Note that above 10 MeV the photon mass attenuation length is mostly constant. To get photon attenuation length, one must simply multiply by the density of the material [28].

which in turn can create an electron-positron pair via pair production. This back and forth occurs anytime a high energy photon or electron impinges on a material, and is called an electromagnetic shower or cascade. Since the photons create two particles, each of which can cause multiple photons, this back and forth is multiplicative. The electrons and photons continue their multiplication until their energies are reduced to the critical energy, at which point the photons will interact via Compton scattering and the photoelectric effect, and the electrons via ionization. If the material is a scintillant, the electrons (from earlier pair production and the low energy photon interactions) cause scintillation light proportional to the amount of energy deposited. Measuring electromagnetic showers to interpret the original particle's energy is the principle of electromagnetic calorimetry. The Belle II electromagnetic calorimeter will be discussed in section 3.2.

2.2.4 Hadronic Interactions

When traversing a material, hadrons may interact via the strong force with a nucleon. This interaction may be (quasi-)elastic, but more often than not, particularly at higher energies, it is inelastic as can be seen in figure 2.5. This means a variety of different particles may come from a hadronic interaction, so hadronic interactions are generally less predictable than electromagnetic ones. Furthermore, simple charge conjugation can change the cross section for a hadronic interaction by a factor of two. Hadronic interactions also change cross section with particle species, for example a kaon and pion of the same energy will have different cross sections (see figure A.1), and therefore different chances to interact. However, this can be generalized with a quantity that yields information on (roughly) how often a hadron will interact in material. This is called the nuclear interaction length, represented by λ_I, and is employed in the following way,

$$P = e^{-x/\lambda_I} \tag{2.6}$$

Where P is the probability a hadron has not interacted after passing through a distance x of material. The nuclear interaction length is generally larger than the radiation length and photon attenuation length in most materials. Also, charged hadrons will lose energy due to ionization when they pass through material, which can be detected in a calorimeter, while neutral hadrons will pass unnoticed until there is a hadronic interaction.

2.2.5 Hadronic Showers

Hadronic showers are the result of a hadronic interaction occurring in a material, leading to further hadronic interactions and (usually) electromagnetic ones too. A hadronic shower can contain many different types particles, which may interact or decay in different ways. This means hadronic showers are naturally less predictable than electromagnetic ones. Furthermore, since the nuclear interaction length is usually longer than

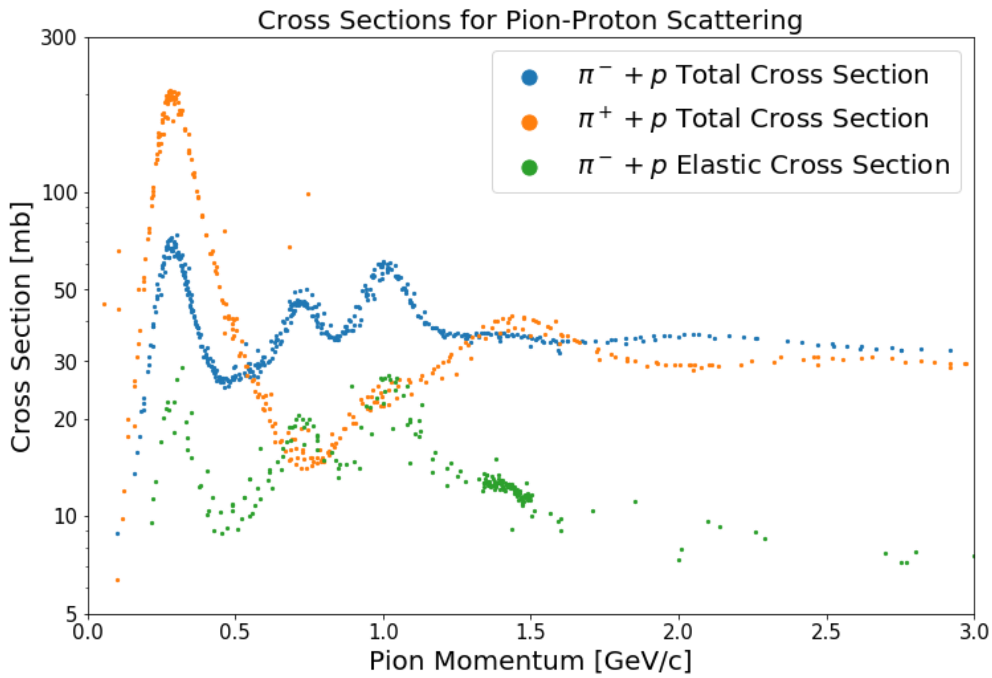

Figure 2.5: Cross sections for pion-proton scattering. Error bars are small in this momentum regime, so they have been omitted. Data taken from [7].

the photon attenuation length and radiation length, hadronic showers usually penetrate deeper and wider than electromagnetic showers on average. This makes hadronic calorimetry generally more difficult in comparison to electromagnetic calorimetry. Specially made hadronic calorimeters are common in particle physics experiments, but the energy scale of Belle II makes hadronic calorimetry less viable. Hadronic showers develop in both the electromagnetic calorimeter and the long-lived kaon and muon detector at Belle II. These detectors will be covered in section 3.2.

Chapter 3

The Belle II Experiment

The Belle II experiment [5] is hosted by the The High Energy Accelerator Research Organization, known as KEK, in Tsukuba, Japan. It follows from the Belle experiment [29] (1999-2010), and started taking data in 2018 after substantial upgrades to the detector and SuperKEKB collider [6]. SuperKEKB is known as a B factory since it's primary use is to produce B mesons from electron-positron collisions. Belle II aims to measure the decay chains of these B mesons to search for new physics (NP) in the flavour sector of the Standard Model and to make the most precise measurements of certain Standard Model (SM) parameters among other secondary goals [30]. This chapter runs through the technical details of the SuperKEKB collider and the Belle II detector. Information is pulled from the Belle II Technical Design Report [5] unless otherwise stated.

3.1 The SuperKEKB Collider

SuperKEKB is the collider which sources the collisions for Belle II. It is a double-ring electron-positron collider consisting of the electron high energy ring (HER) and the positron low energy ring (LER), which accelerate electrons and positrons to energies of 7 GeV and 4 GeV respectively. Electrons and positrons are sent to the rings from a injector linear accelerator that contains a damping ring for the positrons. The beams from the HER and

LER are focused to a small region called the interaction region where their constituent electrons and positrons may collide at a center of mass energy of 10.58 GeV, which is almost exactly the mass of the $\Upsilon(4S)$ meson. This encourages the production of $\Upsilon(4S)$ particles, which then decay to B mesons.

What gives SuperKEKB its namesake is the world leading luminosity it aims to achieve. The current target luminosity is 6×10^{35} cm^{-2}s^{-1} [31], an order of magnitude higher than the previous iteration of the collider, which held the previous record for luminosity. This ultra-high luminosity allows for frequent production of B mesons which then means greater statistical precision for the NP searches and SM measurements Belle II is making. To achieve this high luminosity,every part of the collider was upgraded, with special focus on the two rings themselves, which will double the previous beams' currents, and the final-focus system, which now uses the nano-beam collision scheme. Basically, this scheme squeezes the beams to reduce the area in which they interact and is mainly made possible through the upgrade to the final-focus system [6].

3.2 The Belle II Detector

The Belle II detector, outlined in figure 3.1 is a cylindrical detector surrounding the interaction region of the collider. It is a general purpose detector designed to collect information required to reconstruct B decay chains. This includes high spatial resolution vertexing, precise tracking of charged particles within a solenoidal magnetic field, particle identification, accurate photon calorimetry, and a fast data acquisition and trigger system. All of which needs to be done quickly and with consideration to increased backgrounds due to higher luminosity.

The detector has three regions that are referred to as the backwards end cap, barrel, and forwards end cap. These names come from the direction of the total momentum in the lab frame, with forwards being the direction in which the (higher energy) electrons are going. The barrel is simply the circular extrusion that goes between the end caps. It is

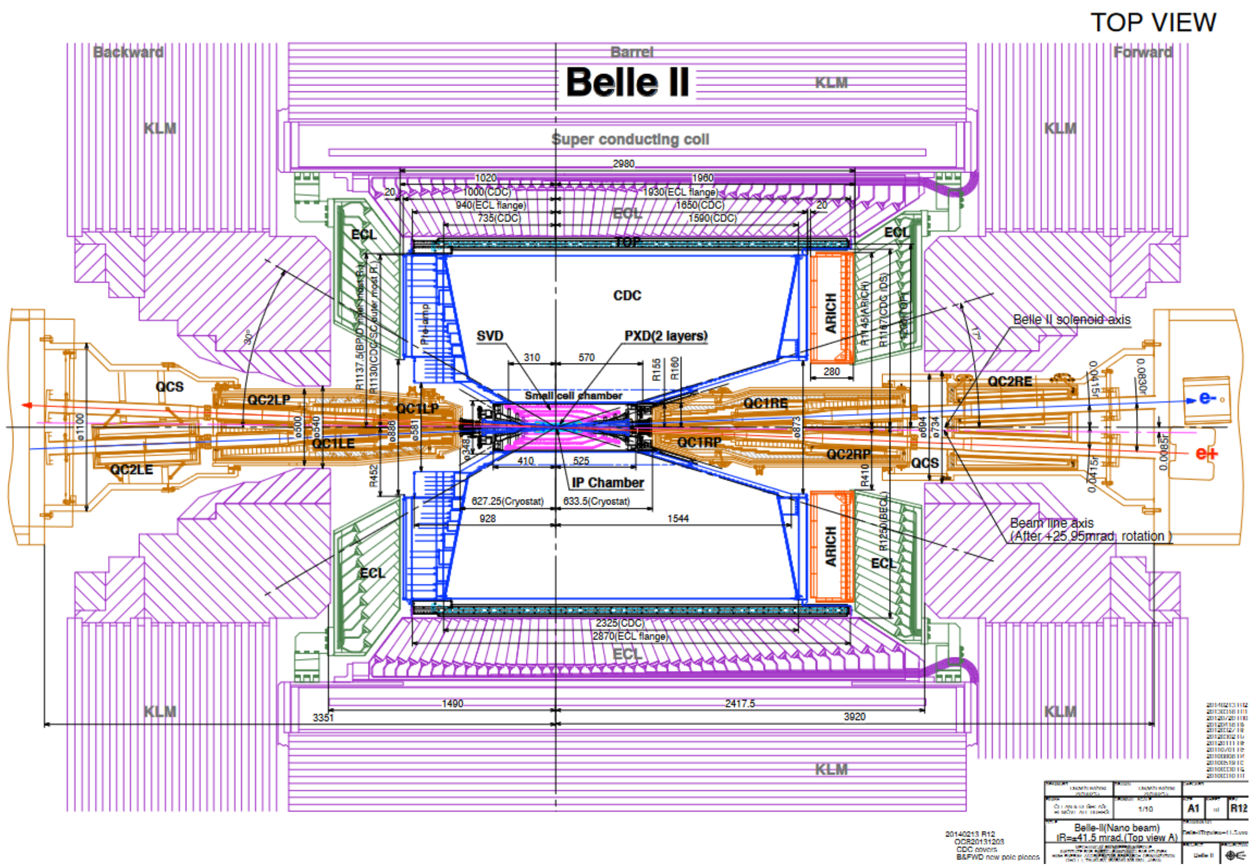

Figure 3.1: Belle II detector schematic, top view [30].

common to use cylindrical co-ordinates given the geometry of the detector, with the origin at the interaction point (IP) and the z-axis along the beam lines, the positive direction towards the forward region. When referring to radius in the x-y plane (cylindrical radius), ρ will be used, while distance from the origin (spherical radius) will be r. In spherical co-ordinates, the detector's region of acceptance is the entire range of ϕ, that is 0° to 360°, and from $17°$ to $150°$ in θ, though acceptance for certain sub-detectors is different.

3.2.1 Tracking and Vertexing

The detector closest to the IP is the the pixel detector (PXD), which is followed by the the silicon vertex detector (SVD). Together, these detectors make up the vertexing detector (VXD) which covers the entire range of the azimuthal angle, ϕ, and $17°$ to $150°$ in the

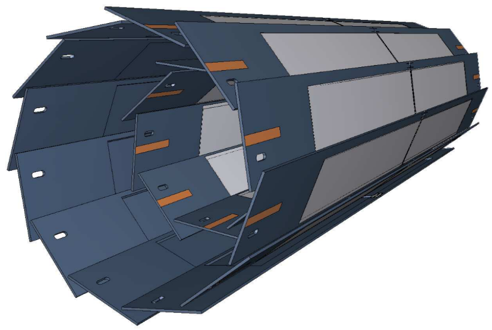

(a) PXD

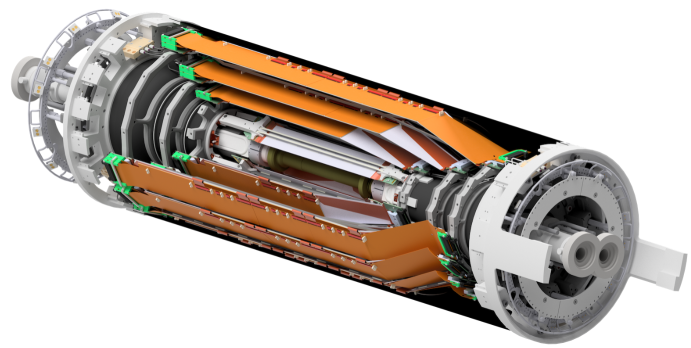

(b) VXD

Figure 3.2: CAD renderings of the PXD and SVD. The area on the PXD in grey are the active DEPFET sensors. Note that the SVD is tilted in the forward region.

polar angle, θ. The PXD consists of two layers of pixel detectors, at radii $\rho = 14, 22$ mm. Pixel detectors are needed close to the IP since the increased luminosity yields more backgrounds which have a larger flux as you get closer to the IP. Strip detectors would have an occupancy too high to make tracking possible. The pixel detectors make use of DEPFET (DEPleted Field Effect Transistor) technology which allows for thin pixels, important for preventing too much multiple scattering. The detector contains 10^7 readout channels for pixels ranging in size from $50 \times 50\,\mu\mathrm{m}^2$ to $50 \times 85\,\mu\mathrm{m}^2$.

The SVD exists so that there are more layers of high spatial resolution tracking information that can be quickly read out. It has layers at radii $\rho = 38, 80, 115, 140$ mm. Each layer is equipped with double sided silicon strip detectors, with strips at right angles such that they can provide 2D position information. There are 2.45×10^5 thousand readout channels for strips that range from 50 to 250 μm in width. The paths traced through the vertex detector can serve as the beginnings of tracks seen in the larger tracking detector.

The tracking detector for Belle II is called the central drift chamber (CDC). The CDC envelopes the VXD and has 14,336 sense wires from a radius $\rho = 160.0$ mm to $\rho = 1111.4$ mm. Combined with the 1.5 T magnetic field provided by a solenoidal superconducting magnet, the CDC is mainly used to measure momentum of particles from the helical paths of ionization they leave behind in the 50-50 mixture of helium and methane gas that fills its volume. The CDC achieves 3D spatial resolution through alternating layers of ”axial” and ”stereo” wires, where the axial wires are aligned in the z-axis, while the stereo ones are skewed with respect to the axial ones. Its acceptance is the same as that of the VXD.

Vertexing is key to determining the intermediate states between final state particles (those that are directly detected in the detector) and the initial B meson pairing. This is done by finding intersections of tracks measured by the high precision tracking detectors of the VXD. These high precision tracks are matched to CDC tracks to infer their momentum, charge, and particle identification information to reconstruct the most likely decay chains. The tracking detector's relative resolution of transverse momentum is less than 0.5% for tracks with transverse momenta 400 MeV/c, and becomes larger for tracks with lower transverse momenta, up to 10% for tracks with transverse momentum 50 MeV/c [32].

3.2.2 Particle Identification

Particle identification may come in many forms, one example is how the amount of ionization left in the CDC is different from particle to particle, and so it may be measured and used to identify them. However, Belle II has two detectors, the time-of-propagation (TOP) counter and the aerogel ring imagining Cherenkov detector (ARICH), dedicated to charged particle identification. The TOP covers the barrel region or 31° to 128° in θ, while the ARICH covers the forward end cap or 14° to 30° in θ. The entire range of ϕ is covered by each detector. Both detectors identify particles using Cherenkov radiation.

The TOP is a special kind of Cherenkov detector which totally internally reflects Cherenkov light in a quartz radiator as depicted in figure 3.3. This allows for the measure of the Cherenkov angle via the time it takes the Cherenkov photons to propagate through the radiator as well as the position in which they are detected in the photon detector at one end of the radiator. A spherical mirror is introduced on the other end of the radiator such that light emitted in the direction opposite to the photon detector can be analyzed. Multichannel plate photo multipliers (with 16 channels) are used to detect Cherenkov

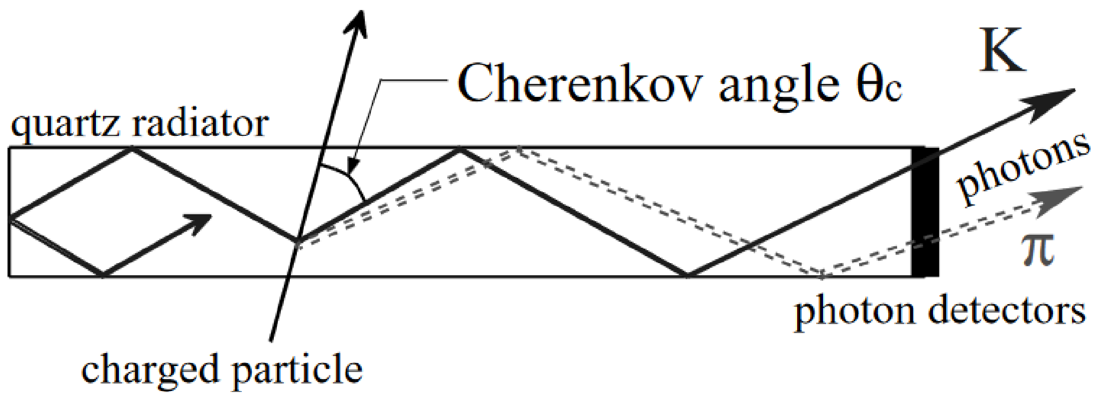

Figure 3.3: Sketch of working principle for the TOP [5]. Paths of Cherenkov photons are traced for kaons (solid line) and pions (dotted line).

photons since they offer great timing resolution, appropriate position resolution, and can operate in magnetic fields. There are 16 TOP modules, each containing a quartz bar that is 45 cm wide, 2 cm thick, and 260 cm long [30].

The aerogel ring imaging Cherenkov detector (ARICH) is a proximity focusing ARICH, meaning it is made from a radiator, followed by an expansion volume for the Cherenkov photons to spread until they reach photon detectors that measure their position. The radius of the ring together with the expansion volume thickness is used to compute the Cherenkov angle. The Belle II ARICH uses a novel method to achieve a higher rate of Cherenkov photon production while minimizing the uncertainty from the unknown emission point. This method employs two 2 cm thick aerogel radiators of differing refractive indices, chosen such that the Cherenkov rings from each radiator coincide once reaching the photon detectors as seen in figure 3.4. Hybrid avalanche photon detectors (HAPDs) are used to detect photons. They consist of a photocathode, a 2 cm drift region with a 8 kV potential difference, and an pixelated avalanche photo-diode (APD). These HAPDs have 144 channels over a $73 \times 73\,\mathrm{mm}^2$ area.

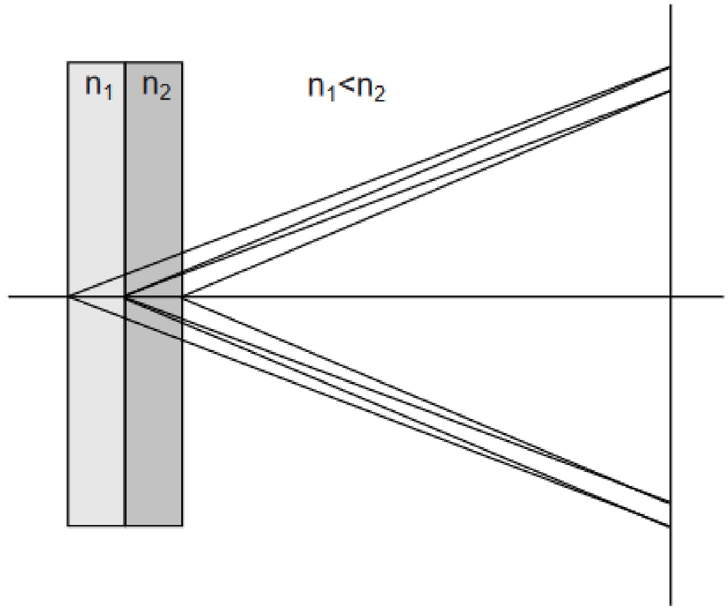

Figure 3.4: Sketch of working principle for dual radiator proximity ARICH. The lines indicate the outer bounds of the Cherenkov rings. The bounds from each radiator coincide at the right hand side, where photon sensors would be.

3.2.3 Electromagnetic Calorimeter (ECL)

The electromagnetic calorimeter (ECL) in Belle II is the only tool able to measure the energy and direction of photons. It does this by measuring scintillation light from electromagnetic showers made by photons in thallium doped caesium iodide crystals. There are 8736 crystals which come in the form of truncated pyramids with an average cross sectional area of $6 \times 6\,\mathrm{cm}^2$ and 30 cm in length, all of which point towards the interaction point. This corresponds to 16.1 radiation lengths or 0.8 nuclear interaction lengths. Each crystal has two photodiodes glued to its rear surface to read out the scintillation light. This setup capable of a photon energy resolution, $\sigma E/E$, of $\tilde{2}$% for photons from 50 MeV to 4000 MeV. The ECL lies just outside the particle identification detectors at a radius of $\rho = 125$ cm, with the backwards end cap 1.02 m behind and the forwards end cap 1.96 m in front of the interaction point. The coverage of the ECL extends past the coverage of the inner detectors, from 12.4° to 155.1° in θ and includes the entire range of ϕ. However, there are two $\sim 1^\circ$ gaps between the barrel and end cap regions. Photons will generally interact in these gaps, but the energy resolution will be degraded due to the lack of active detector.

The readout electronics for the crystals provide high resolution timing of the light pulse and records samples of the waveform. The shape of the waveform is used for two reasons. One is to account for pile up, where showers from a previous (background) event continue to cause scintillation. The other is so that the pulse shapes can be used to discriminate true photons from particles that minimally ionize and/or hadronically interact in a crystal, both of which are processes that have distinguishable waveforms in thallium doped caesium iodide [33].

3.2.4 K_L^0 and Muon Detector (KLM)

The K_L^0 and muon detector (KLM) is the outermost sub-detector, and the only one that lies outside of the superconducting solenoid. As the name suggests, its purpose is to detect and identify long lived kaons and muons. It does this through a sampling device setup of alternating 4.7 cm thick iron plates and active detector material. The 14 iron plates serve as the magnetic flux return for the magnet and provide ~3.9 more nuclear interaction lengths in which K_L^0s can hadronically interact or muons can slow via ionization. The polar angle (θ) coverage of the KLM is $25°$ to $155°$. The end cap and barrel regions overlap around $40°$ and $129°$, which varies the amount of material with which a particle can interact.

In the barrel region, there are 15 layers of active detectors, the first two being scintillator strips, and the others being glass electrode resistive plate chambers (RPCs). The end cap regions have 14 layers of detector material, all of which are scintillator strips. The scintillator strip and RPC layers are capable of detection in orthogonal directions, allowing 2D position resolution. In total, there are 17×10^3 readout channels for the end caps and 32×10^3 channels for the barrel. The scintillation light is readout through wavelength shifting fibre optics which feed to silicon photomultipliers.

The KLM may distinguish muons and K_L^0s by the pattern of hits they leave through it and if there is a track in the CDC that points to the location of said hits. Muons leave hits in successive layers along a straight line, forming a track, while neutral kaons will undergo a hadronic shower leaving spread out hits in a region of the detector, potentially skipping layers. Also, neutral kaons will leave no track in the CDC. Charged pions and kaons that make it through the ECL, which happens $\sim$ 50% of the time at high momentum (>1 GeV/c), may also hadronically interact in the KLM, mimicking a neutral kaon. However, again tracks in the CDC can be used to discriminate these KLM clusters from true neutral kaon ones most of the time.

Chapter 4

Analysis Software and Techniques

A large and complicated detector dictates an equally large and complicated software for abstracting and analyzing the massive amounts of data it collects. The Belle II analysis software framework [34], simply called basf2, is the open source software developed and used by the Belle II collaboration for essentially every aspect of the experiment. This includes simulation, the handling of real data, reconstruction, and high-level physics analyses.

The vast majority of the software comes in the form of various python packages that are primarily written in C++. Usually each package encompasses a broad use, like reconstruction for a certain detector or some high-level analysis procedures. Software that isn't developed within the Belle II collaboration, but that is required to run basf2 is called external software or externals. Summarizing each aspect of the entire software framework would be an immense task, so this chapter will only summarize relevant parts and corollaries to certain software choices. The information in this section is true for `release-06-00-14` of basf2 [35] unless otherwise stated.

4.1 Simulation Software

Simulation is used when designing a detector, estimating systematic error in an analysis, evaluating detector performance, and more. It is a challenge to create a simulation that is quick and accurate over a wide range of particles, energies, and interactions. For this reason, Belle II makes use external software package called Geant4 [36] and EvtGen [37]. Both of these packages are based on the Monte Carlo (MC) method. This method is so pervasive in high-energy physics, when describing things related to simulation ″MC″ is often used as a noun and adjective. To fully simulate an event, the geometry and properties of the materials within the detector are imported and EvtGen is used to simulate the early physics processes related to B meson decay, which give rise to ″primary″ particles that can enter the detector volumes. In the detector volume, Geant4 is used to simulate the interactions of the particles in matter and Belle II has built simulations of the detector response to these interactions.

Within Geant4, a physics list determines which processes must/can be simulated. A common list for high-energy physics is `FTFP_BERT`, but Belle II has made a custom physics list. This was done because `FTFP_BERT` is a reference list meant for higher energy experiments like those at the LHC. To tune the physics list to Belle II energies ($<$ 11 GeV) the overlap between the two main hadronic interaction models have been altered as described by the following. For final state hadrons (pions, kaons, and protons), the Bertini cascade model is used when the particle is under 12 GeV. At energies above 5 GeV for protons and 10 GeV for pions and kaons, the FTFP model is used. Both of these models are described in [38]. Wherever these energies overlap, one is chosen by a random number, with probabilities weighted depending on the energy of the particle. Belle II has shifted the overlaps such that the Bertini model is used more than the FTFP model, which should improve data/MC agreement. There are many different models and sub-models used (other than the two above) to cover the entire energy range and types of interactions in Belle II. This is all to say, the modelling of inelastic hadronic interactions is quite difficult at certain energies and not perfectly done at Belle II.

When Geant4 simulates a particle interaction, ”secondary” particles are produced. However, low energy secondary particles can be produced at high rates in some physics processes. Therefore, it is much easier to model these particles as some sort of energy deposition over a certain length under a certain energy threshold. Even still, thousands of secondary particles that don’t meet this threshold can remain in the simulation, vastly increasing the space needed to store simulation data. To combat this, secondary particles are simulated and seen in the detector response, but their exact information is not written to disk. Then, their detector response is assigned to their parent particle or left unassigned to any particle. This will be important for truth matching in the section 4.2. However, in some cases it is important to save the secondary particles, and this can be done by tuning a parameter in the simulation software. In this case, all secondaries above a threshold energy will be saved.

Lastly, in some cases it is convenient to simulate specific particles rather than entire physics events. With basf2 this can be done with a module[1] called `ParticleGun`. In this module, the types, number, momenta, and production location of primary particles can be custom set. This can be done to see how the detector responds to and reconstructs specific situations found at Belle II.

4.2 Reconstruction

When an event occurs, whether it be real data or simulation, there is information from each readout channel from every detector. To make this manageable and interpretable, basf2 aims to make a one-to-one correspondence between detector data and single final state particles. The data is collected into data objects meant to represent the detector response to a particle. These objects can be vertices from the VXD, tracks in the CDC,

[1]A module can be thought of as a special function in basf2. Modules hide much of the work that goes into passing all of the data objects from function to function.

ECL clusters, or KLM clusters. Each of these is a basf2 data object available to analysts, rich in information. Furthermore, tracks can be matched to any other object after passing some criteria, pairs of ECL clusters can be used to reconstruct neutral pions (since they decay into two photons), and other higher level reconstruction operations can occur. Once this is done, basf2 yields the clearest picture of the event possible and can (ideally) fully reconstruct a B meson decay chain or other $e^+ + e^-$ events. Of course, it is rarely this easy. The following sub-section will act as a primer to understand one of the many ways reconstruction can go awry.

4.2.1 ECL Clusterization and Track Matching

Of interest for this thesis is the way in which readings from ECL crystals are clusterized. Electromagnetic showers within the ECL at Belle II often can be seen in more than one CsI(Tl) crystal due to geometric effects (a particle could interact near the interface of two crystals) or they have a lateral distribution[2] that can be measured outside the range of an individual crystal, which is approximately 6×6 cm^2. Therefore, to capture all of the information of a photon shower, the readings from the crystals in the region of the photon shower must be put together to form a cluster. This clusterization process is described by [30] and [39], although some details from these sources may differ from the implementation for release-06-00-14.

First, the scintillation light is collected and the waveform processed. A 32-bit word, called an `ECLDigit`, containing information on the amplitude and timing of the signal is the most basic ECL data format. This is then corrected via multiple calibration steps that are crystal dependent. Next, ”connected regions” are created at ”seed” crystals, which are `ECLDigit`s over 10 MeV. Crystals neighboring a seed crystal are added to its connected region if they are above 0.5 MeV. If the neighbor is above 1.5 MeV, the connection process continues to its neighbors. At the end of this there usually exists many connected

[2]CsI has a Moliére radius, i.e. a lateral radius in which 90% of the EM shower energy is contained, of 3.5 cm.

regions. Sometimes, connected regions will overlap, having two or more `ECLDigits` over 10 MeV. Local maximums will be searched for within the connected region. When a local maximum is found, the nearest 24 `ECLDigits` of the square arrangement of 5x5 crystals around the maximum are reconstructed as an object called an `ECLShower`. If the connected region has multiple local maxima (although it is rare to see more than 2), the connected region is split into two showers, where the overlapping crystals split their energy between each shower following one of two methods. The methods are based on the hypotheses in which the two maxima within the connected region arise. One is called ”N photons”, where it is expected the two local maxima arise from photons that hit the ECL close together. The other hypothesis is called ”neutral hadrons”, where it is expected there was a hadronic interaction from a neutral hadron in the ECL, in which usually only a few particles carry most of the energy of the shower. These particles may go off in different directions, decaying or causing further interactions that lead to multiple maxima in the connected region. The details of how they are split will not be described here.

Once ECL showers and tracks have been reconstructed, they may be matched to each other to provide a full picture of the particle that caused them. This is done in two ways. The first, and preferred way, is analyzing the crystals the extrapolated track traverses and taking the highest energy shower (per shower hypothesis) containing said crystals to be matched to the track. The other method is by matching ECL showers near the point at which the extrapolated track reaches the ECL. This is used for low transverse momentum tracks reaching the forwards end cap ECL or high transverse momenta in the barrel ECL, and only if the previous method of matching has failed. From the `ECLShower` objects a position, energy, shower shape, and pulse shape discrimination can be calculated. Only showers over 20 MeV are saved as ECL clusters and only one cluster may be matched to a track.

4.2.2 Truth Matching

Truth matching, also called MC matching, is the bridge between reconstructed objects and the simulated particles that caused them. The goal is to assign a simulated particle to the reconstructed object arising from it. Obviously, truth matching is not possible in real data since there are no simulated particles, only real ones. Furthermore, truth matching is not a perfect science even when every particle is simulated in an event. Truth matching is only supposed to happen after reconstruction occurs. At this point, information pertaining to secondary particles has been removed, so their relationships with reconstructed objects can be dealt with in a number of ways. In the ECL (and some other detectors), the energy depositions of the secondary particles are assigned to the primary particles, but this still is not perfect because of the ECL's truth matching algorithm.

Truth matching for ECL clusters is based on how much of the ECL cluster's energy comes from a specific particle, and in turn if that particle's energy makes up most of the ECL cluster's energy. Specifically, an ECL cluster will only be matched to a simulated particle if the particle makes up more than 20% of the cluster's energy, and the cluster is more than 30% of the simulated particle's energy. These percentages were optimized to match photons, which the ECL is designed to detect, but there are issues when certain charged particles enter the ECL. For instance, if a 1.2 GeV muon leaves a characteristic MIP energy deposition of 200 MeV, it will not be matched by the method described above. The ECL cluster energy would not make up enough of the muons total energy to be matched. However, the muon leaves a track in the CDC which has its own truth matching algorithm, described in [32]. Since the CDC is well equipped for charged particles, this matching algorithm is better for muons and therefore will override the ECL truth matching algorithm for that cluster (via the track-ECL cluster relationship set by the track-cluster matching algorithm). However, if a charged particle leaves more than one ECL cluster, the clusters not matched to the track will seek an MC match via the ECL matching algorithm, and once again there will be an ECL cluster with no MC match.

As another example, consider many secondary particles from an inelastic hadronic interaction leading to two or more ECL clusters. The energy of each ECL cluster mainly comes from secondaries arising from the inelastic interaction. The relationships between the clusters and the secondary particles will be reassigned to the incident primary particle. If one cluster has less than 30% of the energy of the primary hadron, it will not be MC matched. Furthermore, even if it did pass the matching criteria, an MC particle can only be matched to one of each type of reconstructed object. This means if a particle creates more than one ECL cluster, only one of those clusters may be matched to it.

Truth matching is important to verify the reconstruction and interpretation of events. In most physics analyses, truth matching is highly effective. Its failures described above are border cases where the ECL energy is not being properly associated to the particle incident on the ECL (or its daughters). This problem with ECL energy is arguably the cause of the problems in truth matching. It also leads the reconstruction algorithms at Belle II to reconstruct objects that don't actually correspond to particles coming from the B decay chains. When this happens in the ECL, the clusters are called "spurious photon candidates" or just "spurious photons".

4.3 Spurious Photons

For an ECL cluster to be considered a photon, it must be over 50 MeV in energy and not have a track matched to it. These conditions are meant to accept photons descending from B decay chains while reducing photon clusters from noise. Spurious photons arise in a number of ways at Belle II. Non-collision sources from the electron and positron beams, known as "beam backgrounds" [40] and bremsstrahlung radiation from charged particles traversing the CDC both give off photons that are detected in the ECL, but don't descend from the B decay chain. These sources are studied independently and are beyond the scope of this thesis.

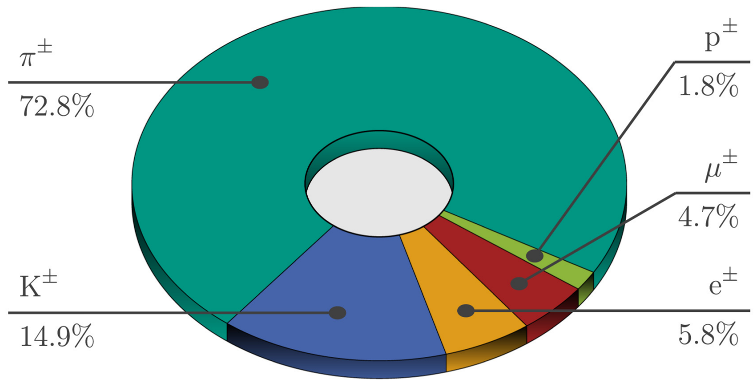

Figure 4.1: Relative abundance of charged final state particles in simulated $\Upsilon(4S)$ events [32].

Of interest for this thesis are spurious photons coming from charged particles traversing the ECL. When the charged particle is a hadron, it may inelastically interact with a nucleus, causing a hadronic shower, described in section 2.2, that can either have multiple local maxima in a connected region (resulting in multiple ECL clusters) or even form multiple connected regions that get clusterized. Spurious photons from hadronic interactions in the ECL are called hadronic split off (HSO) clusters or simply hadronic split offs. Figure 4.1 shows the relative abundance of charged particles coming from a simulated $\Upsilon(4S)$ event. The vast majority ($\sim$ 90%) of charged particles are hadrons.

Another common way spurious photons are formed is low transverse momentum (LPT) clustering. This occurs when a particle has a low momentum in the transverse direction (radially away from the beamlines), so it tightly curls in the CDC, increasing the path length it traverses in the ECL. If the particle is a MIP, a long trail of ionization will be left, causing a large connected region. Geometric effects from the shape of the crystals and the direction across which the particle travels could cause multiple local maxima in the ECL, leading to multiple clusters. This occurs for particles with enough transverse momentum to reach the ECL in the barrel (above 0.3 GeV/c). In the endcaps, the particles momentum in the Z direction (along the beamline) becomes important when considering the length of its path through the ECL. Figure 4.2 shows the distribution of transverse momentum for charged particles from simulated $\Upsilon(4S)$ events. There is clearly a large

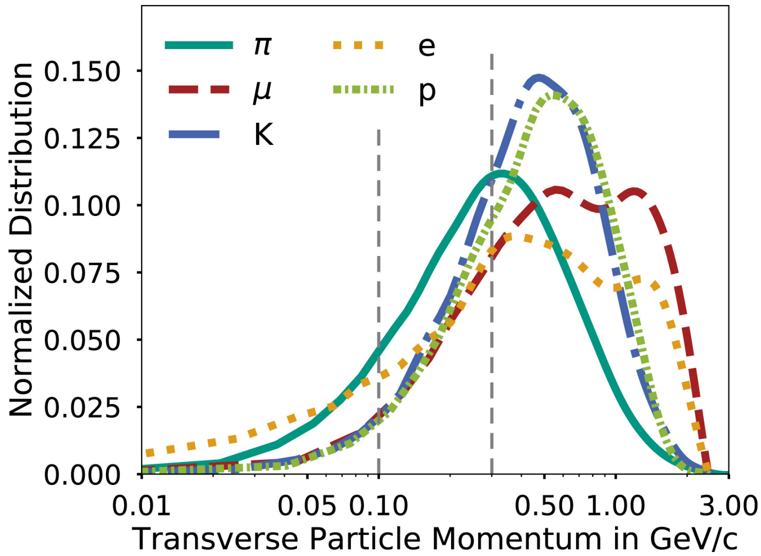

Figure 4.2: Distributions of transverse momentum for final state particles in simulated $\Upsilon(4S)$ events [32]. The distributions are normalized to the total number of tracks of the respective type and plotted on a logarithmic x-axis. The dotted line at 0.3 GeV/c corresponds to particles that will curl in the CDC (i.e. not reach the barrel ECL).

amount of particles above 0.3 GeV/c. The high transverse momentum cutoff for LPT clustering is not well defined, and is therefore a goal of the research in this thesis (see section 5.3).

Furthermore, if the particle is a hadron, the larger path length increases the likelihood of a hadronic interaction, potentially causing more spurious photon clusters. The increased path length through the ECL also increases the likelihood of a particle decaying in the ECL. Particles will slow while in the ECL, reducing their Lorentz boost leading to a higher likelihood of decay. When this happens, some of the mass of the parent particle is converted to kinetic energy, which can then be deposited in the ECL, causing another connected region or local maximum, leading to more clusters.

4.4 ECL Cluster Multiplicity Effects

There are many reasons spurious photons are bad for Belle II. For one, they are a computational strain since they contain information irrelevant to physics analyses, and two, the primary ECL cluster (matched to the track), is missing information that could be used for particle identification[3]. However, a more general way in which spurious photons cause problems is by raising the multiplicity (the number of clusters) in the ECL. This has negative effects on the reconstruction of neutral pions and a variable called extra energy that is used to increase signal purity in physics analyses. This section provides a detailed description how these problems arise and the latest Belle II efforts to combat them.

4.4.1 π^0 Reconstruction

Since a neutral pion almost always decays to two photons, the ECL is the only detector that contains information to reconstruct them. This is done by simply pairing up any two ECL clusters that pass certain energy cuts (and sometimes energy density cuts), then checking their invariant mass (and sometimes the angle between them). In an analysis, a user has a choice for how efficiently[4] they want to reconstruct neutral pions. The most efficient cuts, amounting to an efficiency of 60%, require ECL clusters to be over 200 MeV (or more, depending on the detector region) and form an invariant mass less than 300 MeV/c^2. The cuts for the lowest efficiency of reconstruction, which is 10%, require the clusters to have energies higher than 100 MeV (or more, depending on the detector region), but also have the central crystal contain 50% of the energy of all the crystals, including itself, in the 3x3 region of around it, which occurs more often for photon clusters than other clusters. The cuts on the reconstructed neutral pion are that it has an invariant mass between 127 MeV/c^2 and 139 MeV/c^2 (recall $m_{\pi^0} = 135\,\mathrm{MeV/c^2}$) and that the constituent photons are measured within an opening angle of 0.8 radians and are within 0.9 radians in the azimuthal angle. These cuts are varied to achieve efficiencies at every multiple of ten between 10% and 60%, and the user will choose the neutral pion sample that yields the best results for their analysis.

[3]Specifically E/p measurements that are typically used to identify electrons [30]. Though full shower shapes could also help here.

[4]Efficiency here is the number of reconstructed neutral pions over the number of real neutral pions.

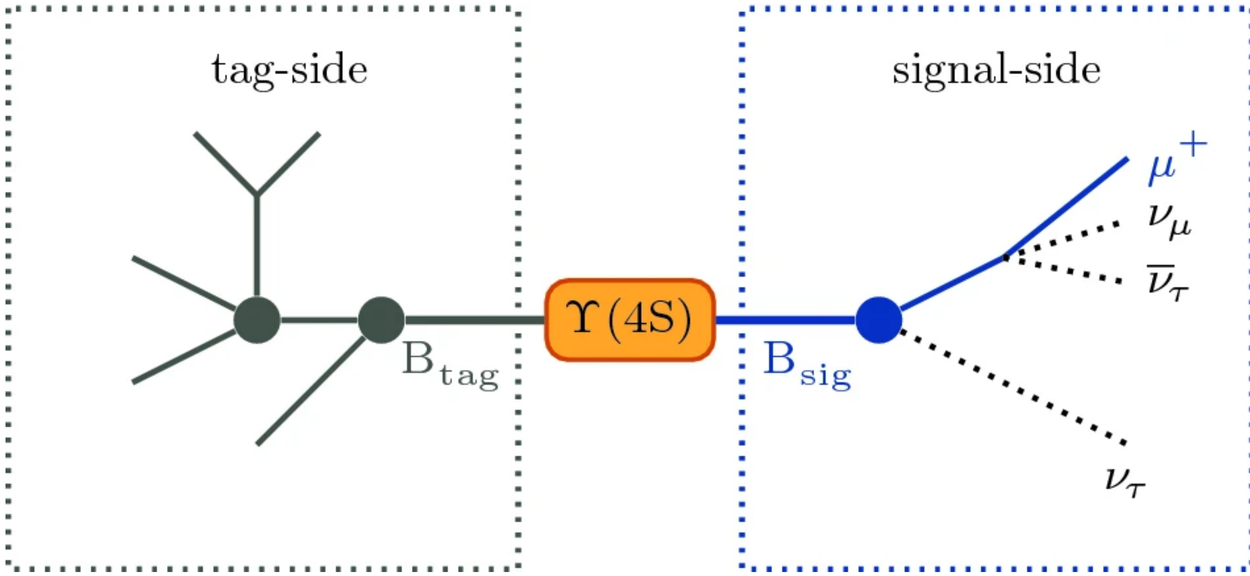

Figure 4.3: Schematic overview of an $\Upsilon(4S)$ decay. The left side is a typical tag side decay while the right is a typical signal side decay. The sides may overlap in the detector and there is no way of knowing which particles belong to each side a priori [41].

This is all to say that spurious photons create combinatoric backgrounds for neutral pions, greatly increasing the number of neutral pion candidates. One goal of better handling ECL backgrounds (spurious photons) is to reconstruct neutral pions with greater purity at higher efficiencies. Furthermore, the computational burden of reconstructing neutral pions can be greatly decreased by omitting spurious photons, speeding up physics analyses and productivity.

4.4.2 FEI and Extra Energy

The full event interpretation (FEI) [41] is an algorithm developed for Belle II that uses machine learning to automatically identify possible B meson decays based on reconstructed data in an event. This allows for one B meson of an $\Upsilon(4S)$ event to be "tagged" which then allows a user to search the rest of the detector data for their "signal" B meson decay chain as in figure 4.3. This type of analysis allows the full reconstruction and interpretation of an event, including the kinematics.

What is left over after fully reconstructing the $\Upsilon(4S)$ is the "Rest of Event" (ROE). If an event is reconstructed properly, one would naively assume there should be nothing left in the ROE. Therefore it would be wise to assume that the reconstruction is false when something is left in the ROE. However, this is rarely the case in real data. Correctly reconstructed events still have objects in their ROE, but incorrectly reconstructed events usually have more left over. One way to quantify the amount left in the ROE is to sum up the energy of the left over ECL clusters. This sum is called the ROE extra energy. In an analysis that uses FEI, it usually increases signal purity to cut out candidates when there is a large ROE extra energy.

Spurious photons are one of many components that add to the ROE extra energy, but when they do, the event may still be correctly reconstructed since the track from the charged particle responsible for the spurious photons is all that is needed. If spurious photons were removed from the ROE extra energy calculation, it would be a better measure for when reconstruction went wrong, thereby improving signal purity in a host of analyses. When this was done using the most recent method of removing spurious photons, described in the next subsection, on a $B^0 \to D^{*-}l^+\nu$ analysis, it increased the signal significance (from a cut on ROE extra energy) from 4.10 to 10.08 [42].

4.4.3 Spurious Photon Discrimination

The recently developed `fakePhotonSuppression`[5] variable [42] is the current method for discriminating spurious photons from non beam background and bremsstrahlung sources. As will be shown in Chapter 5, the majority of these spurious clusters can be attributed to LPT clustering and HSO. `fakePhotonSuppression` is a multivariate analysis (MVA) based on six ECL cluster variables that have been found to contain differences between true photons and spurious photons. They are

[5]In previous studies, certain spurious photons have been called fake photons. However, this can be confusing since some fake/spurious photons come from actual photons such as those from π^0 in a hadronic cascade.

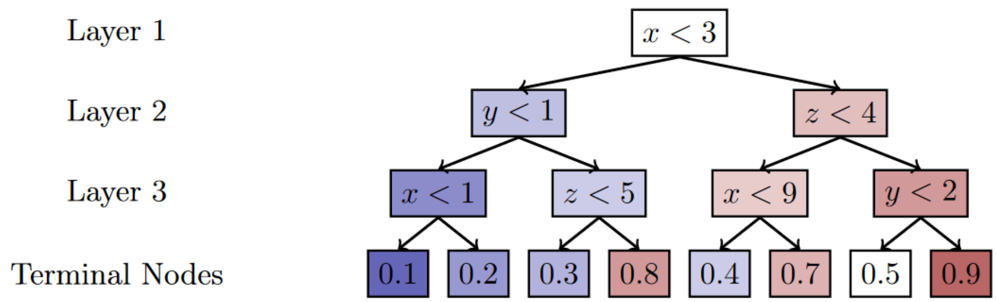

Figure 4.4: An example of a three layer decision tree. A data-point traverses the tree from top to bottom. A decision is made at each node of the tree until a terminal node is reached, which contains the probability of the data-point to be "signal" based on training data. Figure taken from [45].

- `clusterPulseShapeDiscrimintationMVA`, a variable based on the pulse shape seen in the ECL crystals that make up the cluster [43]. It returns 1 when the pulse shape is photon-like and 0 when it is hadron-like
- `minC2TDist`, the distance of the ECL cluster to the nearest track hitting the ECL
- `clusterZernikeMVA`, a variable based on the shower shape (quantified by Zernike polynomials) of the cluster [44]. It returns 1 when the cluster is symmetric and tight (photon-like) and 0 when it is hadron-like
- `clusterE`, the energy of the ECL cluster
- `clusterTiming`, the time after the collision of the ECL cluster
- `clusterTheta`, the polar angle of the ECL cluster

The MVA is in the form of a FastBDT [45], a machine learning algorithm developed for Belle II. FastBDT is a stochastic gradient-boosted decision tree algorithm, which is based on a decision tree algorithm, which makes a number of consecutive cuts as shown in figure 4.4. A boosted decision tree improves upon regular decision trees by sequentially constructing shallow decision trees during the fitting phase to avoiding over-fitting. Finally, stochastic gradient descent is used to optimize the training time of the algorithm.

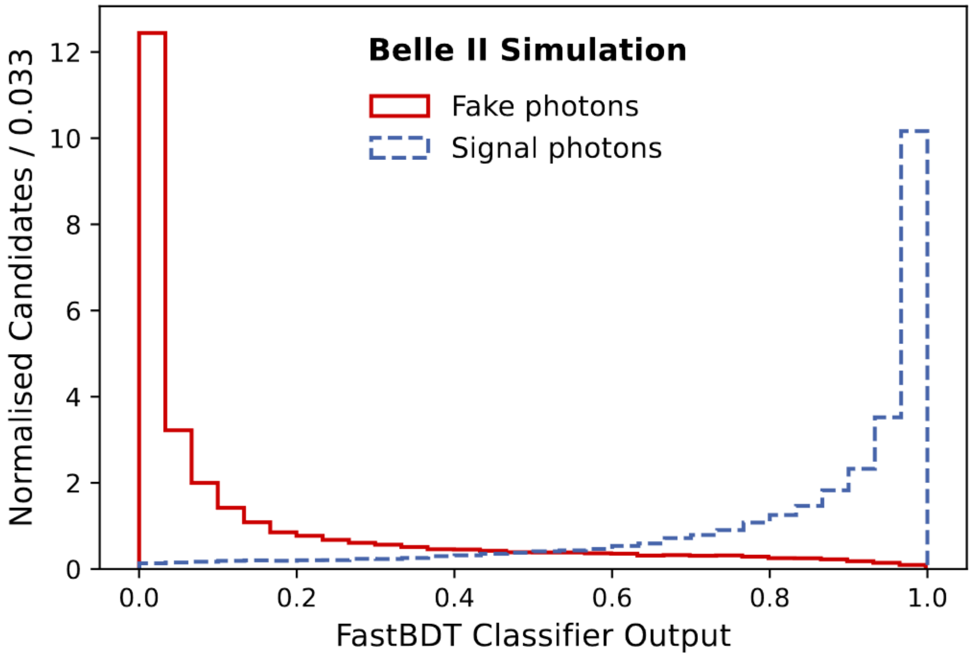

Figure 4.5: Distribution of the spurious photon classifier output. The output represents the probability of the photon candidate to be a signal photon (from the B decay chain). The distribution is normalized to 1. Taken from [42].

The training sample includes signal photons and (non-beam background nor bremsstrahlung) spurious photons selected from photon candidates reconstructed from simulated $B^0\overline{B}^0$ events with simulated background overlay [40]. Photon candidates are ECL clusters that have energies greater than 50 MeV and a polar angle that falls within the acceptance of the ECL. Signal photons are selected as "true" photons (ECL clusters that are truth matched to simulated photons), ensuring they arise from the collision event. Spurious photons are selected as photon candidates that are not truth matched to primary particles from the B decay chains, but still have $\geq$ 53 MeV of their energy coming from particles descending from the decay chain. The training sample included 420,000 signal photons and the same amount of spurious photons. The output of this FastBDT can be seen in figure 4.5. Clearly, `fakePhotonSuppression` works well, but there are tails for both distributions which means there is room for improvement.

Chapter 5

Properties of Spurious Photons

The focus of this analysis is to study the ways in which spurious photons arise in the ECL and explore the parameter space in how they are distinct from true photons. This information can be used to better discriminate between spurious and true photons at Belle II, thereby improving π^0 reconstruction and signal purity via analysis of residual ECL energy in physics analyses. Simulation studies are a first step in finding detector observables that emerge from secondary processes leading to spurious photons. This section serves as a detailed look at the severity and characteristics of two main sources of spurious photons, hadronic split off (HSO) and low transverse momentum (LPT) clustering, in simulated data.

5.1 Data Samples

Belle II creates huge amounts of simulation data that is regularly shared across the collaboration for design and analysis purposes. Normally, MC matching is used to select the particles/reconstructed objects in which a user is interested, then these particles becomes that user's data set. In theory, MC matching can be done to get a sample of HSO by requiring that the particles are secondaries created by inelastic hadronic scattering or decay from particles created by inelastic hadronic scattering. This information can be accessed after MC matching with the variable `mcSecPhysProc`, which gives a code from the Geant4 simulation about how a particle was created. However, due to the nature of MC matching in the ECL, HSOs are often left unmatched.

Furthermore, ECL clusters from LPT clustering can't be MC matched because only one ECL cluster can be matched to one MC particle. Therefore, most spurious photons end up without an MC match, so this type of data sample is very limited in its ability to study all cases of spurious photons. The most valuable information that can be extracted from these MC samples are how and where the simulated particles are produced and where they end up, but this does not include any information on reconstructed objects. Therefore, the data currently best suited for these studies are simple single particle simulations. This way, any detector signal is known to have come from processes caused by the generated particle which can be repeatedly created in the same way. This is exactly what the `ParticleGun` (see section 4.1) module is made for.

`ParticleGun` can be fed many different parameters to change the way it creates particles. For these studies, unless otherwise stated, particles were produced at a fixed momentum (both direction and magnitude) at the interaction point. The momentum direction was $60°$ in ϕ and $90°$ in θ. The momentum magnitude and type of particle were varied for study. Most often, 5000 events were produced for each momentum and particle type pairing using basf2 `release-06-00-14`. To keep the analysis focused, events where the particle interacted or decayed before reaching the ECL were removed from the sample. This was done by finding events in which the decay vertex of the initial particle was before the ECL radius, then removing these events from the sample. This is the data sample that will be called "single particle events" in the following sections, whether the particle be a muon, pion, or kaon. The parameters which determine if a particle is more or less likely to reach the ECL are the decay time, Lorentz boost, and particle type (hadron or lepton). Muons almost always make it to the ECL, while low momentum kaons are least likely to reach the ECL, which is shown explicitly in figure A.3.

Finally, spurious photon is a catchall term that is worth moving away from in this focused study. Therefore, ECL clusters matched to the track from the initial particle will be referred to as primary clusters, while clusters arising from HSO or LPT clustering will be called secondary clusters.

5.2 Interaction Modes Leading to Hadronic Split Off

It is worth having a qualitative feel for what HSO may look like. To this end, the Belle II event display, a program which yields a rendering of the MC particles and the detector response of an event, was used to view HSO. The simulation was set to save secondary particles over 4 MeV in energy, but, as described in section 4.1, lower energy particles are still simulated to achieve proper detector response. This section describes how to interpret the event display, then showcases event displays of the most common cases of HSO. More event displays can be seen in appendix B.

The Belle II event display shows multiple perspectives of a simulated particle collision, but for simplicity only one perspective (a cross section of the barrel at the IP) is shown in figure 5.1. From this perspective, the vertical axis corresponds to the y-axis and the horizontal corresponds to the x-axis. The scales on the display are given in centimeters. The display showcases the VXD in pink and the TOP in blue to get bearings within the detector. Simulated particles are shown as dashed lines of varying colours as to identify their type. Reconstructed tracks are solid blue lines and ECL clusters show up as red columns just outside the TOP. The height of the column corresponds to the energy of the ECL cluster.

Now that the reader has an understanding of what everything represents, the event display of figure 5.1 may be discussed. There is a reconstructed track coming from the IP, which is the generated 0.6 GeV/c momentum pion. This track is extrapolated to the outer detector region, and straightens out after passing the solenoid, where the magnetic field is no longer apparent. Just after the TOP (i.e. in the ECL) there are 3 dashed yellow lines

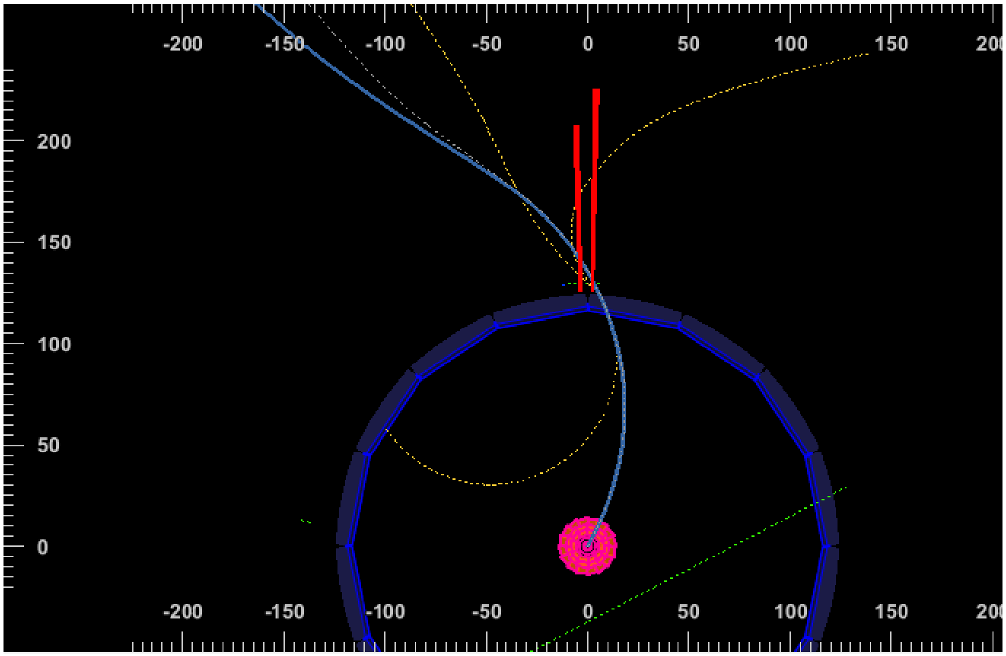

Figure 5.1: Event display of HSO resulting from a 0.6 GeV/c momentum π^-.

which represent protons. These must have come from an inelastic nuclear interaction of the form,

$$\pi^- + N \rightarrow nucleons \tag{5.1}$$

where π^- is the original pion and N is a nucleus. This can be confirmed by looking at the simulation data and is one of the most common nuclear interactions observed for 0.6 GeV/c momentum pions. Here, there are two ECL clusters arising from this pion, likely due to the spread of the hadronic shower[1].

Moving on to higher momenta, the event display in figure 5.2 shows a single 1 GeV/c momentum pion event. Once again, a reconstructed track comes from the IP and is extrapolated to the outer detector, which is the 1 GeV/c momentum pion. A nuclear interaction takes place in the ECL, slightly deeper than in figure 5.1. Various pink, green, and yellow dashed lines, representing neutrons, photons, and protons respectively, come

[1]The z-axis part of the spread can't be seen from this perspective, but does exist.

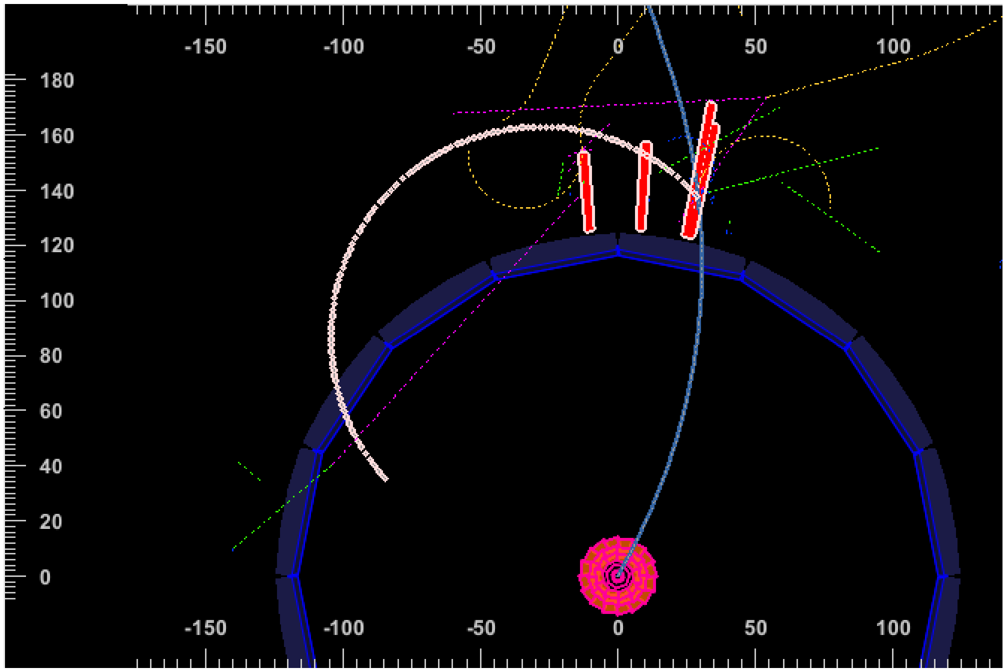

Figure 5.2: Event display of HSO resulting from a 1.0 GeV/c momentum π^-.

from this vertex. The particle highlighted in white is a pion, which comes from a nuclear interaction of the form,

$$\pi^- + N \rightarrow nucleons + \pi^- \tag{5.2}$$

The pion curls in the magnetic field, through the ECL where it leaves ionization and/or eventually suffers another nuclear interaction. This process likely causes the three secondary clusters seen in figure 5.2 (there are 4 clusters in total, but two overlap in this perspective). Pions from nuclear interactions are another common form of HSO. As observed in this event, they have potential to cause split offs far from the primary cluster.

Speaking generally about the differences between the low and high momentum examples discussed above, higher momentum hadrons have a larger phase space to create/free particles in nuclear interactions and can produce higher momentum particles. This becomes clear when comparing more event displays from low and high momentum particles, such as those found in appendix B.

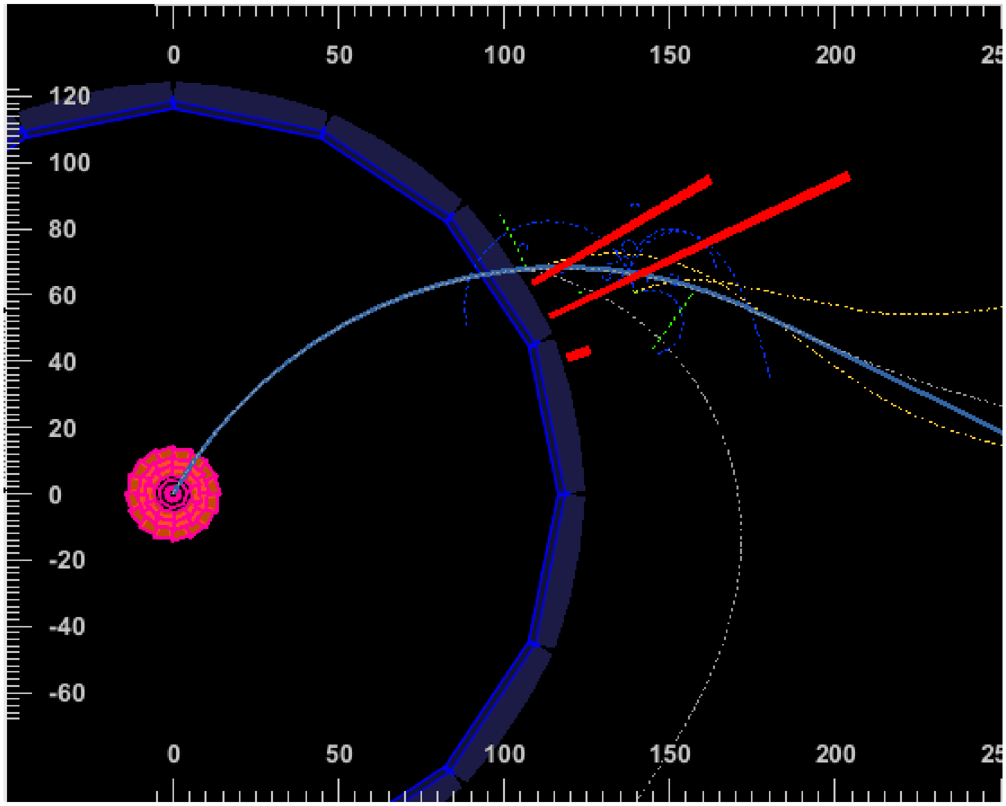

Figure 5.3: Event display of HSO resulting from a 0.6 GeV/c momentum π^+.

Hadronic interaction also depends on particle type. First, simple charge conjugation will be studied with a 0.6 GeV/c (positive) pion event. The event display, as found in figure 5.3, shows similar events to what has been seen before, but this time the curvature of the initial pion is in the opposite direction. Furthermore, many blue dashed lines come from the nuclear interaction. These blue dashed lines are electrons arising from electromagnetic showers caused by photons coming from a neutral pion decay. The neutral pion arises from a nuclear interaction of the form,

$$\pi^+ + N \rightarrow hadrons + \pi^0 \tag{5.3}$$

What is interesting about the neutral pion interaction mode is that much of the energy is deposited from photons, making it harder to discriminate against primary (signal) photons. There is also a pion (the grey dotted line) in figure 5.3 coming from the interaction which is likely responsible for some of the energy deposition leading to (in tandem with photons) the secondary ECL clusters. It should be noted, neutral pions also come from interactions involving negative pions. The main difference between positive and negative pion interactions are the cross sections (seen in figure 2.5).

Particle type plays a larger role when considering kaons. Kaons contain a strange quark, which cannot change flavour in strong interactions. This means there are a host of new particles that can be produced in a hadronic shower from a kaon. Furthermore, the strange quark must eventually decay, which can lead to further interactions and/or high energy particles in a separate part of the detector.

Figures 5.4 and 5.5 show events with an initial 1 GeV/c momentum K^- and 0.6 GeV/c momentum K^+ respectively. The display in figure 5.4 shows the side-on perspective of the event, with the z-axis as the horizontal axis and the y-axis as the vertical one. Overall, this nuclear interaction does not look very different from the previous ones. However, there is a difference in that a Λ^0 (a strange hadron) comes from the interaction, which then travels a short distance before decaying into a proton (dashed yellow line) and pion (dashed grey line). This pion and proton are likely responsible for the ECL cluster left of the primary cluster (in this perspective).

At lower momentum, some strange interactions are forbidden or suppressed. In fact, due to the kaon's large mass and shorter lifetime (see table 2.1), it is far more likely to decay within the detector volume than a pion of the same momentum. This is what is in figure 5.5, and is what happens quite often for lower momentum kaons. In this display, a kaon decays to a muon neutrino and anti-muon, which travels a short distance before decaying to a positron, anti-muon neutrino, and an electron neutrino. This electron (and maybe ionization from the muon) likely results in the secondary ECL cluster below the primary one. Kaons are likely to decay in the ECL because they are close to the low energy rise of the Bethe curve (see figure 2.2). Once having lost some energy to ionization, they are no longer minimum ionizing and will climb the Bethe curve, losing more and more energy until they stop. While they are losing energy, their Lorentz boost becomes

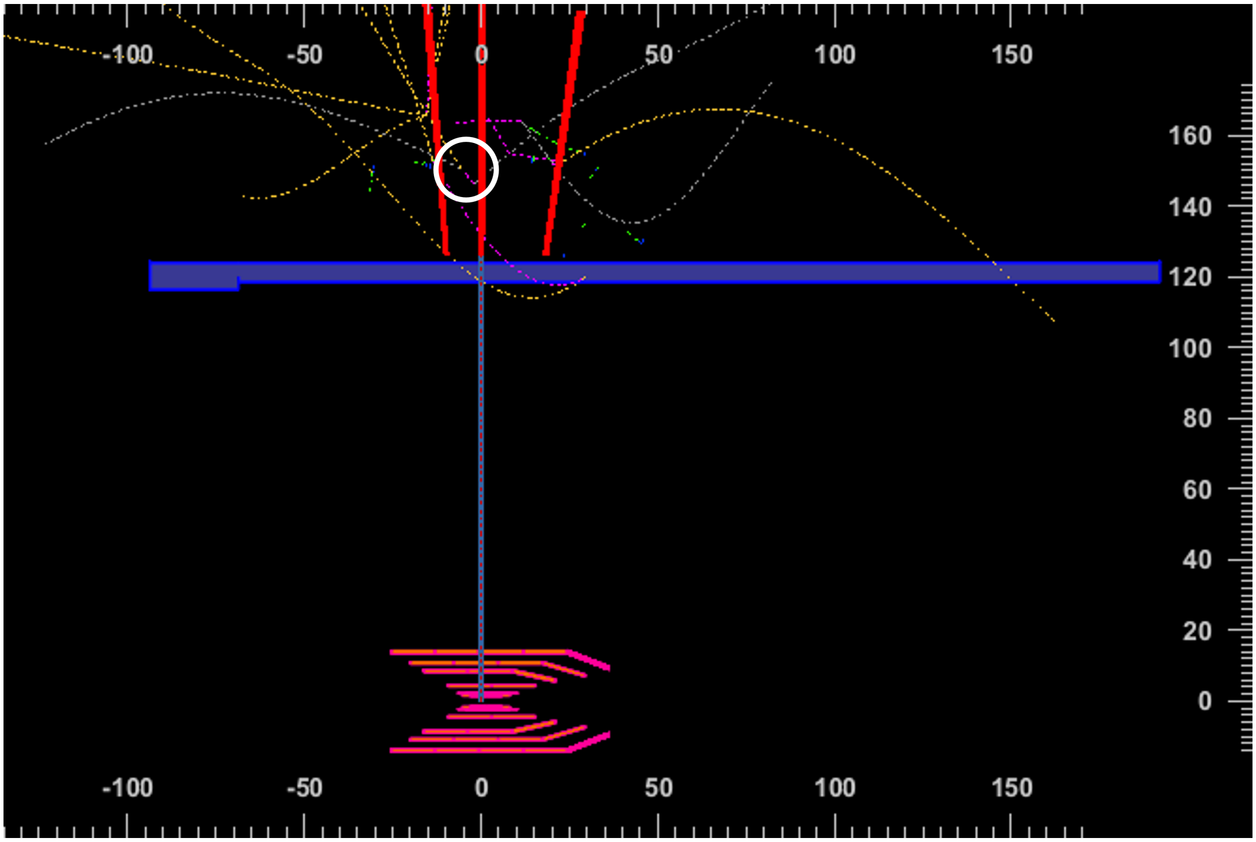

Figure 5.4: Event display of HSO resulting from a 1.0 GeV/c momentum K^-. The nuclear interaction, resultant Λ^0, and its decay to a proton and pion are within the white circle.

smaller and smaller which reduces their time dilation, making the decay all more likely. Therefore, if a low momentum kaon reaches the ECL, it is likely to interact or decay inside the ECL.

The event displays presented above show a qualitative understanding of HSO. There is clear dependence on the momentum and type of incident particle, with interplay between those two properties. The bulk properties of HSO within Belle II will now be studied with a focus on the dependency on momentum and particle type of these interactions. Many of the processes described above will be important to keep in mind when comparing these macroscopic properties, starting with the ECL cluster multiplicity.

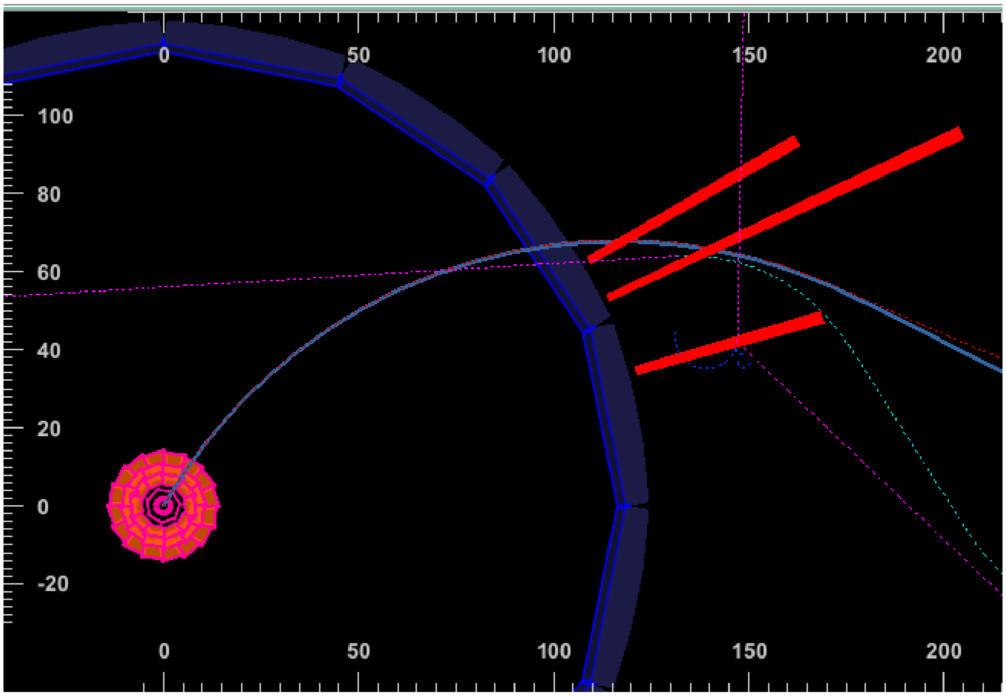

Figure 5.5: Event display of HSO resulting from a 0.6 GeV/c momentum K^+.

5.3 Cluster Multiplicity

As described in section 4.4, high cluster multiplicity leads to problems in physics analyses. Therefore, ECL cluster multiplicity may be used as an initial measure of the impact LPT clustering and HSO has on an analysis. Since these effects are mixed for (low transverse momentum) charged hadrons, it is useful to analyse single muon events to isolate the frequency and characteristics of LPT clustering. Figure 5.6 shows the number of ECL clusters seen in single muons events (the data set defined in section 5.1) as produced by the particle gun setup described in section 5.1. It is clear that cluster multiplicity from LPT clustering increases as transverse momentum decreases. These data also show a dramatic transition in multiplicity between particles with transverse momentum of 0.4 GeV/c and 0.6 GeV/c, where the number of single clusters seen from muons drops by a factor of 7 in place of higher multiplicities. At transverse momenta above 0.8 GeV/c, LPT clustering is insignificant, so the approximate cutoff for LPT clustering can be established at 0.8 GeV/c. Of course, below the 0.3 GeV/c threshold no ECL clusters should be present unless the

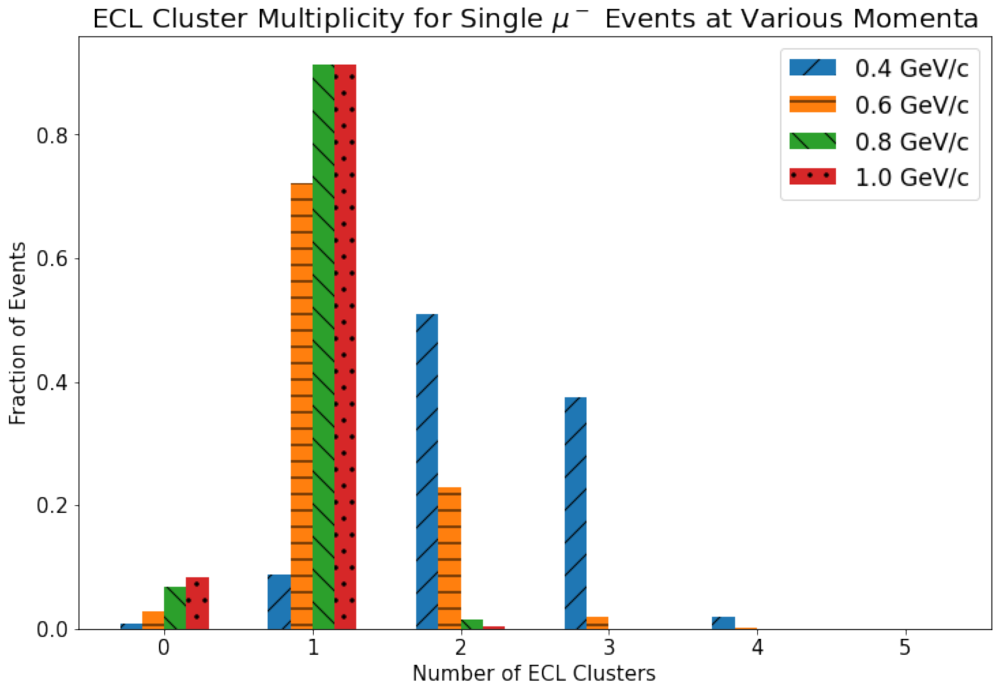

Figure 5.6: ECL multiplicity for simulated single muon events at various momenta. Equivalent to multiplicity due to LPT clustering. The momentum for each distribution can be found in the legend.

initial particle decays in the CDC, in which case the daughter could make its way into the ECL. Though this thesis is focused on hadrons, this shows that muons with a particular transverse momentum can be troublesome as well.

Moving to charged hadrons becomes tricky. Hadronic interactions may occur soon after the hadron enters the ECL, before it leaves the long trail of ionization that causes LPT clustering. Furthermore, hadrons can catastrophically interact in the inner detector region and have shorter decay times than muons, which means fewer hadrons reach the ECL and will be removed from the data sample. Therefore, one cannot simply subtract the multiplicity seen from muons (LPT clustering) from the hadron multiplicity to get the multiplicity from HSO. The strongest conclusion is that LPT clustering becomes insignificant at and above momenta of 0.8 GeV/c.

The multiplicities for negative pions can be seen in figure 5.7. The multiplicity is highest at low momenta, as suspected from what was seen with muons. However, the ECL

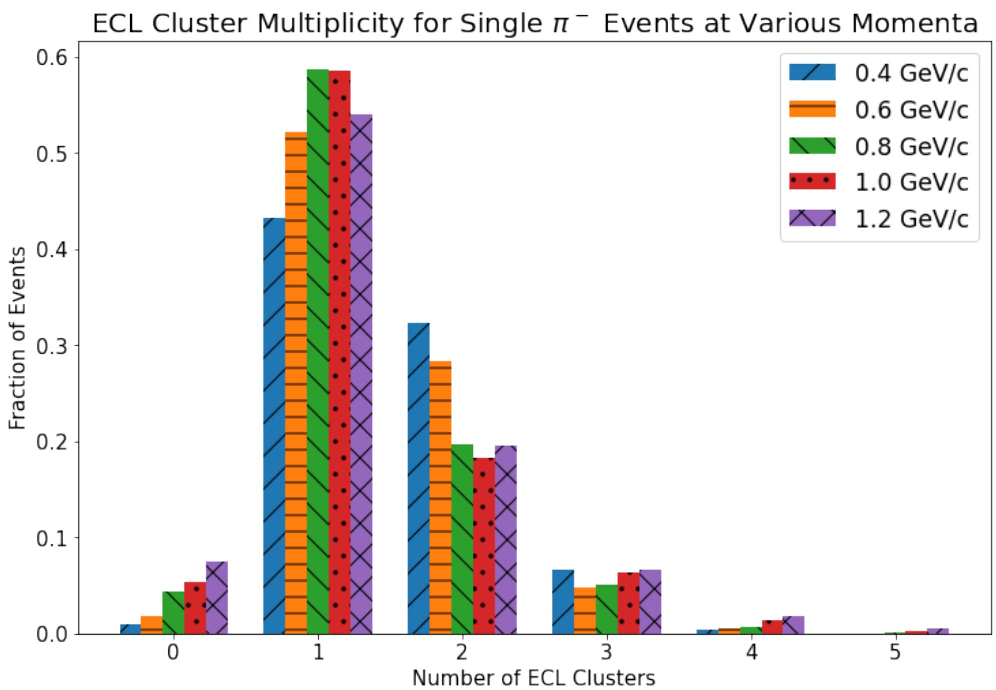

Figure 5.7: ECL multiplicity for simulated single pion events at various momenta. The momentum for each distribution can be found in the legend.

multiplicity for pions at low momenta is actually lower than that of muons. This is likely due to pions slowing (lowering their Lorentz boost) and decaying within a more localized region of the ECL, where muons would simply continue without decaying. At higher momenta, HSO causes a significant increase (when compared to muons) in ECL multiplicity at and above 0.8 GeV/c momentum. Furthermore, the frequency of high multiplicities (greater than 3 ECL clusters) monotonically increase with particle momentum, with the exception of a peak in 3 ECL clusters for pions with 0.4 GeV/c momentum. This is likely due to the larger and more chaotic interactions possible at higher energies. ECL multiplicity for negative pions is slightly higher when compared to positive pions (see figure A.2), as expected due to the lower cross sections seen in figure 2.5.

This is all to show that, for pions, HSO occurs $\sim \frac{1}{3}$ of the time at momenta above 0.8 GeV/c and a mix of HSO and LPT clustering occurs $\sim \frac{1}{2}$ of the time for momenta 0.6 GeV/c and below.

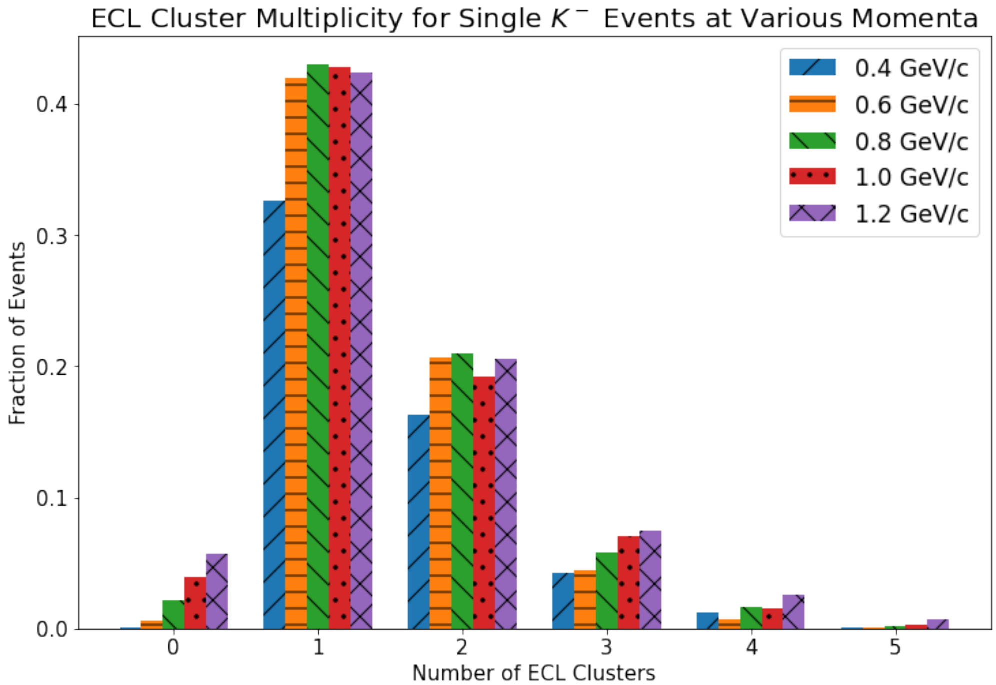

Figure 5.8: ECL multiplicity for simulated single negative kaon events at various momenta. The momentum for each distribution can be found in the legend.

ECL multiplicities for kaons, seen in figure 5.8, are comparable to those of pions at first glance. The main difference is in the fact that kaons decay before the ECL more than twice as often as pions, which significantly reduces the sample size, particularly at low momenta. This explains the minimums at 0.4 GeV/c seen in 2 and 3 ECL clusters while these are maximums for pions. The other difference is that, even with extra decays before the ECL, the HSO multiplicities (multiplicities for momenta 0.8 GeV/c and above) are the same. This implies that kaons, if they reach the ECL, are more likely to produce secondary ECL clusters than pions.

Something apparent in each of the multiplicity figures shown above is a monotonic increase with momentum in the rate of finding no ECL clusters. This should only happen when a muon doesn't leave enough ionization in a single crystal for it to be a seed crystal for clusterization (10 MeV). One instance where this could happen is if the muon slips through the interface of two crystal, although this is incredibly rare and wouldn't account for the level of zero ECL multiplicity seen in figure 5.6. This is an effect that should be studied further.

The dominant processes through which charged hadrons create secondary clusters is HSO and LPT clustering. Multiplicity plots show HSO increases with momentum while low-transverse momentum clustering is important at transverse momenta below 0.8 GeV/c, but becomes insignificant[2] above 0.8 GeV/c. It is clear that there are enough of these secondary clusters created such that it is important to remove them from analyses. To do so, the first step is to analyze the underlying properties of the secondary clusters based on pre-existing variables in the Belle II analysis software framework.

5.4 Relevant Detector Variables

Secondary clusters from HSO or LPT clustering should have different characteristics from those of photons. These distinct characteristics give a way to discriminate secondary clusters from real photons and primary ones. These variables (introduced at the end of section 4.4) have already been studied for spurious photons and applied in the `fakePhotonSuppression` variable, but have not been studied separately for HSOs and LPT clustering. This section studies the differences in ECL cluster variables for these two processes. Namely, the variables `minC2TDist`, `clusterE`, `clusterZernikeMVA`, and `pulseShapeDiscriminationMVA` will be studied through simulated single particle events. The two other variables used in `fakePhotonSuppression`, `clusterTheta` and `clusterTiming`, can't be studied in meaningful ways given the simulation setup. First, variables for secondary ECL clusters from muons and pions will be analyzed and compared, then notable differences in secondary clusters from kaons and pions will be analyzed.

[2]According to the simulated single particle events. Trails of ionization can be longer when the momentum is not in the θ=90 direction. In theory this would increase the frequency of LPT clustering, but should be studied further.

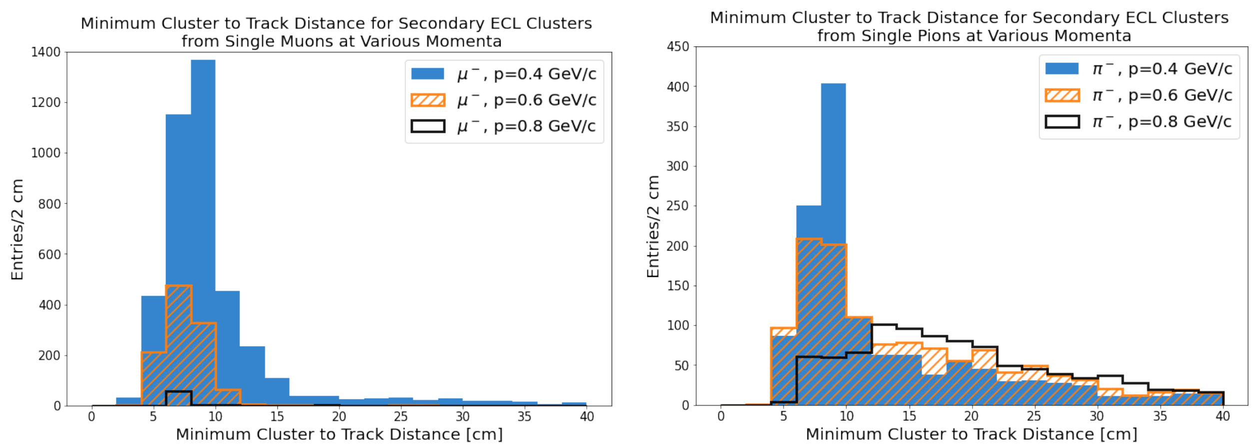

(a) **(b)**

Figure 5.9: Minimum cluster to track distance of secondary clusters from muons (a) and pions (b) at momenta 0.4, 0.6, and 0.8 GeV/c. Note the difference in vertical axes.

First, `minC2TDist`, or the minimum distance between the selected cluster and where a track meets the ECL shall be studied. Intuitively, one can expect a difference between this variable for true photons and HSO or LPT clustering, since the latter two occur via charged particles that leave tracks in the CDC. Figure 5.9a shows the distribution of this variable for muons, which can be interpreted as the distribution for LPT clustering. Here it can be seen that the mean minimum distance to a track decreases as transverse momentum increases. However, when compared to the same distributions for pions, in figure 5.9b, it is much more likely for secondary clusters from pions to be produced > 15 cm from the track, especially when considering the 0.8 GeV/c momentum distributions. Since LPT clustering rarely occurs at this momentum, this is a direct result of HSO. This is to say that secondary clusters from HSO are often further from their primary cluster or track than those from LPT clustering. At higher and higher momentum, this distancing increases slightly as seen in figure C.1 of appendix C.

However, when moving to a realistic setting, like an $\Upsilon(4S)$ event, the number of tracks increases. The secondary clusters that have a large cluster to track distance in the single particle events will end up with smaller distances since they will be closer to those other tracks. This means they will end up looking more like photons and be harder to discriminate.

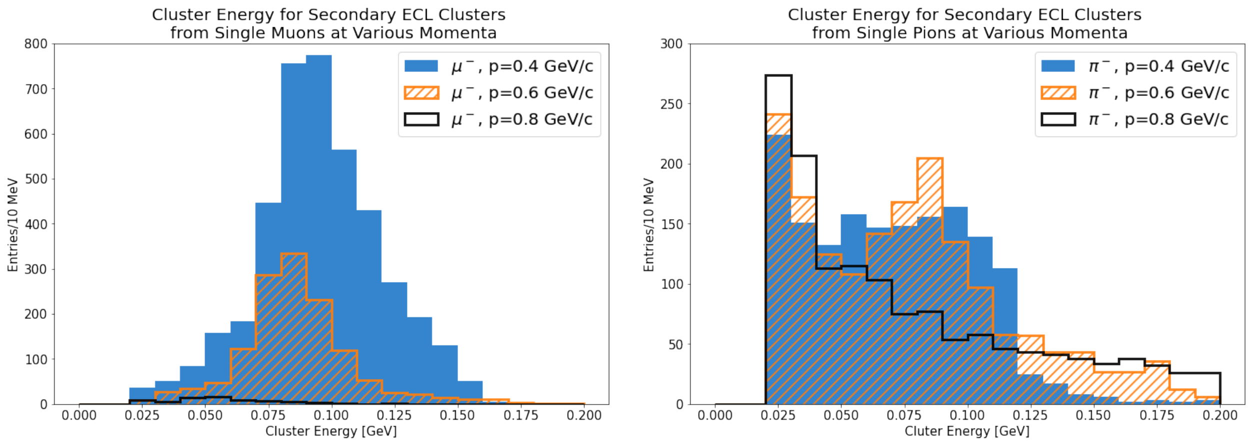

(a) **(b)**

Figure 5.10: Cluster energy of secondary clusters from muons (a) and pions (b) at momenta of 0.4, 0.6, and 0.8 GeV/c. Note the difference in vertical axes.

Another variable expected to be different from true photons is the cluster energy. Photons arising from B meson decay chains will often be of higher energy than those produced by HSO and LPT clustering. Figures 5.10a and 5.10b show the cluster energies for muons and pions respectively. As transverse momentum increases, the cluster energy in low-transverse momentum clusters drops. This can be rationalized through the shorter paths of ionization through the ECL at higher transverse momenta. A rough estimate using PDG values for CsI [7] of the ionization left by a MIP passing straight through an ECL crystal is below:

$$
\begin{aligned}
E_{dep} &= \left(\frac{dE}{dx}\right)_{MIP} \rho \Delta x \\
&= (1.24\text{MeV g}^{-1}\text{cm}^2)(4.51\text{g cm}^{-3})(30\text{cm}) \\
&= 168\text{MeV}
\end{aligned}
\tag{5.4}
$$

And when a MIP enters at an angle of 45^o, that value can be multiplied by $\sqrt{2}$, assuming the transverse path length is equal to the longitudinal one[3], to yield 237 MeV, an increase of 69 MeV. Clearly, figure 5.10 shows cluster energies are most often smaller than those calculated above, but that is because they are split between the primary and secondary ones.

Comparing the pions and muons, thereby extracting the behaviour of HSO, the energy shifts to favour low energy clusters for pions, but there also exists a longer tail. The length of the tail increase at higher momentum as can be seen in figure C.2. The LPT peak is maintained until 0.6 GeV/c. Based on these plots, if a secondary cluster has an energy below 50 MeV or above 150 MeV, it can be expected to have come from HSO rather than LPT.

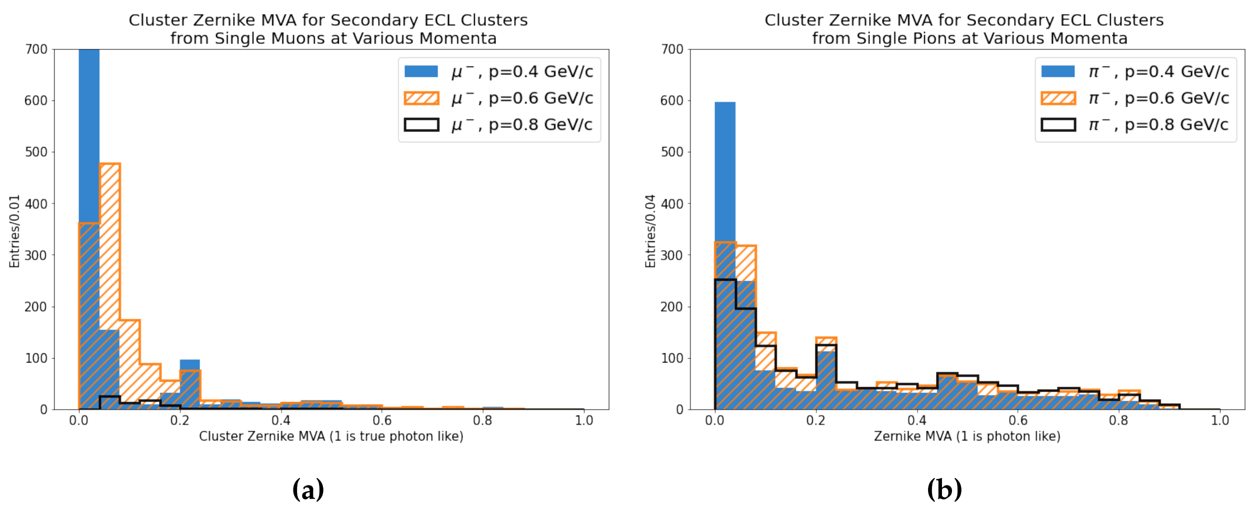

Figure 5.11: Zernike MVA of secondary clusters from muons (a) and pions (b) at momenta of 0.4, 0.6, and 0.8 GeV/c. Note that the first bin in (a) has a value of nearly 4000 for 0.4 GeV/c muons, but has been cut off to better show other details.

Another characteristic that distinguishes photon showers from others is the shower shape. This can be quantified via Zernike polynomials [46]. Belle II has a built in MVA that computes the Zernike polynimials of ECL clusters and outputs a classifier, called `clusterZernikeMVA` [44]. This classifier output can be seen in figure 5.11 for secondary

[3]The transverse length would be larger due to slowing and curling within the magnetic field.

ECL clusters from muons and pions. In classifying clusters as photon-like from other types of clusters, the classifier can be thought to measure the symmetry of a cluster, but some features in the distribution are not well understood. Nonetheless, this variable arguably has the strongest dependence on momentum for the muon case in comparison to other variables in this section. The lower momentum muons almost always have an output of < 0.05 while the peak of 0.6 GeV/c momentum muons is above this. An explanation for this lies in the angle at which particles of different momenta hit the ECL. The lower the momentum, a cluster is likely to see a track that is more parallel with the face of the ECL crystals, rather than perpendicular to them like photons should be. This greatly changes the shape of the ECL cluster. When comparing pions to muons, the distribution gains a large tail up to just around 0.9. This tail also occurs for secondaries from 0.6 GeV/c momentum muons, but is much smaller in magnitude.

Lastly, the pulse shape discrimination MVA can be analyzed for the secondaries in the data sample. The distributions for this variable for secondary clusters from particles of various momenta and particle types, as seen in figure 5.12, are quite similar except for multiplicity effects (impacting the total number of secondary clusters). The differences are best viewed when the distributions are normalized (see figures C.3 and C.4). There is a slight increase in the peaks at 0 for 0.6 GeV/c and 0.8 GeV/c momentum pions, though these peaks are surpassed by the 0.6 GeV/c muons. This is likely because pulse shape discrimination works better at higher momenta/energies. While this variable shows little difference between HSO and LPT clustering, it is a strong discriminator between spurious photons and true photons since pulse shape differs in CsI for these processes. Therefore it remains valuable for discriminatory purposes [42].

The variables `clusterTheta` and `clusterTiming` have been omitted from a detailed analysis here because the particle gun simulation is not suitable to study them. The polar angle of the cluster, `clusterTheta`, is important for the difference in distributions between photons and charged particles coming from B meson decay chains, but in particle gun the direction at which the particle comes from the IP is fixed. To better analyze the

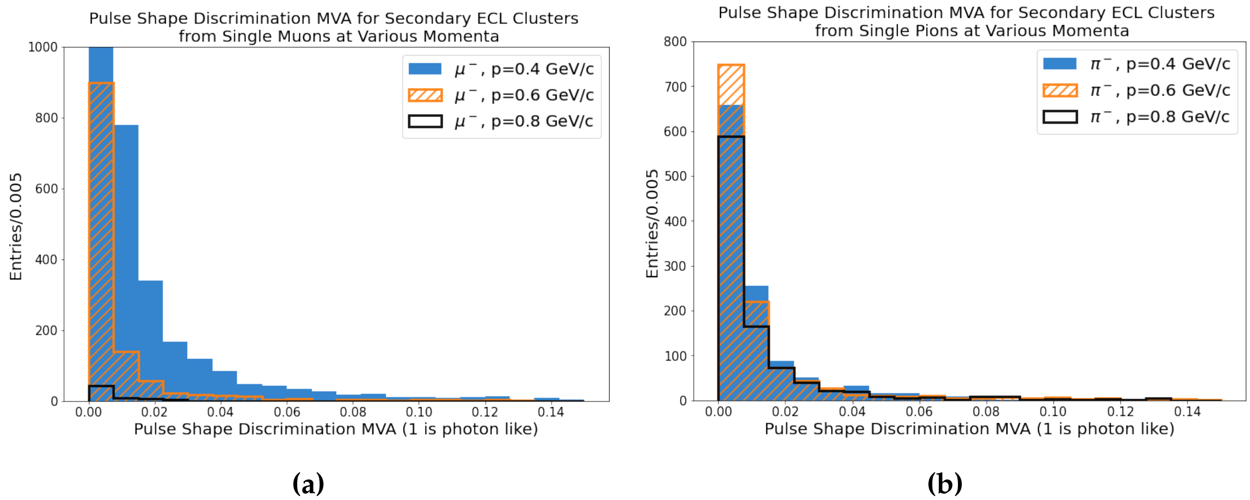

Figure 5.12: Pulse shape discrimination MVA of secondary clusters from muons (a) and pions (b) at momenta of 0.4, 0.6, and 0.8 GeV/c. Note that the first bin in (a) has a value of just over 2000 for 0.4 GeV/c muons, but has been cut off to better show other details.

difference between the theta positions of LPT clustering and HSO, this analysis can be repeated, generating each single particle event with the characteristic angular distribution of charged particles seen in $\Upsilon(4S)$ events. The timing of the cluster (after the collision causing an event), `clusterTiming`, depends on the determination of the initial time of an event. This quantity is improperly calculated for particle gun simulations since it is altered by track and ECL cluster multiplicity. Therefore, the distributions for the cluster timing will be different for real events since they have significantly different multiplicities for these two reconstruction objects. Fully simulated $\Upsilon(4S)$ events would improve the measure of cluster timing for LPT clustering and HSO. This can be cross-checked with experimental data. In data, one could get a high purity list of pions by reconstructing short lived kaons since they decay to a π^+ and π^- 69% of the time [7]. The area around these pions can then be checked for ECL clusters which are likely LPT clusters or HSOs (though by choosing clusters close to the pions, the sample becomes biased).

Figures 5.9, 5.10, and 5.11 show that, while secondary clusters can be distinguished from photons, they can also be separated by the process in which they are formed because of their different ECL cluster properties. However, the process of kaon stopping, observed in section 5.2, hasn't been studied in the plots above. This process is only observable for low momentum kaons and is most interesting when compared to pions since they are both hadrons. Figure 5.13 shows distributions of ECL cluster variables with stark differences, implying these secondary clusters have significant dependence on the type of particle that causes them.

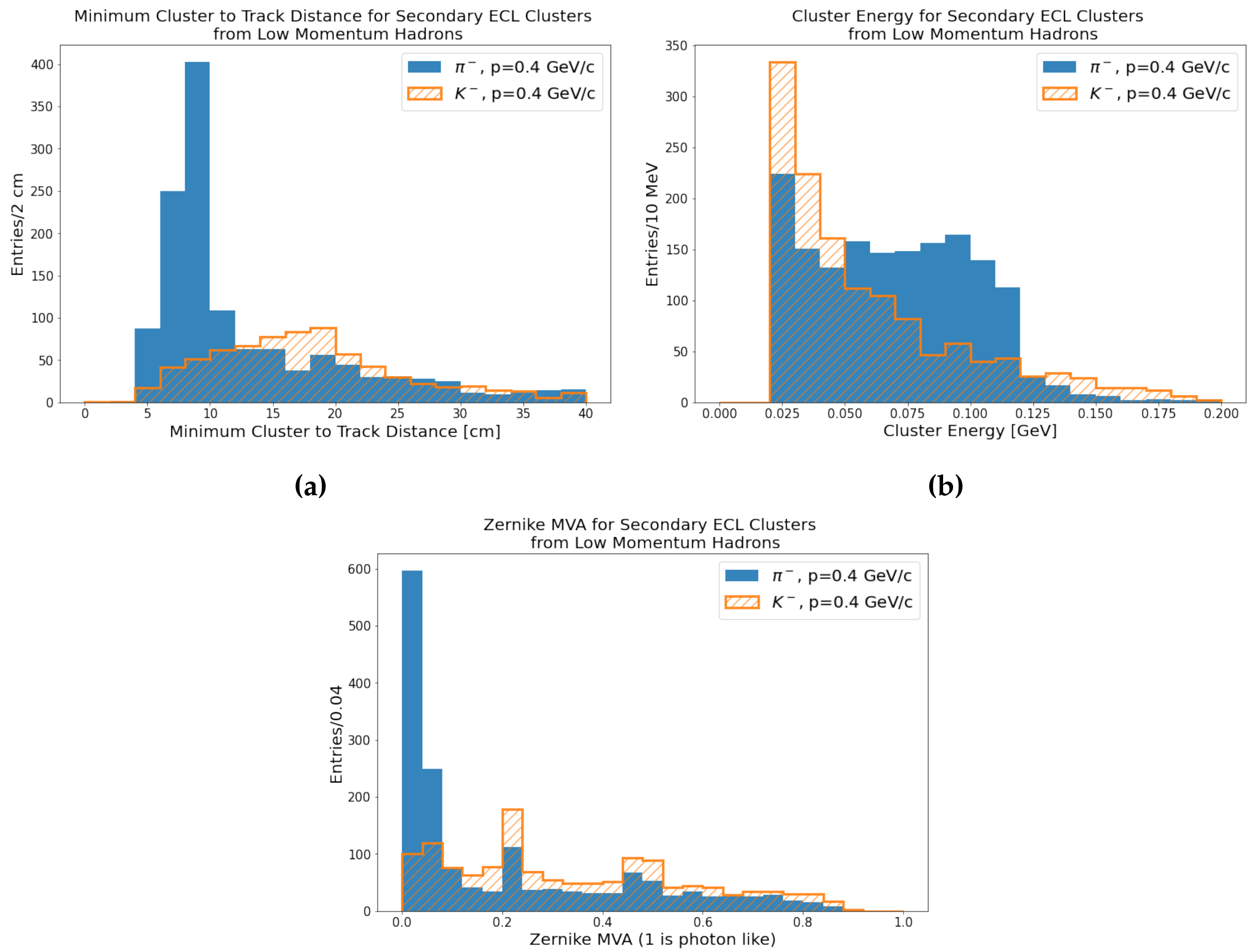

(a) **(b)** **(c)**

Figure 5.13: Distributions for the minimum cluster to tracks distance (a), cluster energy (b), and the Zernike MVA (c) for secondary ECL clusters from low momenutm (0.4 GeV/c) kaons and pions.

Overall, secondaries from low momentum kaons are further from the track that causes them, lower in energy, and have shower shapes that are more likely to resemble those of photons. This points to a significant reduction in LPT clustering. The most sensible cause of this reduction is that low momentum kaons are decaying in the ECL before they would leave long tracks of ionization, which can be observed in simulation using the event display as done in figure B.10.

Analysis of secondary clusters from various particles has shown that their properties, specifically some of the variables used in `fakePhotonSuppression`, have a strong dependence on the momentum and particle type of the final state particle that causes them.

Chapter 6

Spurious Photon Discrimination

Having studied the underlying properties of LPT clustering and HSO clusters, the current methods of their discrimination can be analyzed and understood. Notably, the current method of discriminating these clusters, the `fakePhotonSuppression` MVA (discussed in section 4.4), only looked at the bulk properties of the variables discussed in the previous chapter without extensive consideration for the underlying ways in which these types of spurious photons arise. Analysis of the faults in the current method of discrimination may inform as to where and how improvements can be made.

This chapter will first give an overview on the performance of current spurious photon discrimination methods and then give evidence that there is further information to be exploited for the purpose of discriminating spurious photons.

6.1 Spurious Photon Discrimination Performance

The variables described in the previous chapter are all inputs to the `fakePhotonSuppression` MVA described at the end of section 4.4. It is worth testing the performance of this MVA on the simulated single particle events. However, it is important to keep in mind that the variables for the timing of the cluster and the theta position of the cluster aren't fairly represented in these data. Histograms of the output of

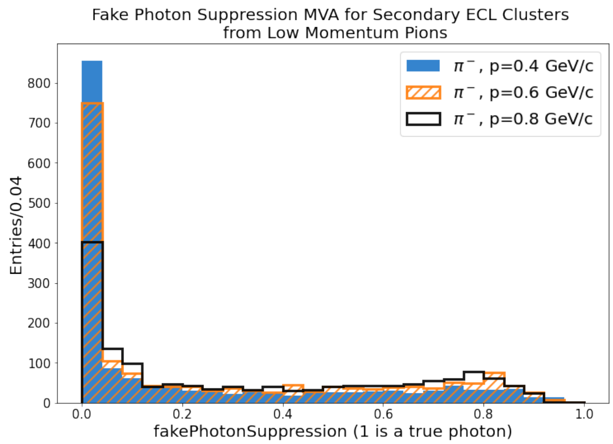

(a)

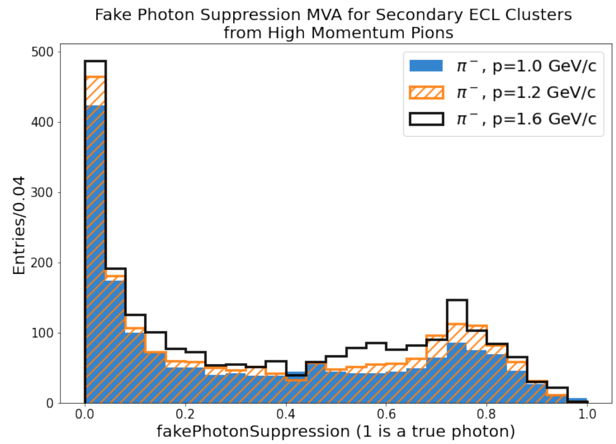

(b)

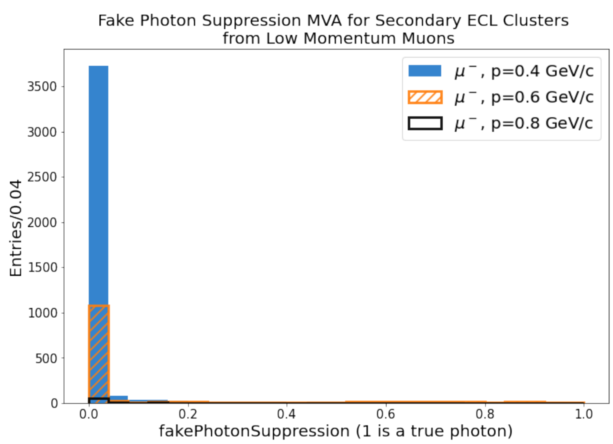

(c)

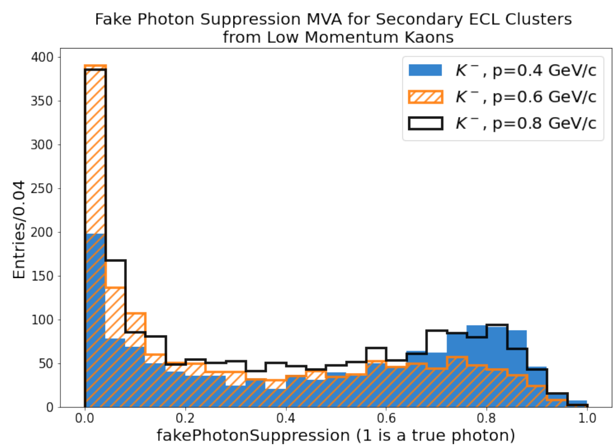

(d)

Figure 6.1: Distributions of the current spurious photon MVA for (a) low momentum pions, (b) high momentum pions, (c) low momentum muons, and (d) low momentum kaons.

the `fakePhotonSuppression` variable for various particle types and momenta can be seen in figure 6.1.

The performance of this MVA on LPT clustering from muons is remarkably good. Essentially all secondary clusters in this case were categorized as spurious photons. On the other hand, mis-classifications arise when looking at charged hadrons, implying HSO is the cause of the problems facing this MVA. In particular, this MVA performs worse on kaons and high momentum hadrons as seen in the thicker tails and peaks around 0.8 in figures 6.1b and 6.1d.

There are multiple reasons as to why the performance of the `fakePhotonSuppression` MVA is great for low trasverse momentum clustering and not so great for HSOs. The first one, and most obvious, is that HSOs simply mimic photons better than LPT clustering. When looking at the distributions for `minC2TDist` (figure 5.9), `clusterE` (figure 5.10), and `clusterZernikeMVA` (figure 5.11) the pions always have a larger range of values that are often more similar to those of photons. Furthermore, when considering the hadronic interactions that lead to HSO, sometimes photons are truly created when neutral pions are in the interaction, and sometimes particles travel to the opposite side of the detector which make them extremely hard to associate to the primary particle.

However, the other reason why HSOs aren't discriminated as well has to do with the data and variables with which the MVA is trained. In general, cluster multiplicities are highest when there is LPT clustering. Furthermore, most particles in $\Upsilon(4S)$ events have less than 0.8 GeV/c transverse momentum, which is where LPT clustering occurs (see figure 4.2). Therefore, data (specifically the training dataset) are dominated by LPT clustering, and cannot determine a priori if an ECL cluster comes from HSO or LPT clustering. This means that when the FastBDT model is being trained on the data, it will optimize to discriminate more LPT clusters even if it means mis-classifying the fewer HSO clusters. If there were some node within the trees of the BDT that could determine if the photon candidate is more likely to have come from LPT clustering or HSO, the subsequent nodes may have a better opportunity to classify the cluster correctly. One way this may be done is by considering the (transverse) momentum and the particle type of the nearest track to the ECL cluster in question.

6.2 Secondary Cluster Directionality

One of the main discriminators for spurious photons is the distance of the spurious photon cluster from the nearest point a track hits the ECL [42] (see figures 5.9 and 5.13a).

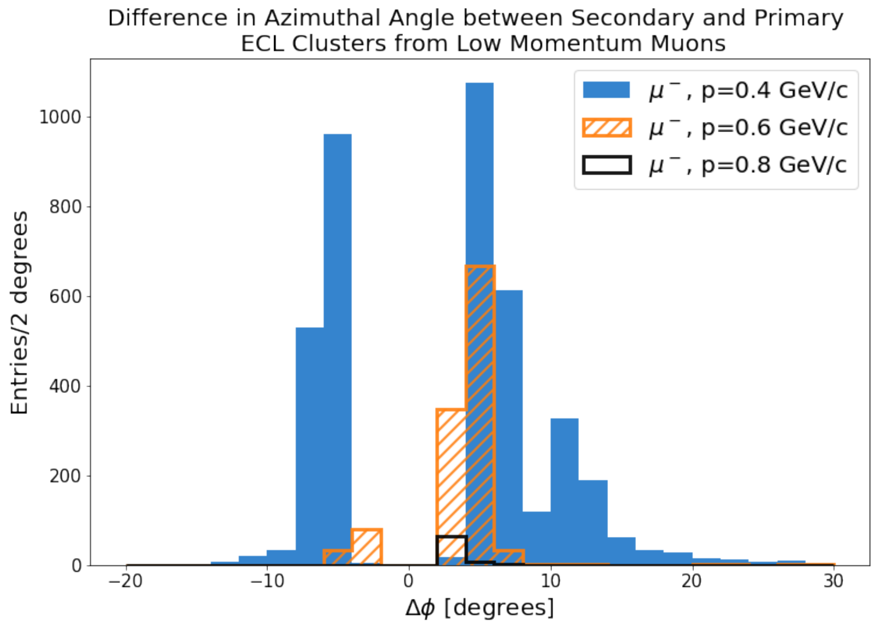

Figure 6.2: Distribution of differences in azimuthal angle for primary and secondary clusters from muons of various momenta.

However, this parameter ignores that for LPT clustering, the clusters should be aligned to the path of the particle through the ECL, and that for HSO the hadronic shower tends to be boosted in the direction at which the particle hits the ECL. In other words, there should not just be proximity relationship between secondary ECL clusters and the tracks of the particles that cause them, but a directional relationship as well. This hypothesis can be tested in the single particle events by comparing the azimuthal angles of the secondary ECL clusters to the primary one.

Figure 6.2 shows the distribution of difference between the secondary and primary cluster azimuthal angles, $\Delta\phi = \phi_{secondary} - \phi_{primary}$, for single muon events at various momenta. Since the muons are negatively charged, they curl in the direction of increasing azimuthal angle (counter-clockwise). The distributions show that secondary clusters can form behind and in front of the primary clusters, but that for transverse momenta 0.6 GeV/c and above, they are preferentially formed in front of the primary cluster. Notably, this differs from bremmstrahlung clusters since those are expected to always be behind the primary cluster (in the azimuth).

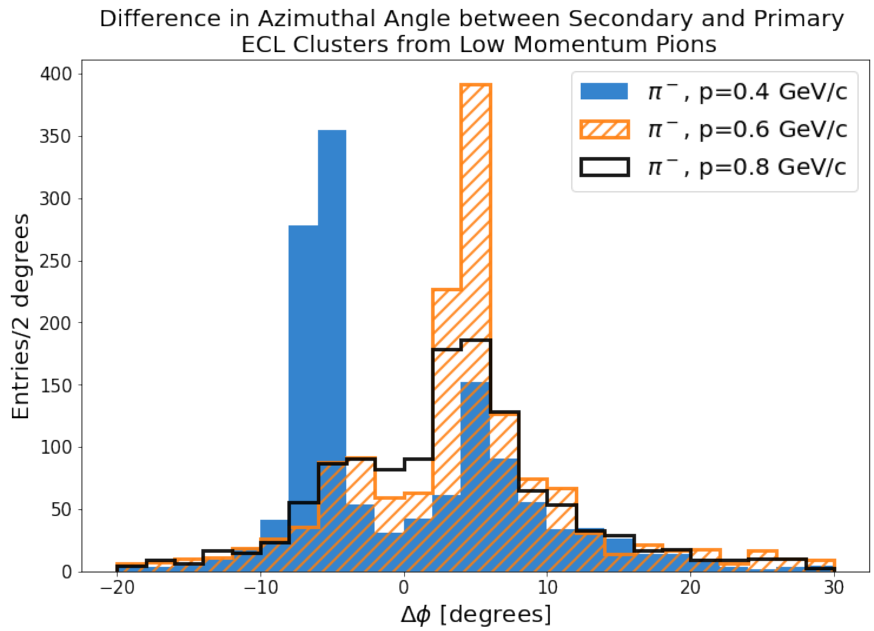

Figure 6.3: Distribution of differences in azimuthal angle for primary and secondary clusters from pions of various momenta.

The same can be seen in figure 6.3 for single pion events, but now with more clusters closer to $\Delta\phi = 0$ and broader distributions as momentum increases. This shows that LPT clustering most often forms clusters between 4 and 8 degrees before or after the primary cluster, whereas HSO has a broader distribution from 8 degrees behind, to 12 degrees in front. There is also a second peak at 10-12 degrees in front for muons at 0.4 GeV/c which likely arises from the muon decaying to an electron. For pairings of true photon clusters and track-matched clusters, we would not see such a directionality nor proximity since these clusters should be independent. This is to say the angular difference would be a useful discriminator for HSO and LPT clustering from true photons.

Improvements may continue by adding the same information in the polar angle. However, it is important to note that the single particles start at θ = 90, and therefore a symmetric distribution about $\Delta\theta = 0$ is expected. Figure 6.4 shows that LPT clustering from muons yields a tight distribution mostly contained within 3 degrees of the primary cluster. When considering pions this distribution broadens from the HSO component as can be seen in figure 6.5.

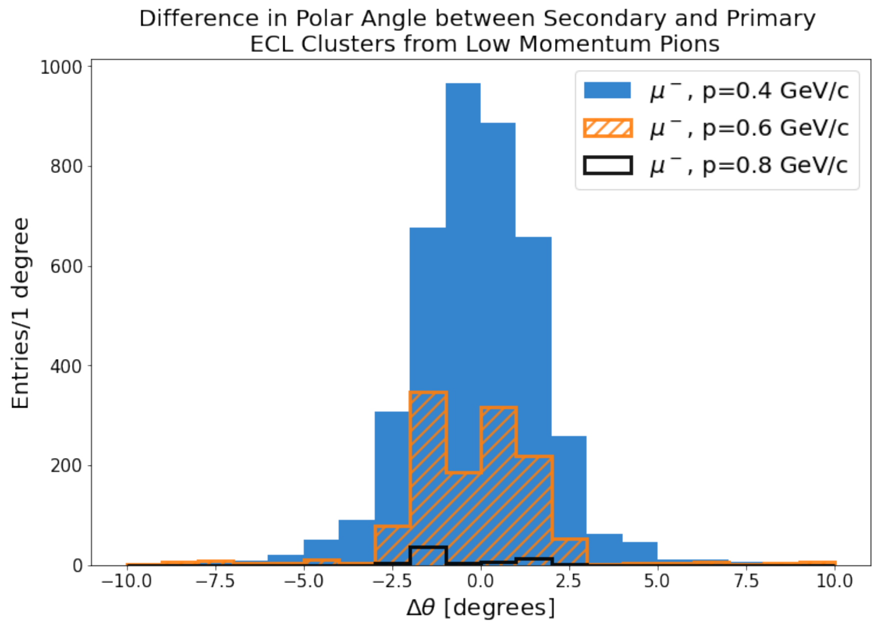

Figure 6.4: Distribution of differences in polar angle for primary and secondary clusters from muons of various momenta.

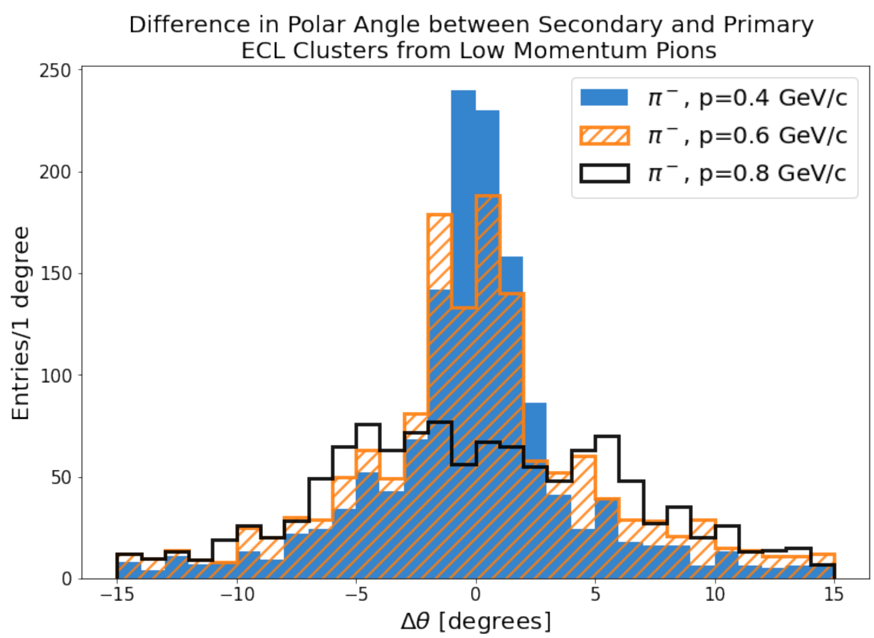

Figure 6.5: Distribution of differences in polar angle for primary and secondary clusters from pions of various momenta.

Together with the azimuthal information, a region that is in the direction of bending due to the solenoidal magnetic can be found in which secondary clusters are localized. This relationship is strongest for low-transverse momentum clustering and becomes weaker for HSO from high momentum hadrons. In any case, differences between secondary cluster and incident track angular positions in both the azimuthal and polar angles is a discriminator for spurious photons. Furthermore, it is a better discriminator than an absolute distance to the nearest track, which is currently being used.

Chapter 7

Discussion

Chapter 5 and 6 analyzed and discussed characteristics of HSO and LPT clustering, common sources of spurious photons, as well as the ways in which they can be discriminated from real photons. This chapter will present a summary of these processes as well as recommendations that will lead to better discrimination of spurious photons caused by them.

The two main sources of spurious photons studied here are LPT clustering and HSO, as was observed in the multiplicity plots in figures 5.6, 5.7, 5.8. Another source that was studied are low momentum particles, especially kaons, which slow and decay within the ECL, causing spurious photons. The ECL variables that have been found and used to discriminate LPT clustering and HSO were analyzed and rationalized in section 5.4. This yielded insight on the motivation to use these variables as discriminators and also showed how they vary with momentum and particle type, detailing their variance with the processes that causes them.

It was observed that the current method of discriminating these spurious photons, the `fakePhotonSuppression` MVA, was exceedingly good at discriminating spurious photons originating from muons (see figure 6.1c), indicating it does well discriminating LPT clustering. With the addition of directional information (discussed below) of these clusters, further improvements are possible. However, improvements to the MVA should be focused on discriminating HSO since this is where the current MVA fails most often. Especially HSO from kaons and particles that have higher momenta (> 1 GeV), since these are more likely to produce π^0s in their hadronic shower. Alternatively, multiple MVAs could be trained for each process.

One way to improve the current MVA is to introduce more information that separates or "clusterizes" the data fed into the FastBDT model. Ultimately, decision trees sort data to certain hypotheses based on multiple boolean decisions. If the decision tree knew early on that the cluster was caused by HSO or LPT clustering, then each branch coming from that node could be tuned to their respective process. Two variables that are immediately available in basf2 and could theoretically yield this information are the momentum of the nearest track and the particle ID of the nearest track.

While these variables seem like they should be useful, it is less clear if they will improve a boosted decision trees model or if the model can already figure out if the spurious photon cluster comes from a certain process. However, principal component analysis [47] could indicate whether or not an additional variable would be useful. Therefore it is recommended to perform a principal component analysis with the current variables included in the `fakePhotonSuppression` MVA as well as the momentum and particle identification of the nearest track.

As discussed in 6.2, improvements could be made upon the proximity relationship between HSO and LPT clustering clusters and the tracks of the particles that cause them by adding an extra dimension. Rather than using the absolute distance between the cluster and the nearest track, one could compare the distance in the direction of the track. For LPT clustering, the clusters will appear just in front or just behind (depending on the particle momentum) the track-matched cluster. For HSO, clusters mostly appear in front, possibly further than those for LPT clustering, and with a wider distribution transverse to the track. This information should, in theory, isolate HSO and LPT clustering more. This would require some prepossessing before one could add this as a variable to the fake photon MVA. Therefore, it is recommended that a variable be added to basf2 that compares the direction of the nearest track as it enters the ECL to the direction of a photon candidate to the cluster matched to the nearest track.

One downfall to using track information to discriminate these clusters is that the nearest track may not actually be the track that caused a spurious photon cluster. To account for this, it may be helpful to assign LPT clustering and HSO regions in the ECL on an event-by-event basis, based on the various tracks' trajectories into the ECL. This type of algorithm would likely be done using some form of machine learning, such as a GAN [48]. From these regions, an LPT cluster or HSO "locality score" can be assigned to each ECL cluster and included in an MVA.

While valuable information has been found during the work of this thesis, there is much left to be studied and characterized regarding HSO and LPT clustering. Spurious photons arising from electrons and neutral hadrons were not studied during the work of this thesis due to their relatively low abundance and unique interactions, though studies on these particles should be considered in the future. Also, these studies should be extended to better measure the cluster timing, which cannot be calculated correctly for simulations using `ParticleGun` and to cover all values of θ, in particular the end caps of the detector. Lastly, cases where particles decay or interact (with the VXD or beampipe) before the ECL should be studied using CDC data.

It is notable that the conclusions presented above come from detailed analysis of HSO and LPT clustering, which is presented in this thesis as the first of its kind. The current `fakePhotonSuppression` algorithm was developed based on bulk properties of data samples thought to correspond to these types of spurious photons, but did not consider in detail the properties of the processes causing them.

Finally, these findings must be verified and checked in data. An example of a data sample that will be useful to check are displaced vertices of two oppositely charged particles, which would yield a pure $K_s \to \pi^-\pi^+$ sample. The photons in the event, in particular around the pions, could be compared to those seen in simulation.

Chapter 8

Conclusion

This thesis presented a characterization of hadronic split off (HSO) and low transverse momentum (LPT) clustering, a subset of spurious photons in the Belle II experiment. HSO and LPT clustering were found to be large sources of spurious photons and each was found to have unique characteristics. A series of recommendations was made to further explore these spurious photons and improve their discrimination based on the characteristics observed. Namely they are, to include nearest track information (such as momentum and particle ID) to the current MVA used to discriminate HSO and LPT clustering, and to include cluster-track directional information to better discriminate these spurious photons. A number of specific ways to improve these studies were presented to account for the drawbacks of `ParticleGun` simulations and the scenarios left out of the data set used in this thesis. These recommendations are likely to improve signal purity in physics analyses, thereby improving the precision of measurements at Belle II which are and will be world leading in the coming years.

Bibliography

[1] Ziro Maki, Masami Nakagawa, and Shoichi Sakata. "Remarks on the Unified Model of Elementary Particles". In: *Progress of Theoretical Physics* 28.5 (Nov. 1962), pp. 870–880. URL: https://doi.org/10.1143/PTP.28.870.

[2] Y. Fukuda et al. "Evidence for Oscillation of Atmospheric Neutrinos". In: *Phys. Rev. Lett.* 81 (8 Aug. 1998), pp. 1562–1567. URL: https://link.aps.org/doi/10.1103/PhysRevLett.81.1562.

[3] Q. R. Ahmad et al. "Measurement of the Rate of $\nu_e + d \rightarrow p + p + e^-$ Interactions Produced by ^8B Solar Neutrinos at the Sudbury Neutrino Observatory". In: *Phys. Rev. Lett.* 87 (7 July 2001), p. 071301. URL: https://link.aps.org/doi/10.1103/PhysRevLett.87.071301.

[4] D. London and J. Matias. "B Flavor Anomalies: 2021 Theoretical Status Report". In: *Annual Review of Nuclear and Particle Science* 72.1 (Sept. 2022), pp. 37–68. URL: https://doi.org/10.1146%2Fannurev-nucl-102020-090209.

[5] T. Abe et al. *Belle II Technical Design Report*. Tech. rep. 2010. URL: https://arxiv.org/abs/1011.0352.

[6] Kazunori Akai, Kazuro Furukawa, and Haruyo Koiso. "SuperKEKB collider". In: *Nuclear Instruments and Methods in Physics Research Section A: Accelerators, Spectrometers, Detectors and Associated Equipment* 907 (Nov. 2018), pp. 188–199. URL: https://doi.org/10.1016%2Fj.nima.2018.08.017.

[7] Particle Data Group. “Review of Particle Physics”. In: *Progress of Theoretical and Experimental Physics* 2022.8 (Aug. 2022). 083C01. URL: https://doi.org/10.1093/ptep/ptac097.

[8] F. Abe et al. “Observation of Top Quark Production in $\overline{p}p$ Collisions with the Collider Detector at Fermilab”. In: *Phys. Rev. Lett.* 74 (14 Apr. 1995), pp. 2626–2631. URL: https://link.aps.org/doi/10.1103/PhysRevLett.74.2626.

[9] S. Abachi et al. “Observation of the Top Quark”. In: *Phys. Rev. Lett.* 74 (14 Apr. 1995), pp. 2632–2637. URL: https://link.aps.org/doi/10.1103/PhysRevLett.74.2632.

[10] CMS Collaboration. “Observation of a new boson at a mass of 125 GeV with the CMS experiment at the LHC”. In: *Physics Letters B* 716.1 (2012), pp. 30–61. URL: https://www.sciencedirect.com/science/article/pii/S0370269312008581.

[11] ATLAS Collaboration. “Observation of a new particle in the search for the Standard Model Higgs boson with the ATLAS detector at the LHC”. In: *Physics Letters B* 716.1 (2012), pp. 1–29. URL: https://www.sciencedirect.com/science/article/pii/S037026931200857X.

[12] M. Awramik et al. “Precise prediction for the W-boson mass in the standard model”. In: *Phys. Rev. D* 69 (5 Mar. 2004), p. 053006. URL: https://link.aps.org/doi/10.1103/PhysRevD.69.053006.

[13] T. et al. Aaltonen. “High-precision measurement of the W-boson mass with the CDF II detector”. In: *Science* 376.6589 (2022), pp. 170–176.

[14] Paul A. M. Dirac. “The quantum theory of the electron”. In: *Proc. Roy. Soc. Lond. A* 117 (1928), pp. 610–624.

[15] Sheldon L. Glashow. “Partial-symmetries of weak interactions”. In: *Nuclear Physics* 22.4 (1961), pp. 579–588. URL: https://www.sciencedirect.com/science/article/pii/0029558261904692.

[16] Steven Weinberg. “A Model of Leptons”. In: *Phys. Rev. Lett.* 19 (21 Nov. 1967), pp. 1264–1266. URL: https://link.aps.org/doi/10.1103/PhysRevLett.19.1264.

[17] Abdus Salam. “Weak and Electromagnetic Interactions”. In: *Conf. Proc. C* 680519 (Oct. 1968), pp. 367–377. URL: https://www.worldscientific.com/doi/abs/10.1142/9789812795915_0034.

[18] S. L. Glashow, J. Iliopoulos, and L. Maiani. “Weak Interactions with Lepton-Hadron Symmetry”. In: *Phys. Rev. D* 2 (7 Oct. 1970), pp. 1285–1292. URL: https://link.aps.org/doi/10.1103/PhysRevD.2.1285.

[19] H. Fritzsch, M. Gell-Mann, and H. Leutwyler. “Advantages of the color octet gluon picture”. In: *Physics Letters B* 47.4 (1973), pp. 365–368. URL: https://www.sciencedirect.com/science/article/pii/0370269373906254.

[20] C. N. Yang and R. L. Mills. “Conservation of Isotopic Spin and Isotopic Gauge Invariance”. In: *Phys. Rev.* 96 (1 Oct. 1954), pp. 191–195. URL: https://link.aps.org/doi/10.1103/PhysRev.96.191.

[21] F. Englert and R. Brout. “Broken Symmetry and the Mass of Gauge Vector Mesons”. In: *Phys. Rev. Lett.* 13 (9 Aug. 1964), pp. 321–323. URL: https://link.aps.org/doi/10.1103/PhysRevLett.13.321.

[22] Peter W. Higgs. “Broken Symmetries and the Masses of Gauge Bosons”. In: *Phys. Rev. Lett.* 13 (16 Oct. 1964), pp. 508–509. URL: https://link.aps.org/doi/10.1103/PhysRevLett.13.508.

[23] *Go on a particle quest at the first CERN webfest*. CERN Bulletin Archive, issues 35/2012 and 36/2012. Aug. 2012. URL: https://cds.cern.ch/record/1473657 (visited on 08/22/2023).

[24] H. David Politzer. “Reliable Perturbative Results for Strong Interactions?” In: *Phys. Rev. Lett.* 30 (26 June 1973), pp. 1346–1349. URL: https://link.aps.org/doi/10.1103/PhysRevLett.30.1346.

[25] David J. Gross and Frank Wilczek. “Ultraviolet Behavior of Non-Abelian Gauge Theories”. In: *Phys. Rev. Lett.* 30 (26 June 1973), pp. 1343–1346. URL: https://link.aps.org/doi/10.1103/PhysRevLett.30.1343.

[26] C. S. Wu et al. “Experimental Test of Parity Conservation in Beta Decay”. In: *Phys. Rev.* 105 (4 Feb. 1957), pp. 1413–1415. URL: https://link.aps.org/doi/10.1103/PhysRev.105.1413.

[27] R Acquafredda et al. “The OPERA experiment in the CERN to Gran Sasso neutrino beam”. In: *Journal of Instrumentation* 4.04 (Apr. 2009), P04018. URL: https://dx.doi.org/10.1088/1748-0221/4/04/P04018.

[28] Particle Data Group. “Review of Particle Physics, Passage of Particles Through Matter”. In: *Progress of Theoretical and Experimental Physics* 2022.8 (Aug. 2022). 083C01, pp. 549–564. URL: https://doi.org/10.1093/ptep/ptac097.

[29] A. Abashian et al. “The Belle detector”. In: *Nuclear Instruments and Methods in Physics Research Section A: Accelerators, Spectrometers, Detectors and Associated Equipment* 479.1 (2002). Detectors for Asymmetric B-factories, pp. 117–232. URL: https://www.sciencedirect.com/science/article/pii/S0168900201020137.

[30] E Kou et al. “The Belle II Physics Book”. In: *Progress of Theoretical and Experimental Physics* 2019.12 (Dec. 2019). URL: https://doi.org/10.1093%2Fptep%2Fptz106.

[31] Demin Zhou et al. *Luminosity performance of SuperKEKB*. 2023.

[32] Valerio Bertacchi et al. “Track finding at Belle II”. In: *Computer Physics Communications* 259 (Feb. 2021), p. 107610. URL: https://doi.org/10.1016%2Fj.cpc.2020.107610.

[33] S. Longo and J. M. Roney. “Hadronic vs Electromagnetic Pulse Shape Discrimination in CsI(Tl) for High Energy Physics Experiments”. In: *JINST* 13.03 (2018), P03018.

[34] T. Kuhr et al. "The Belle II Core Software". In: *Comput. Softw. Big Sci.* 3.1 (2019), p. 1. URL: https://link.springer.com/article/10.1007/s41781-018-0017-9.

[35] The Belle II Collaboration. *Belle 2 Software Documentation*. July 2022. URL: https://software.belle2.org/release-06-00-14/sphinx/index.html (visited on 07/31/2023).

[36] S. Agostinelli et al. "Geant4—a simulation toolkit". In: *Nuclear Instruments and Methods in Physics Research Section A: Accelerators, Spectrometers, Detectors and Associated Equipment* 506.3 (2003), pp. 250–303. URL: https://www.sciencedirect.com/science/article/pii/S0168900203013688.

[37] D. J. Lange. "The EvtGen particle decay simulation package". In: *Nuclear Instruments and Methods in Physics Research Section A: Accelerators, Spectrometers, Detectors and Associated Equipment* 462.1 (2001). BEAUTY2000, Proceedings of the 7th Int. Conf. on B-Physics at Hadron Machines, pp. 152–155. URL: https://www.sciencedirect.com/science/article/pii/S0168900201000894.

[38] Geant4 Collaboration. *Physics Reference Manual*. July 2023. URL: https://geant4-userdoc.web.cern.ch/UsersGuides/PhysicsReferenceManual/fo/PhysicsReferenceManual.pdf (visited on 08/30/2023).

[39] M. De Nuccio and T. Ferber. *Tutorial: The Belle II Electromagnetic Calorimeter*. Jan. 2020. URL: https://indico.belle2.org/event/1307/sessions/378/attachments/3070/5670/mmilesi_ECLPid_B2SKW_2020.pdf (visited on 07/31/2023).

[40] A. Natochii et al. "Beam background expectations for Belle II at SuperKEKB". In: (Aug. 2022). URL: https://arxiv.org/abs/2203.05731.

[41] T. Keck et al. "The Full Event Interpretation: An Exclusive Tagging Algorithm for the Belle II Experiment". In: *Comput. Softw. Big Sci.* 3.1 (Feb. 2019), p. 6. URL: https://link.springer.com/article/10.1007/s41781-019-0021-8.

[42] P. Cheema et al. “Development of FastBDT Classifiers to Suppress Beam Background Clusters and Fake Photons”. In: *Belle II Internal Document* (Apr. 2023). URL: https://docs.belle2.org/record/3528/.

[43] S. Longo et al. “CsI(Tl) pulse shape discrimination with the Belle II electromagnetic calorimeter as a novel method to improve particle identification at electron–positron colliders”. In: *Nuclear Instruments and Methods in Physics Research Section A: Accelerators, Spectrometers, Detectors and Associated Equipment* 982 (2020), p. 164562. URL: https://www.sciencedirect.com/science/article/pii/S0168900220309591.

[44] A. Hershenhorn, T. Ferber, and C. Hearty. “ECL shower shape variables based on Zernike moments”. In: *Belle II Internal Document* (Jan. 2017). URL: https://docs.belle2.org/record/454?ln=en.

[45] Thomas Keck. *FastBDT: A speed-optimized and cache-friendly implementation of stochastic gradient-boosted decision trees for multivariate classification*. Sept. 2016. URL: https://arxiv.org/abs/1609.06119.

[46] F. Zernike. “Beugungstheorie des schneidenver-fahrens und seiner verbesserten form, der phasenkontrastmethode”. In: *Physica* 1.7 (1934), pp. 689–704. URL: https://www.sciencedirect.com/science/article/pii/S0031891434802595.

[47] Jake Lever, Martin Krzywinski, and Naomi Altman. “Principal component analysis”. In: *Nature Methods* 14 (2017), pp. 641–642. URL: https://www.nature.com/articles/nmeth.4346.

[48] Ian J. Goodfellow et al. *Generative Adversarial Networks*. 2014.

Appendix A

Figures Related to Probability of Hadronic Interaction

The first figure of this appendix shows the cross sections for negative pions and kaons with protons at momenta relevant to Belle-II. The second figure shows the cluster multiplicity for simulated single positive pion events. The last figure shows how many single particle events were omitted (due to particle decaying or interacting before reaching the ECL) for various particle types at various momenta. These figures are referenced in section 2.2, 5.1, and 5.3.

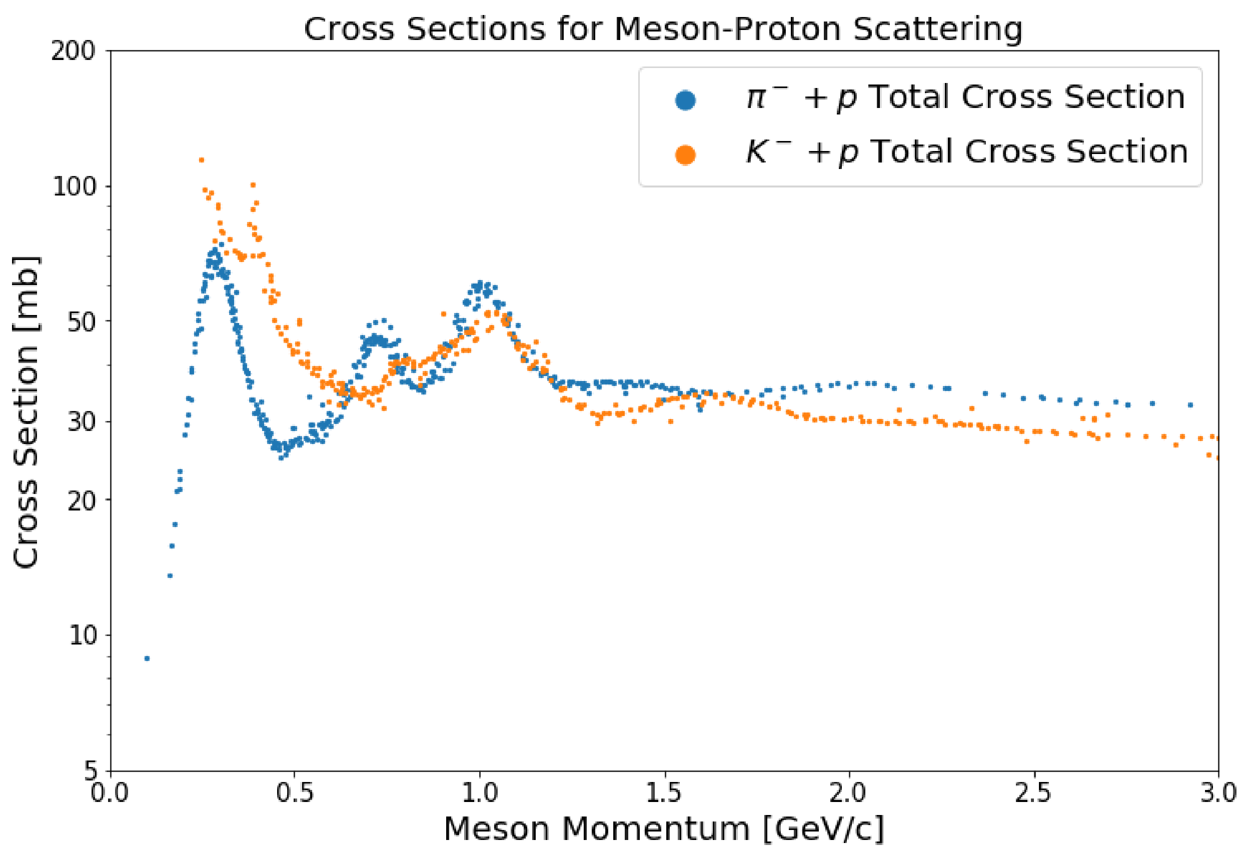

Figure A.1: Cross sections for proton-meson scattering. Error bars are small in this momentum regime, so they have been omitted. Data taken from [7].

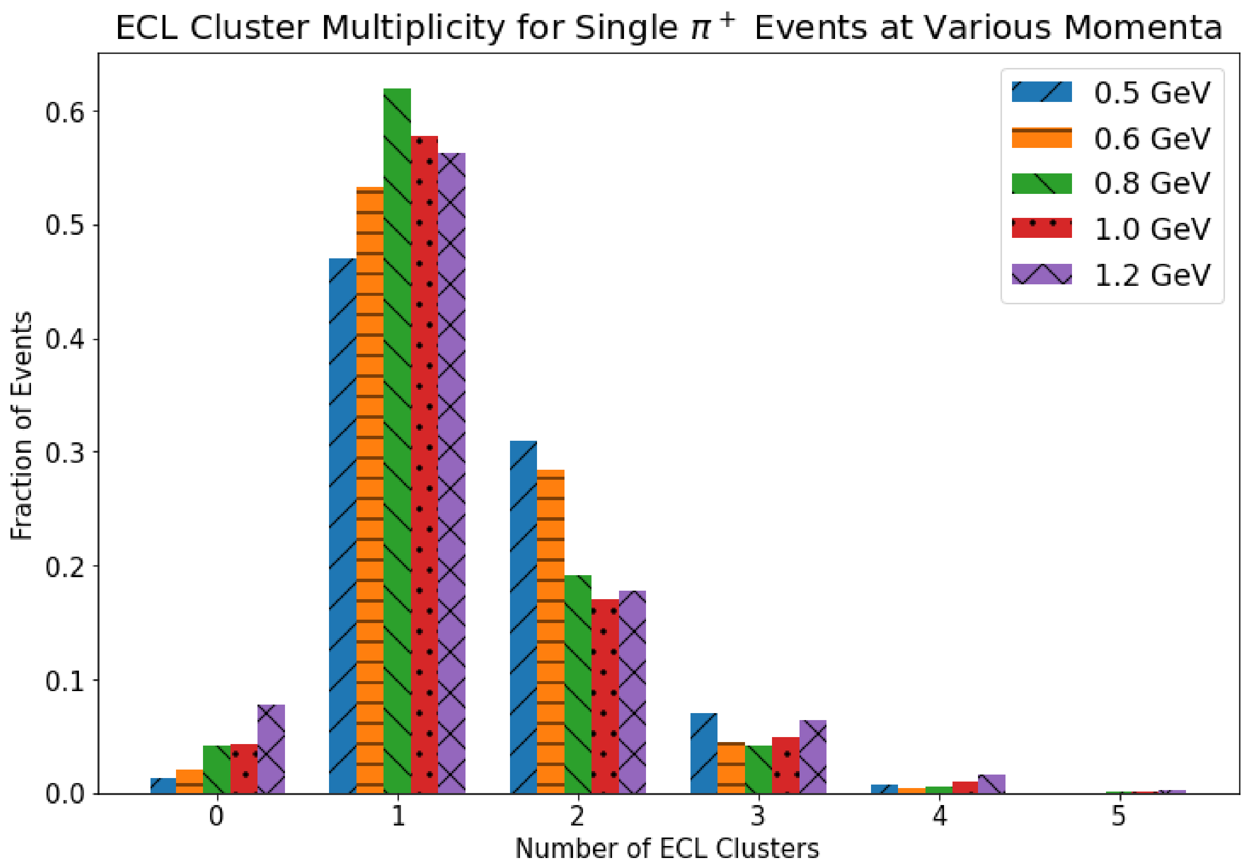

Figure A.2: ECL multiplicity for simulated single positive pion events at various momenta. The momentum for each distribution can be found in the legend.

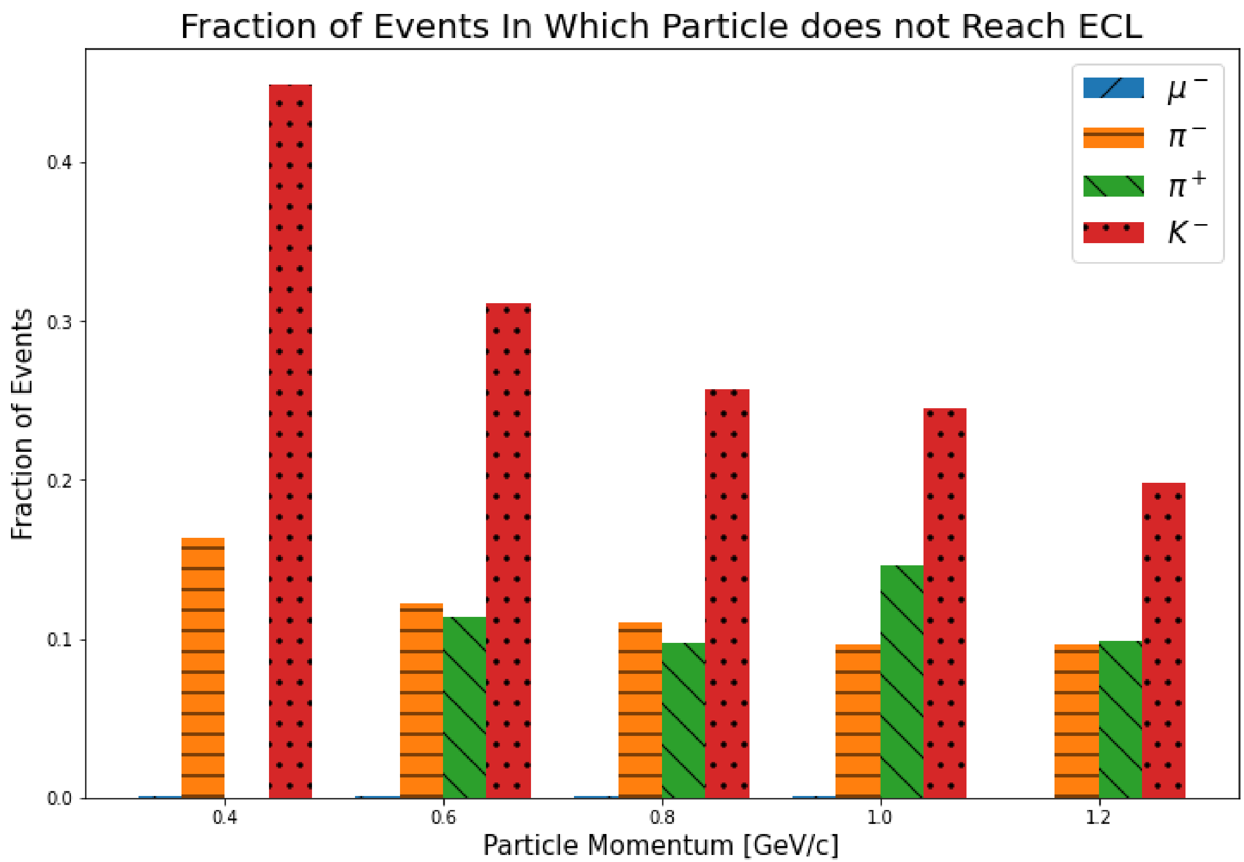

Figure A.3: Fraction of events for each particle and momentum where the initial particle interacts or decays before the ECL. There are no data for 1.2 GeV/c μ^- nor 0.4 GeV/c π^+ since these were not simulated. Kaons decay significantly more than others, especially at low momenta.

Appendix B

Single Particle Event Displays

The first five figures of this appendix are the full versions of the event displays featured in section 5.2. The next five figures are event displays that happen to be interesting, but didn't fit well or were not important enough to feature in the analysis sections. There is a reference to figure B.10 in section 5.4.

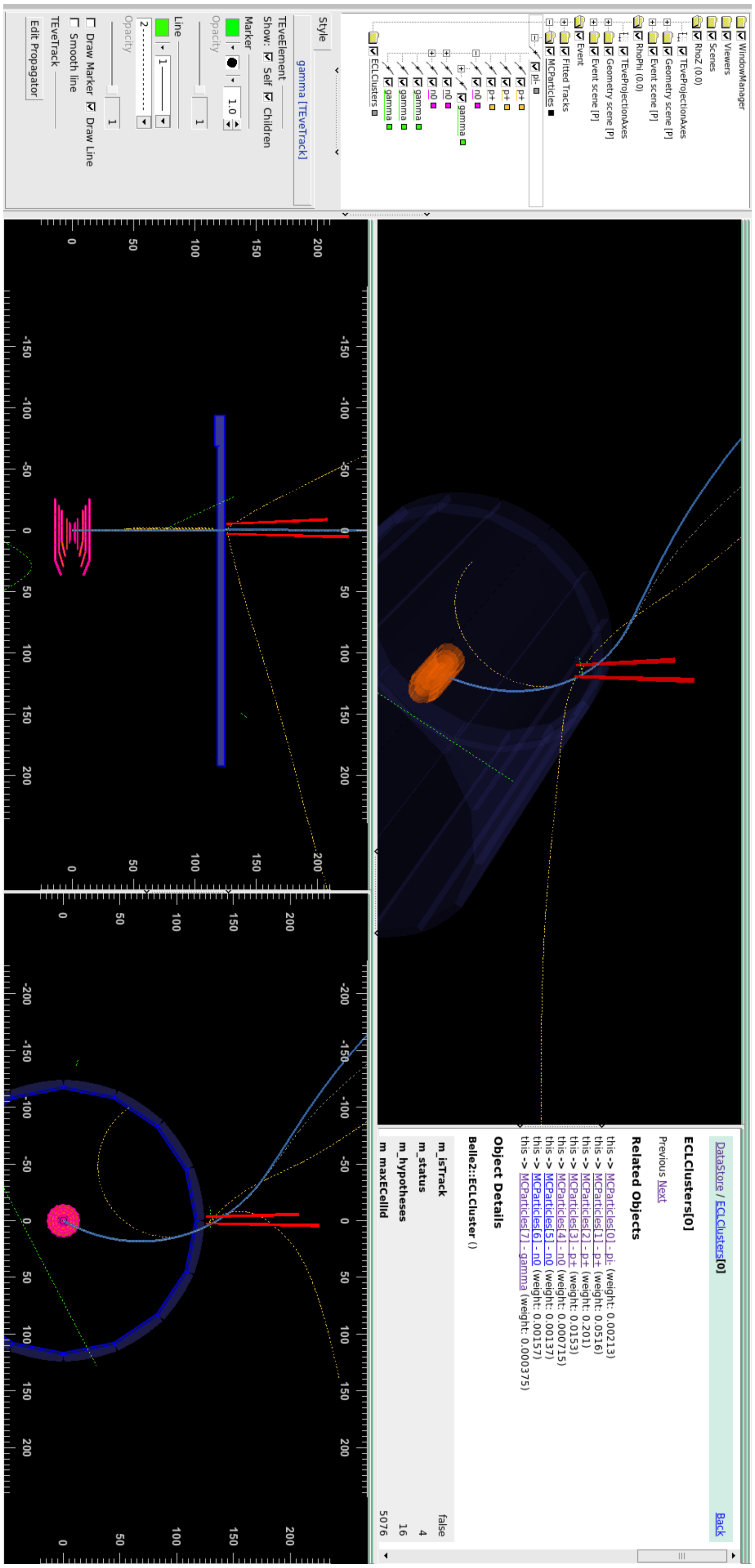

Figure B.1: Full event display for figure 5.1.

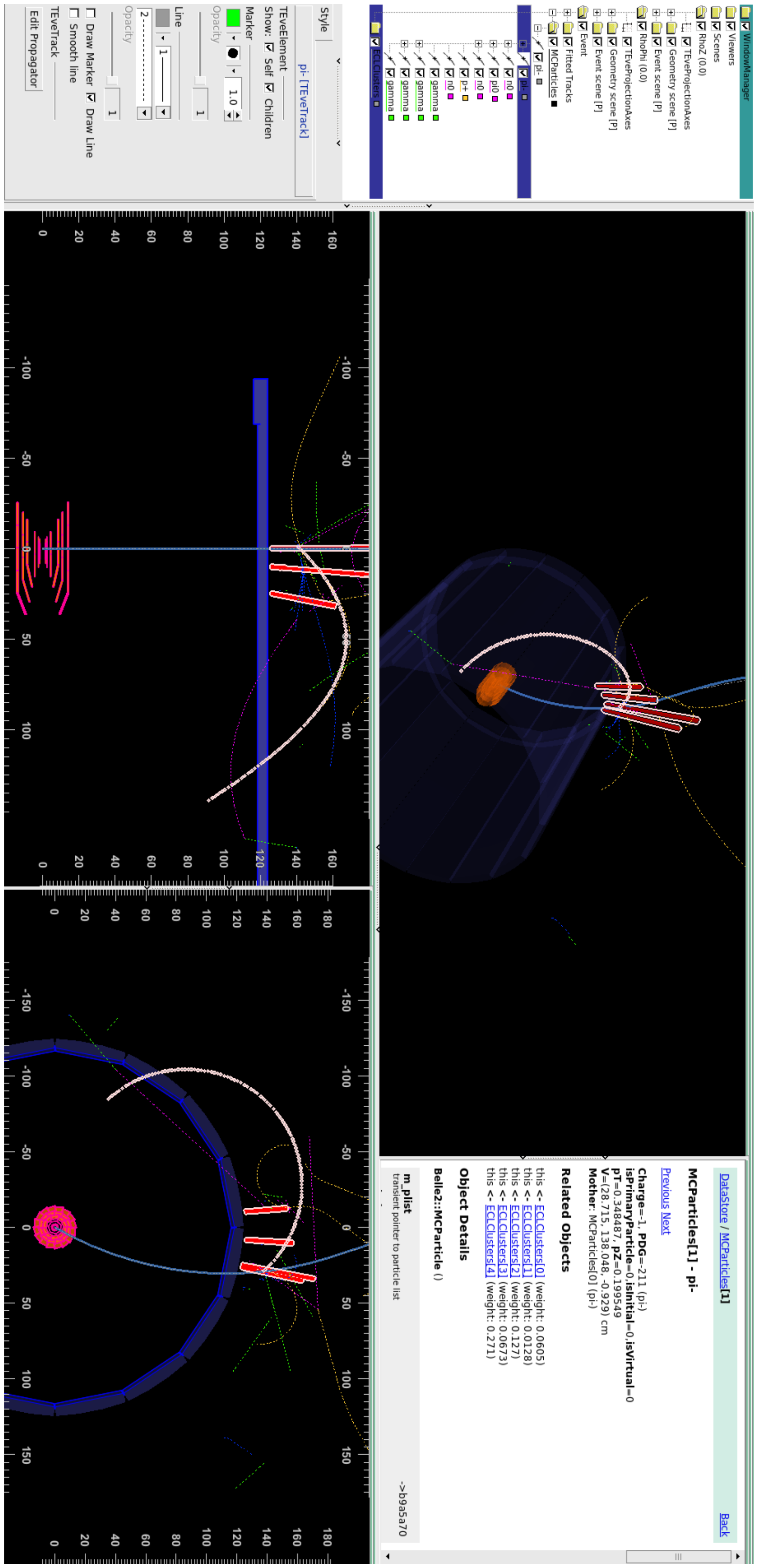

Figure B.2: Full event display for figure 5.2.

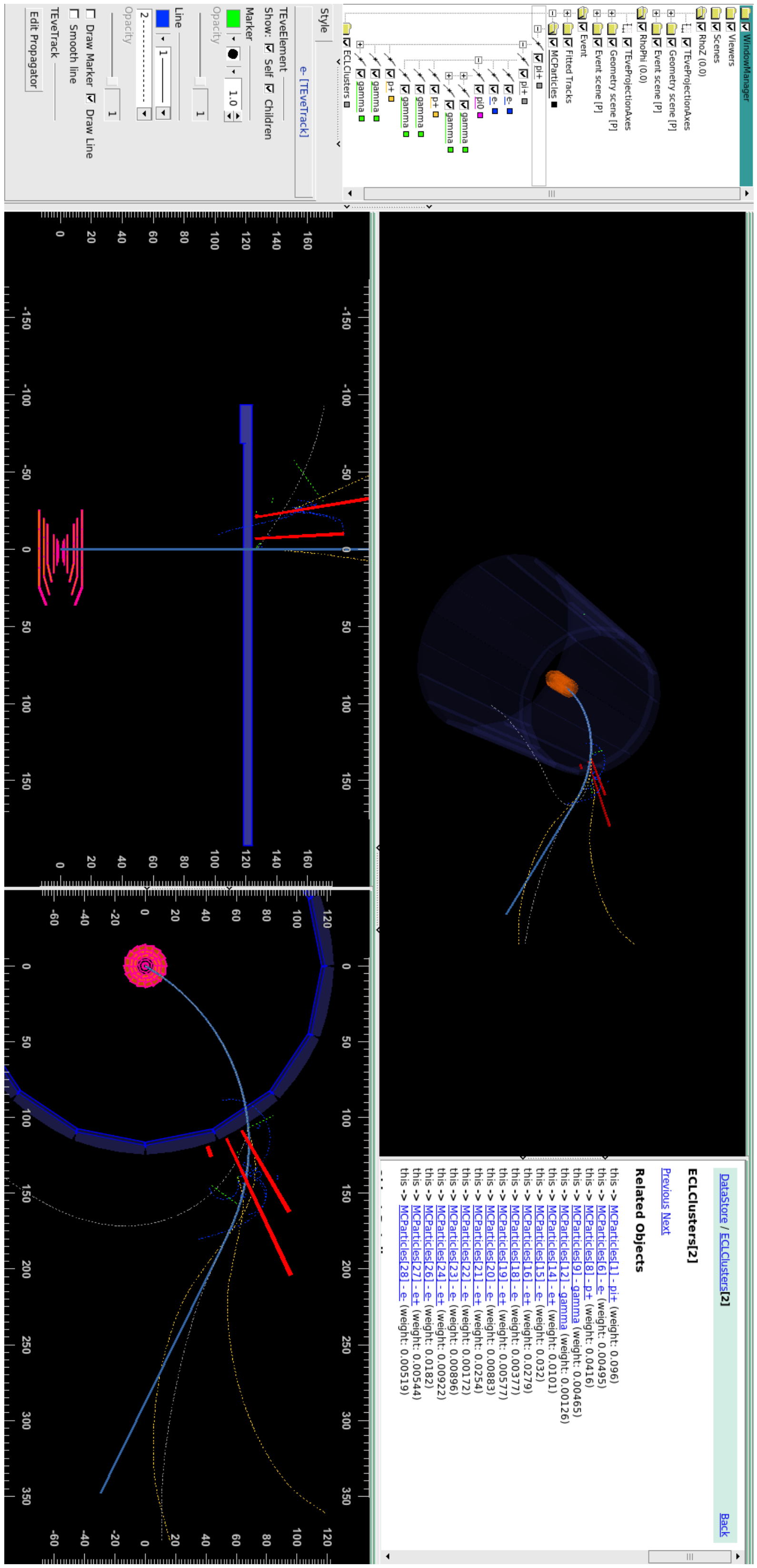

Figure B.3: Full event display for figure 5.3.

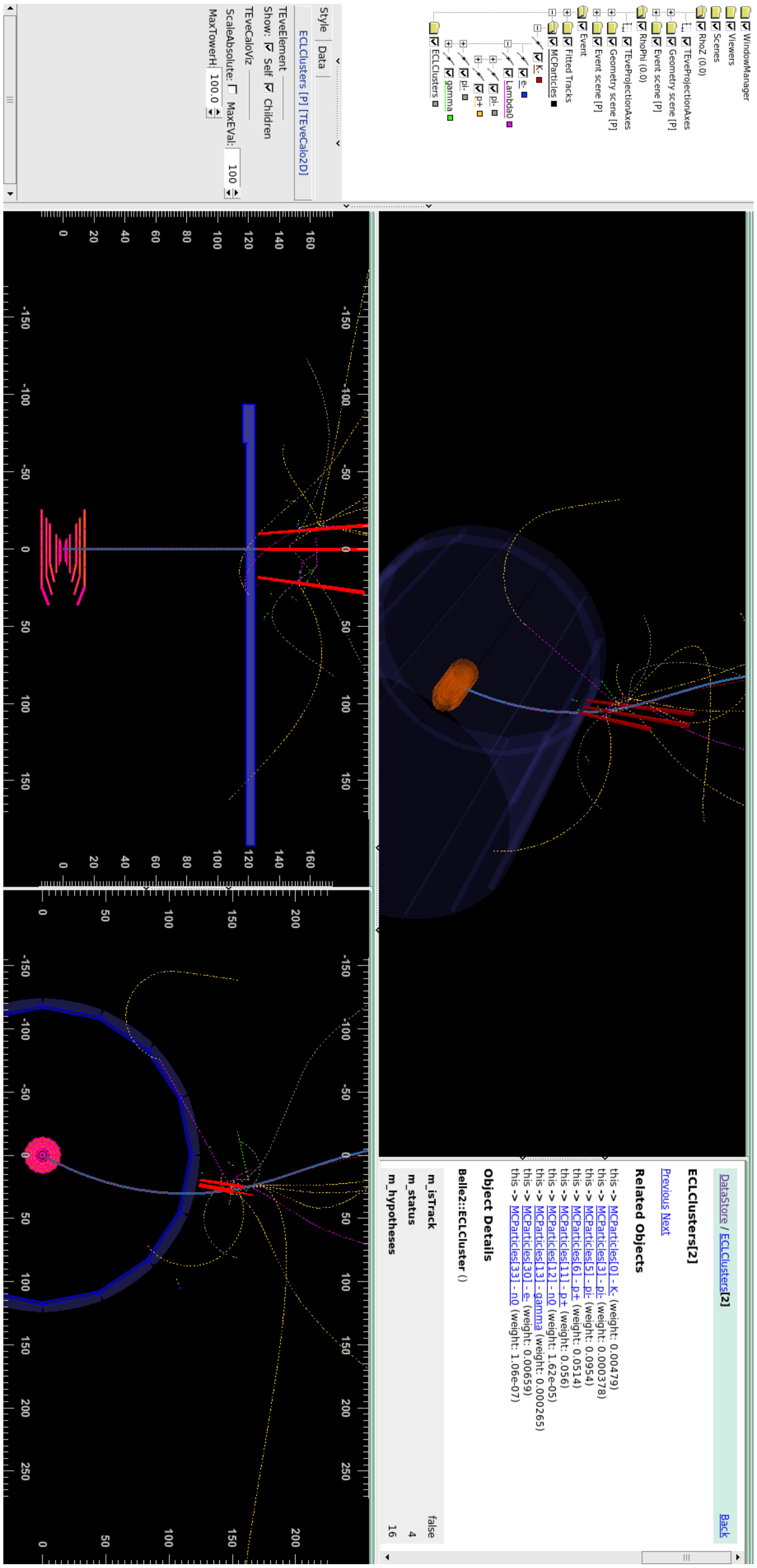

Figure B.4: Full event display for figure 5.4.

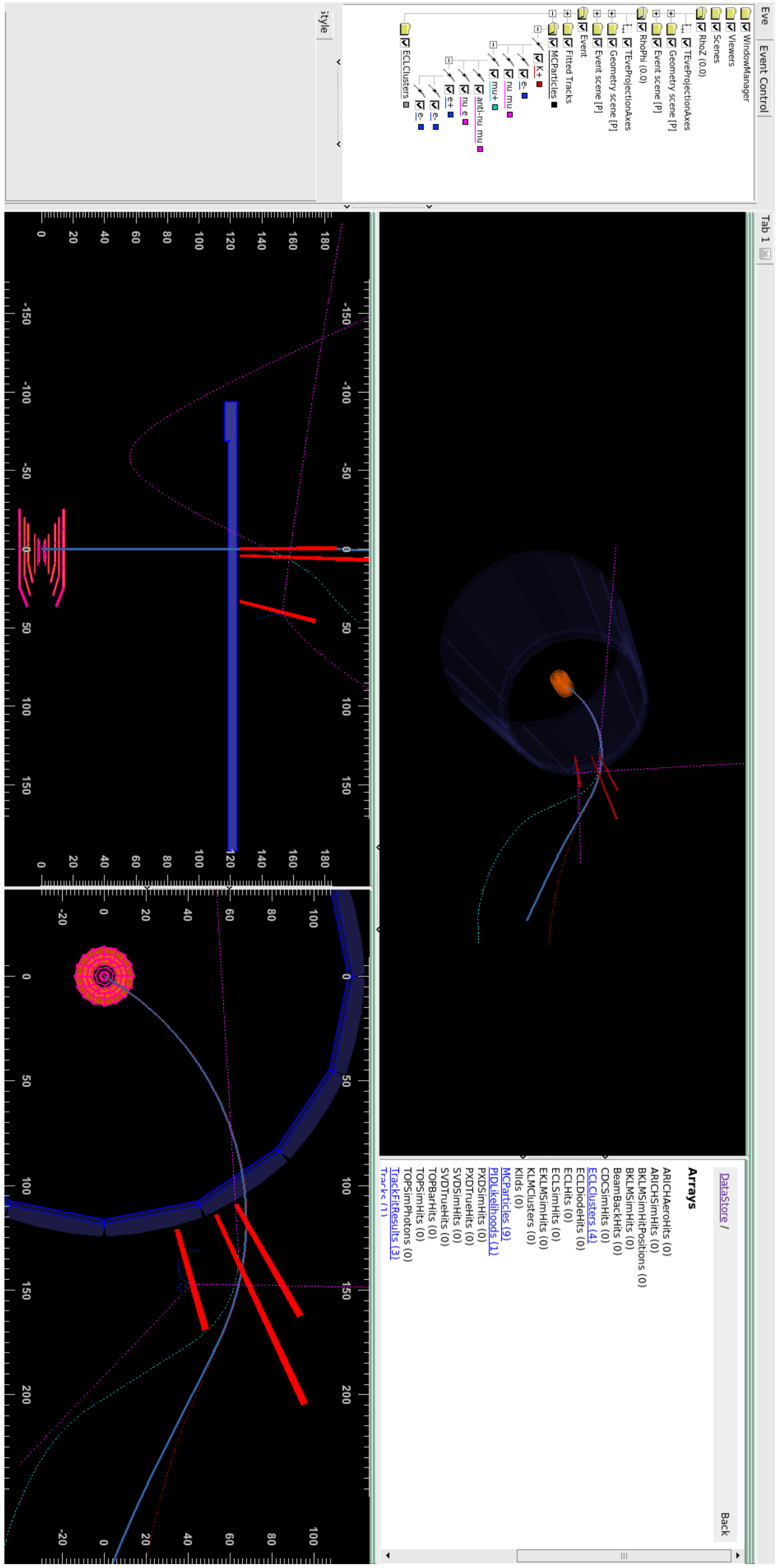

Figure B.5: Full event display for figure 5.5.

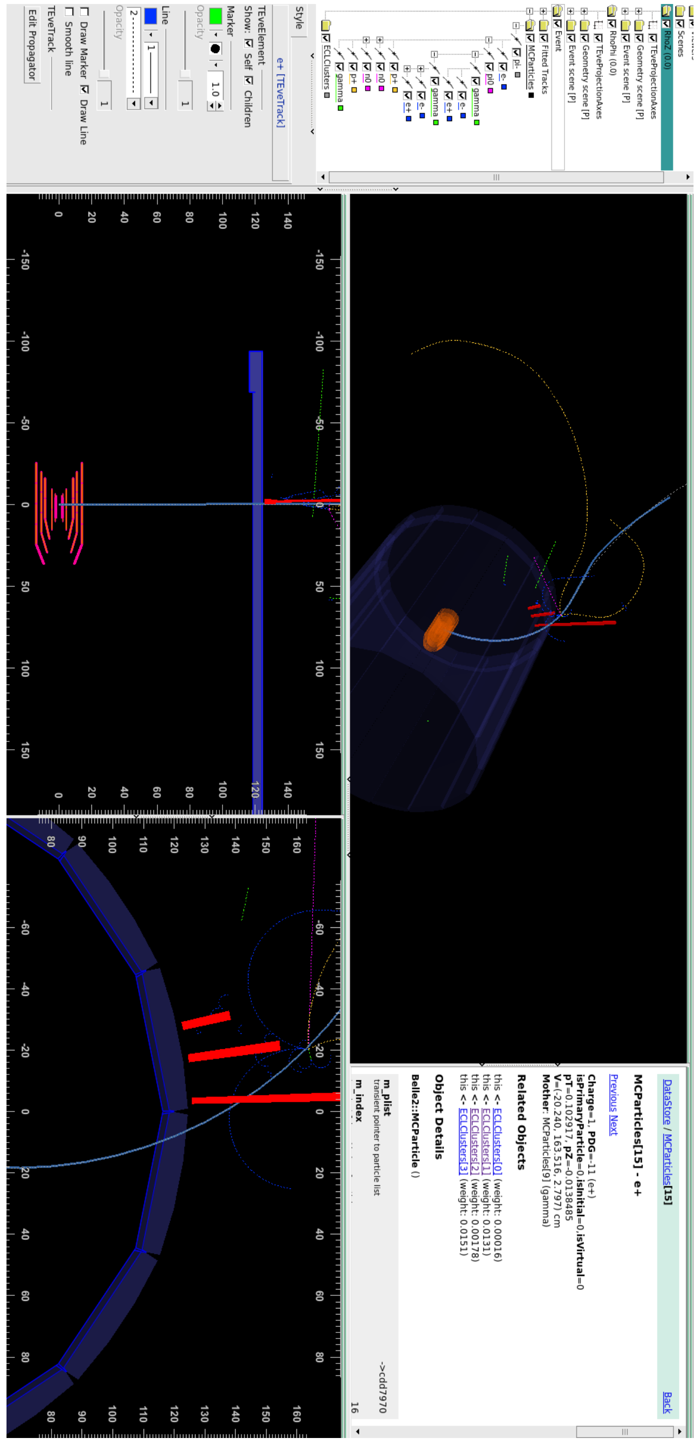

Figure B.6: An instance of hadronic split off from a 0.6 GeV/c momentum π^- interaction leading to a π^0 that decays into photons. This was seen in section 5.2 for a π^+, but is shown here for a pi^- as proof this occurs for either charged pion.

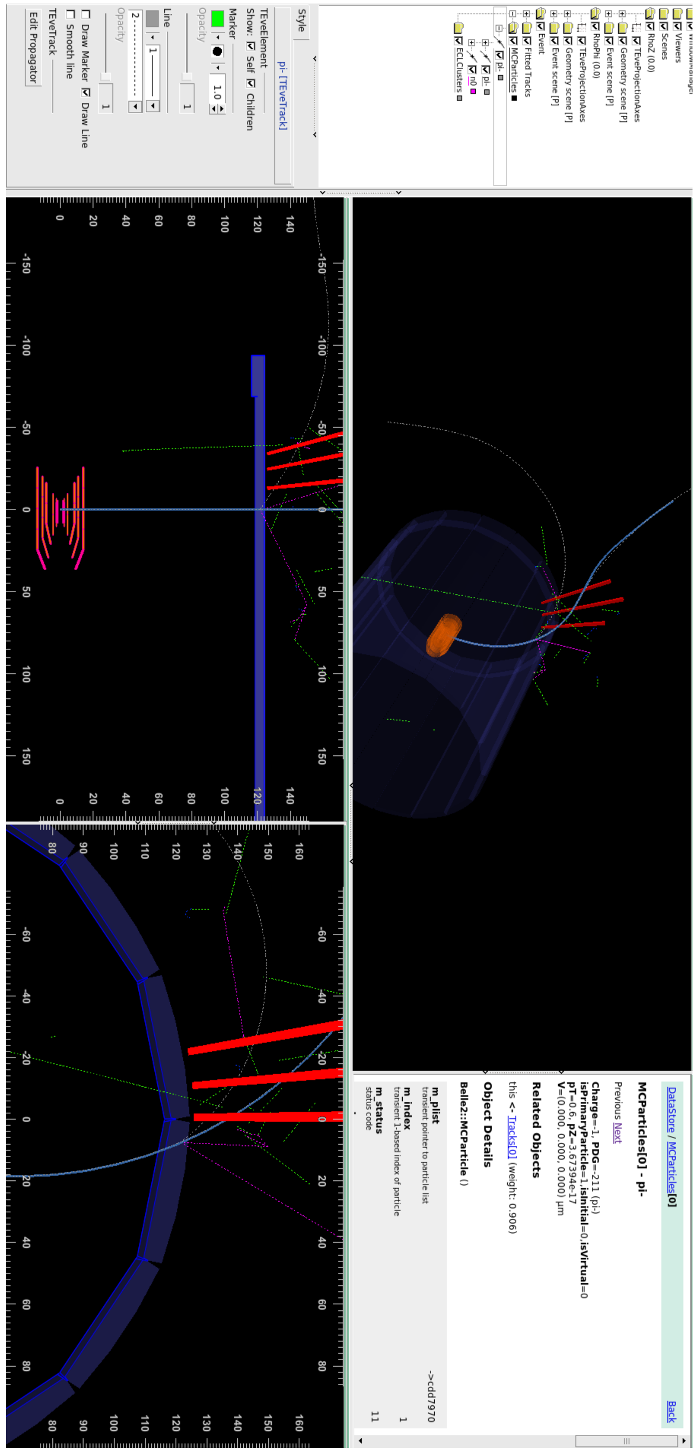

Figure B.7: A 0.6 GeV/c momentum π^- undergoing a nuclear interaction within a TOP crystal, leading to fake photons. This process would be omitted from the single particle event data set since the TOP is before the ECL. It is important to keep in mind the interactions that occur before the ECL, since these produce many spurious photons but are not studied in this thesis.

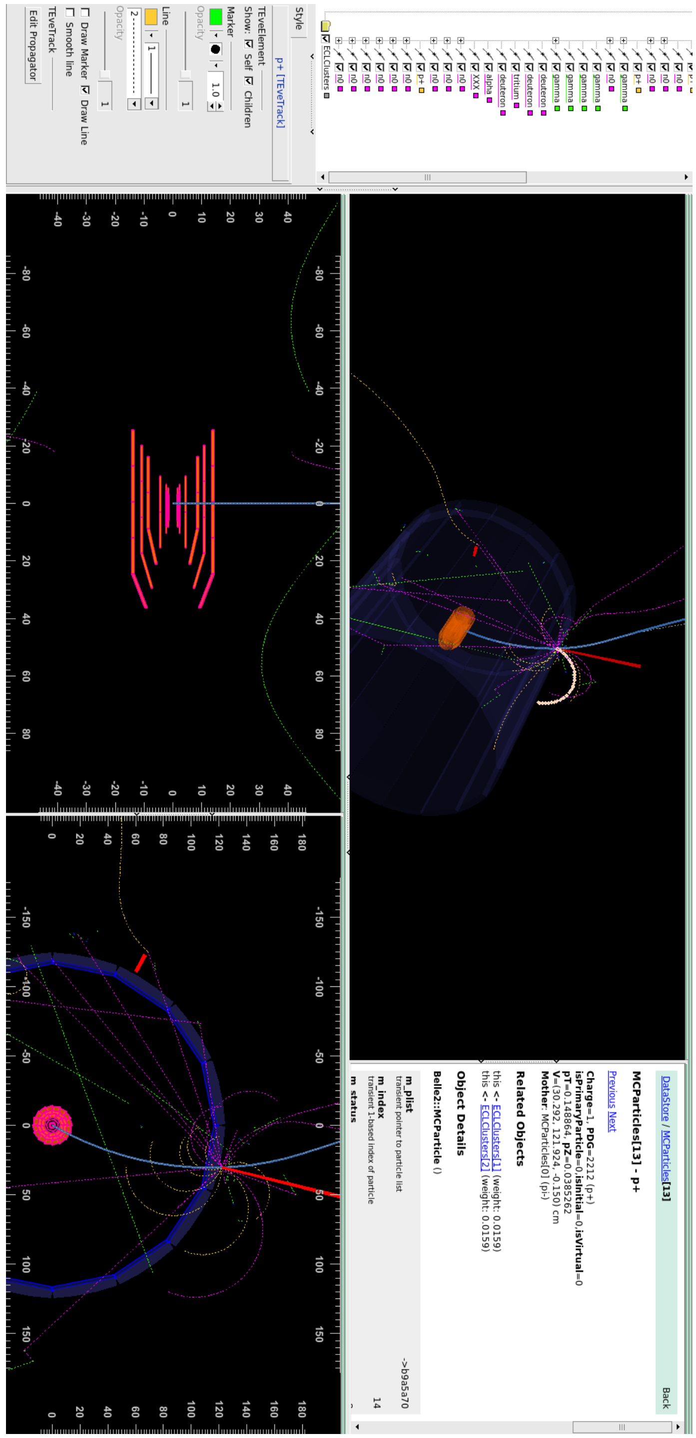

Figure B.8: A 1.0 GeV/c momentum π^- causing a large nuclear interaction including alphas, deuterons, and the a nucleus. This sort of interaction would be impossible if the pion had lower momenta, highlighting the importance of the charged particle's momentum on hadronic split off.

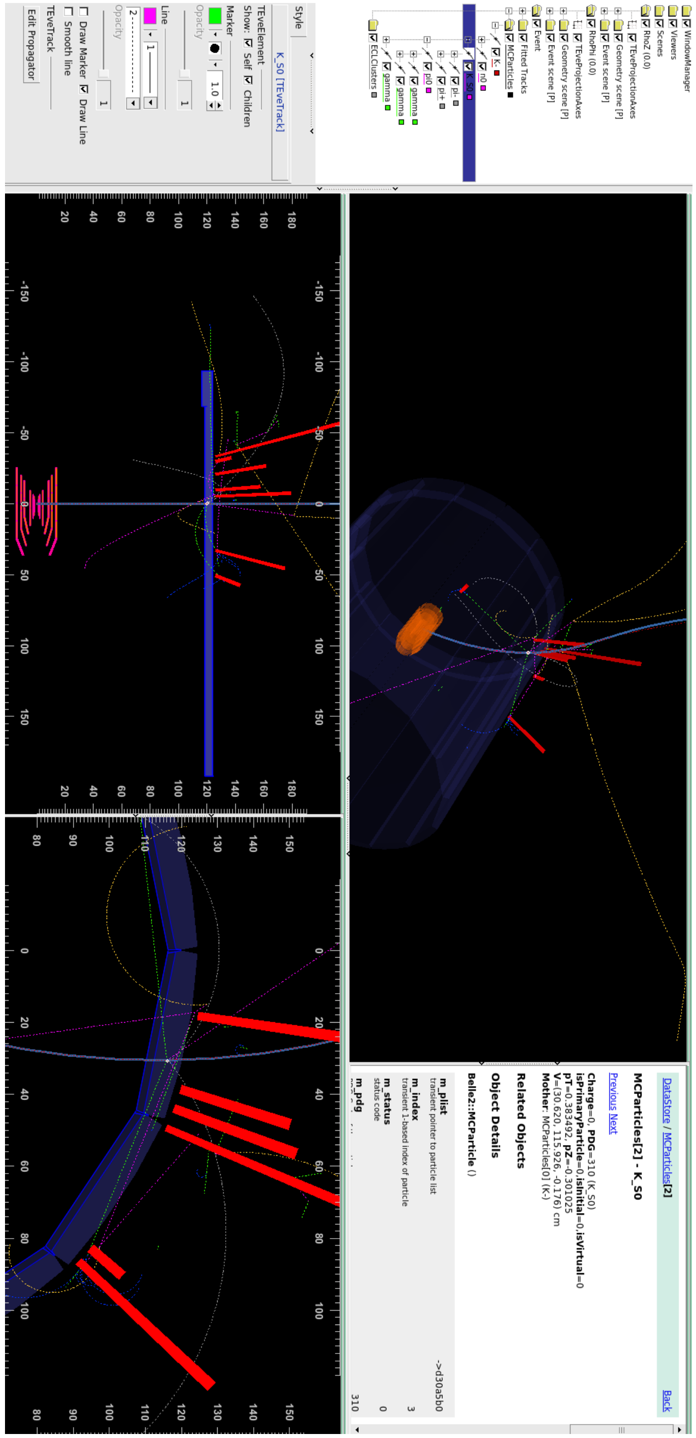

Figure B.9: A 1.0 GeV/c momentum K^- interacting in the TOP. A K_S^0 and π^0 lead to many ECL clusters. This event is omitted from the single particle event data set. This interaction highlights once again the power of the strange quark in the K^-, large momenta, and interaction before the ECL because of the events high ECL multiplicity.

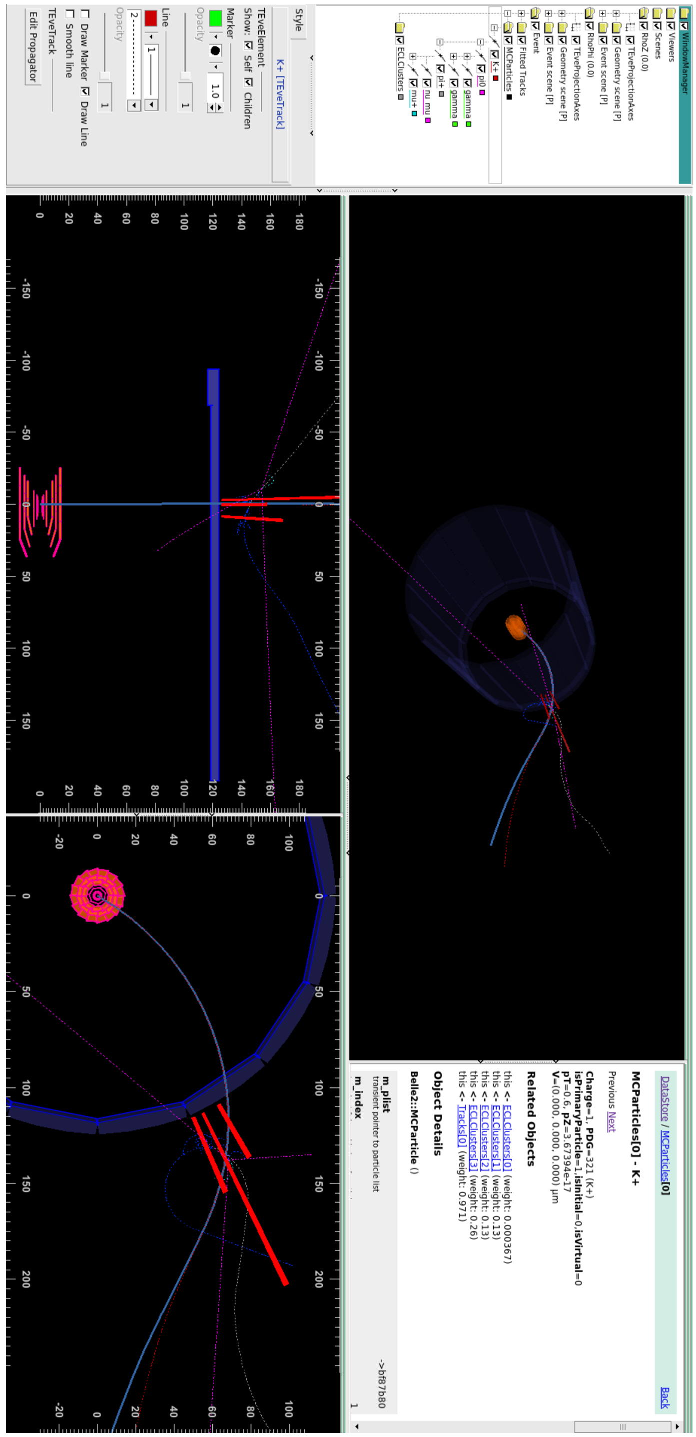

Figure B.10: A 0.6 GeV/c momentum K^+ decaying in the ECL to a π^0 and π^+, causing fake photons. This is an instance where the K^- slows and decays rather than interacts with a nucleus. This doesn't usually occur for pions and highlights another big difference between the two species.

Appendix C

Supplementary ECL Variable Plots

Below are figures that don't show much new or interesting information, but are left here as proof that the statements which reference them in section 5.4 are true.

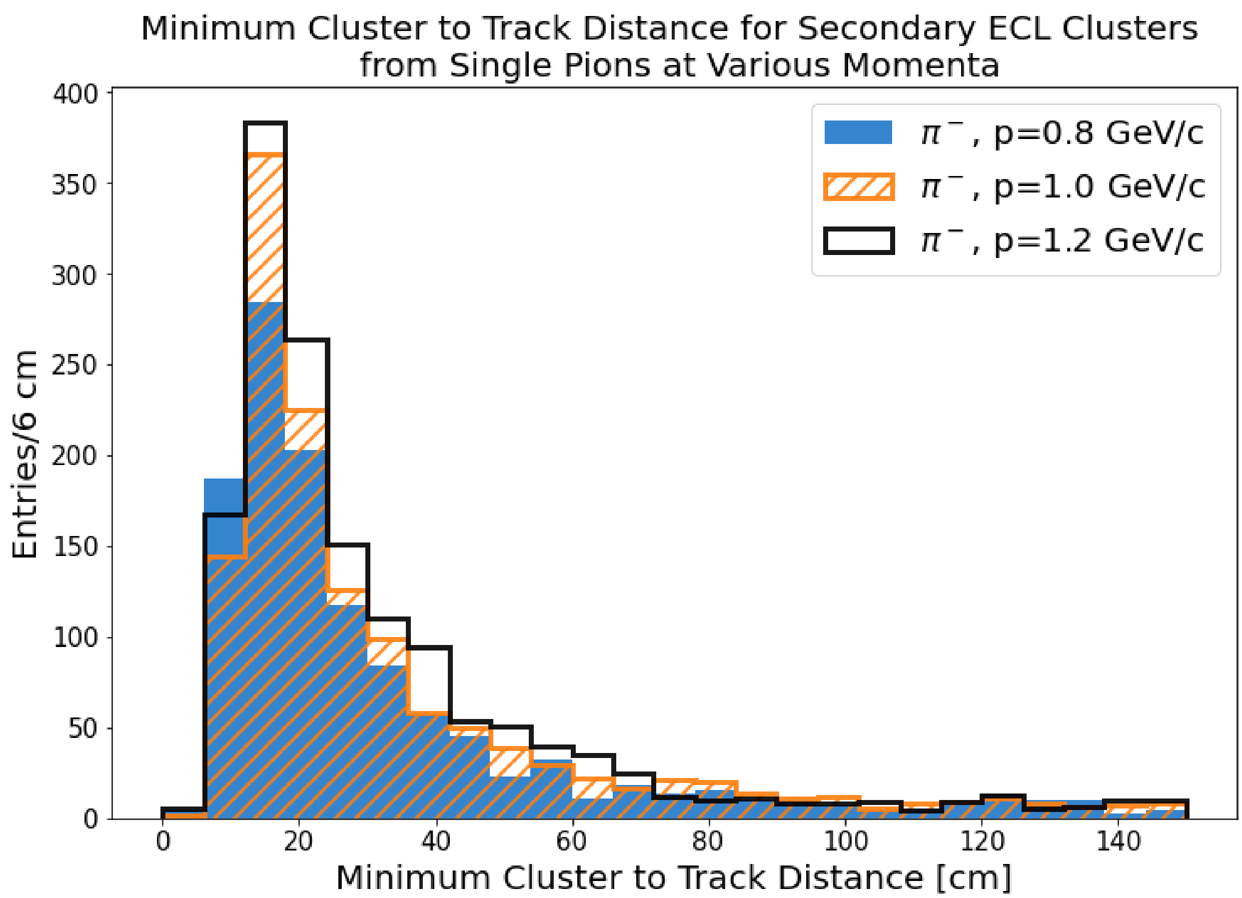

Figure C.1: Distribution of the minimum cluster to track distance of secondary clusters from high momentum pions.

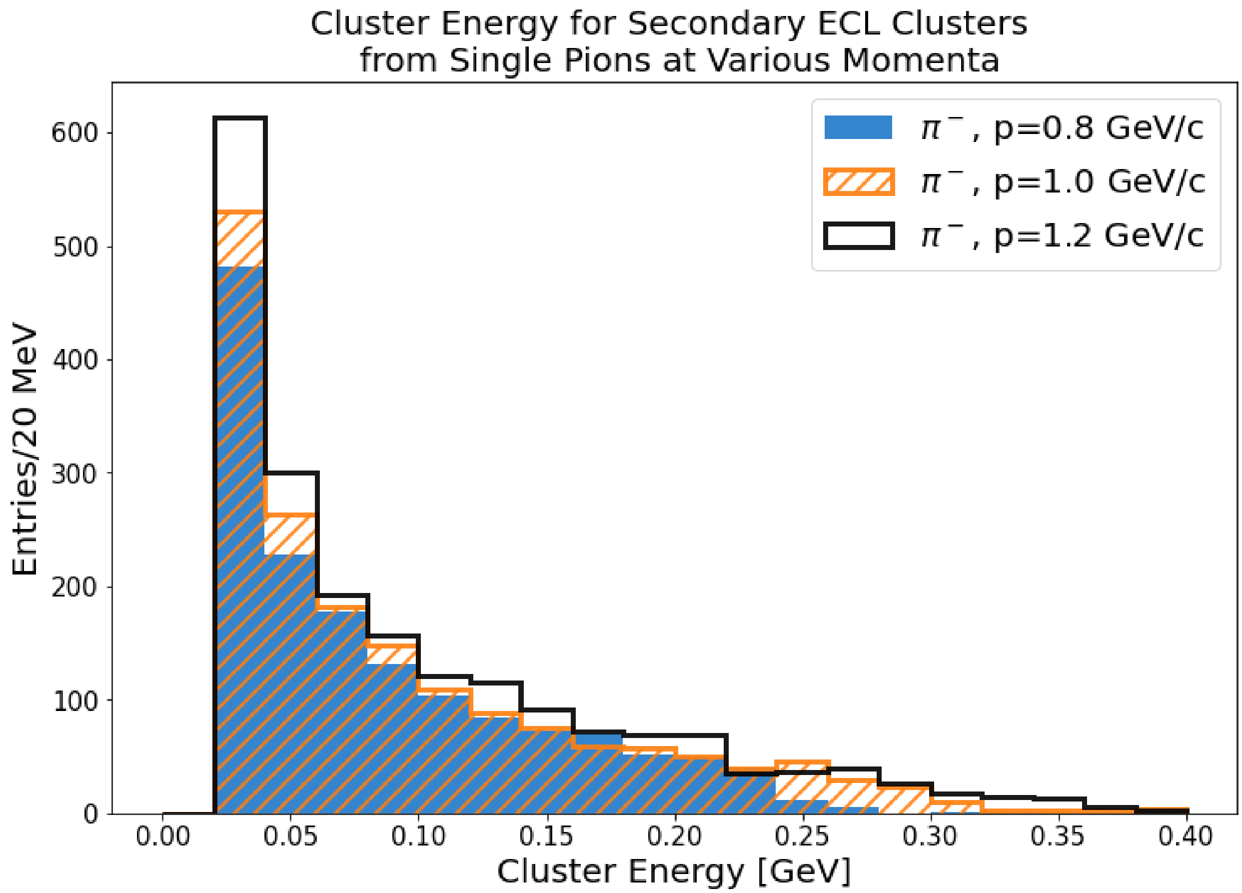

Figure C.2: Distribution of the cluster energy of secondary clusters from high momentum pions.

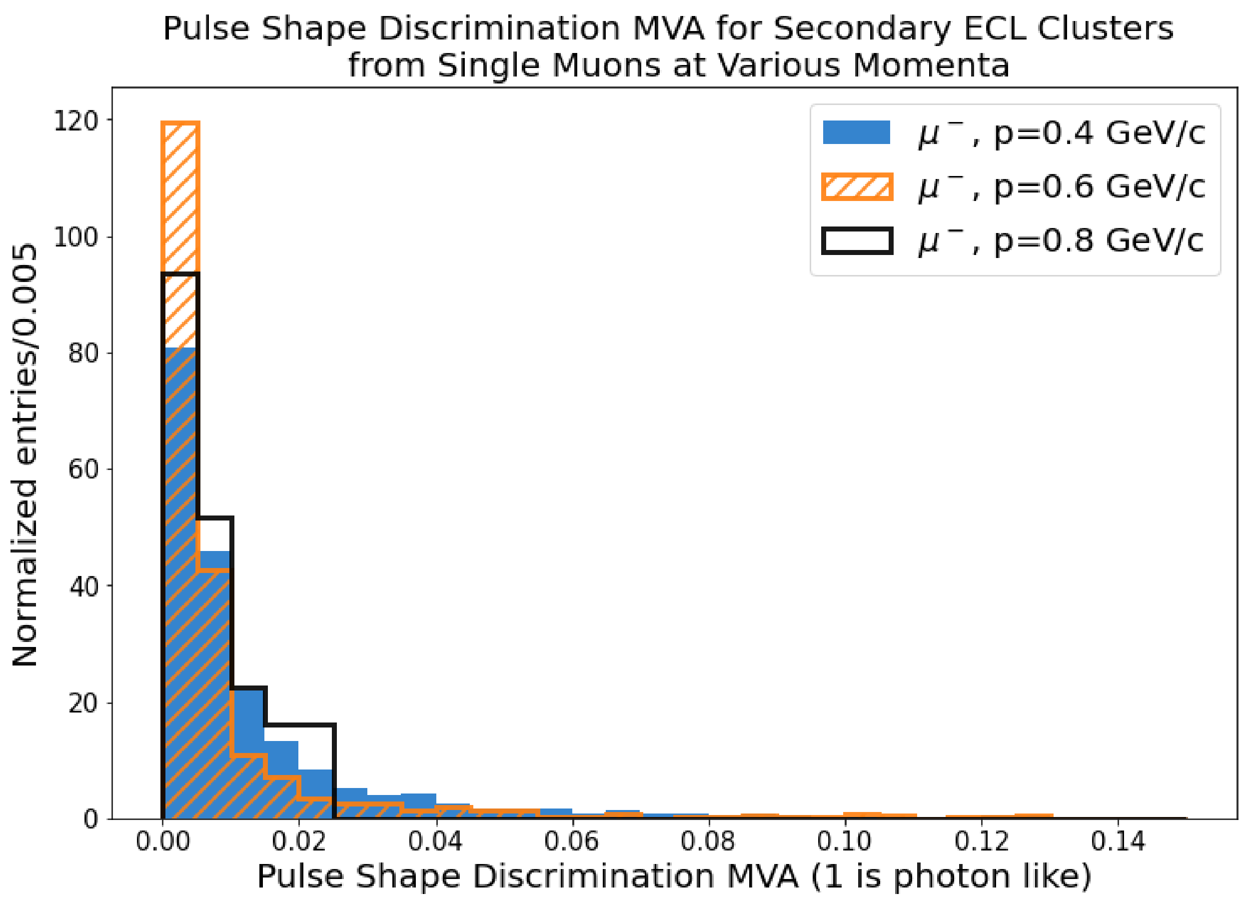

Figure C.3: Normalized distributions of pulse shape discrimination MVA of secondary clusters from muons.

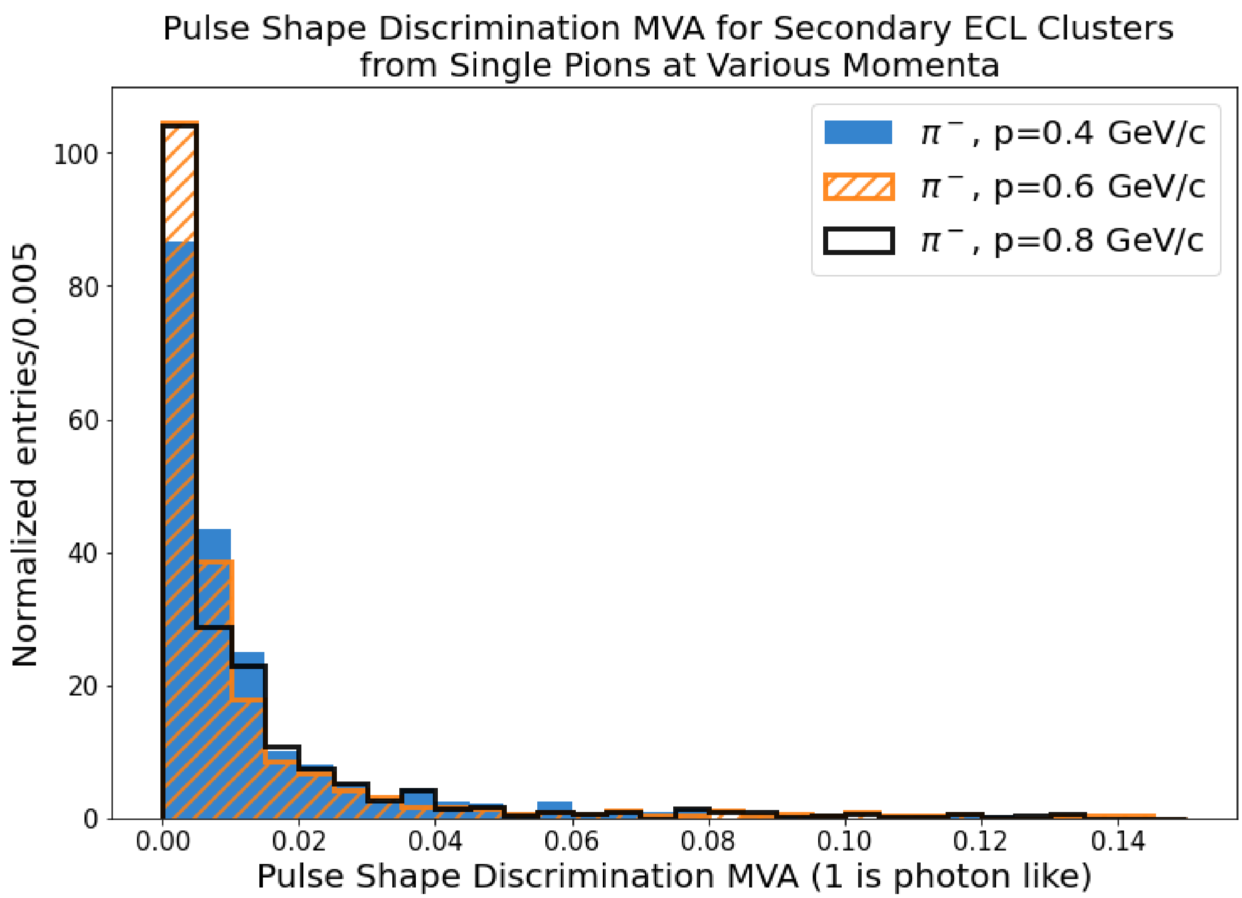

Figure C.4: Normalized distributions of pulse shape discrimination MVA of secondary clusters from pions.